Gas-Phase Infrared Spectroscopy of Metal-Containing Clusters and Complexes



Gabriele Meizyte

Worcester College

University of Oxford

A thesis submitted for the degree of

Doctor of Philosophy

Trinity Term 2022

Abstract

Metal-containing clusters and complexes may represent active sites in heterogeneous catalysts, where catalytic transformations take place, thus offering an elegant approach in studying the fundamental interactions in a simplified way. In this thesis, infrared-(multiple) photodissociation spectroscopy is used to study metal-containing clusters and complexes with atmospherically relevant adsorbates to learn about their reactivity, structural binding motifs, and the degree of activation of adsorbed moieties. Complementary density functional theory calculations help in the assignment of experimentally observed phenomena.

Each chapter describes a different system that presents unique and sometimes unexpected results. N_2O binding to Pt_n^+ proves to be size-dependent; small clusters form molecular N_2O adsorption products whereas larger ones react to produce PtO^+, and similar chemistry is observed upon infrared excitation. Examining N_2O binding to Au_n^+ and Co_n^+ reveals inertness of gold clusters whereas cobalt species prove to be similar in their reactivity to platinum. Size-selective cooperative binding effects are discovered for $Au_nO_2CO^-$ species both from mass spectrometry and spectroscopy. Infrared action spectra of $Co(NO)_n^+$ and $Rh(NO)_n^+$ complexes disclose spectral differences in the number and position of the bands as well as similarities in the NO binding motifs to these metal centres. $Rh(CO)_n(N_2O)_m^+$ system proves to be different than $Au(CO)_n(N_2O)_m^+$ studied by the Mackenzie group previously, and these observations are explained in terms of different electronic structures, relative binding energies, and coordination numbers. Isotopic study of $Au(CO)_n(N_2O)_m^+$ using ^{13}CO reveals a band in the infrared spectrum of the $Au(^{12}CO)_2(N_2O)^+$ complex that is an overlap between individual $^{12}C{\equiv}O$ and N_2O N=N vibrational bands.

Acknowledgements

First of all, I thank my supervisor Prof. Stuart Mackenzie for his continuous support and knowledge sharing throughout the years. Without his motivation and close supervision this DPhil would have been much more difficult, thank you!

Appreciation also goes to the rest of Mackenzie-Timmel group members. Dr Alice Green for teaching me so much about the experiment, Ed Brewer and Philip Pearcy for helping with the experiment when it misbehaved, Dr Peter Watson for your comments on my thesis drafts, Angela Gehrckens, Hang Zhou, Jamie Gravell, Maddy Buffet, Dr Olivier Pare-Labrosse, Patrick Murton for many good evenings, chats, and friendly atmosphere. The Part II students, Sean Kealy, Jack Pickering, Rachael Brown, Olga Duda, and Matthew Doll for chess matches and cheerfulness.

I am also thankful to Dr André Fielicke and collaborators at the Fritz Haber Institute in Berlin for the opportunity to participate in the free electron laser runs and their help.

My MSci project supervisor Dr Hans Senn in the University of Glasgow for introduction to DFT and inspiring me to continue my research journey.

To my parents Jurate & Zilvinas, I am incredibly grateful for providing me with the opportunities that they were not able to have, which has led me to where I am now. I am also forever indebted to my partner Vasilis for his continuous support and pampering. Last but not least, thanks to my tight friends group(s) for keeping me sane and (occasionally) listening to chemistry talk in parties.

List of Publications

Arising directly from this thesis:

G. Meizyte, A. E. Green, A. S. Gentleman, S. Schaller, W. Schöllkopf, A. Fielicke, and S. R. Mackenzie. Free electron laser infrared action spectroscopy of nitrous oxide binding to platinum clusters, $Pt_n(N_2O)^+$. *Phys. Chem. Chem. Phys.*, 22(33):18606−18613, 2020.

E. M. Cunningham, A. E. Green, G. Meizyte, A. S. Gentleman, P. W. Beardsmore, S. Schaller, K. M. Pollow, K. Saroukh, M. Förstel, O. Dopfer, W. Schöllkopf, A. Fielicke, and S. R. Mackenzie. Infrared action spectroscopy of nitrous oxide on cationic gold and cobalt clusters. *Phys. Chem. Chem. Phys.*, 23(1):329−338, 2021.

A. E. Green, R. H. Brown, G. Meizyte, and S. R. Mackenzie. Spectroscopy and infrared photofragmentation dynamics of mixed ligand ion−molecule complexes: $Au(CO)_x(N_2O)_y^+$. *J. Phys. Chem. A*, 125(33):7266−7277, 2021.

G. Meizyte, P. A. J. Pearcy, P. Watson, E. I. Brewer, A. E. Green, M. Doll, O. Duda, and S. R. Mackenzie. An infrared study of gas-phase metal nitrosyl ion-molecule complexes. *J. Phys. Chem. A*, in preparation, 2022.

Other:

A. E. Green, S. Schaller, G. Meizyte, B. J. Rhodes, S. P. Kealy, A. S. Gentleman, W. Schöllkopf, A. Fielicke, and S. R. Mackenzie. Infrared study of OCS binding and size−selective reactivity with gold clusters, Au_n^+ ($n = 1$−10). *J. Phys. Chem. A*, 124(26):5389−5401, 2020.

E. I. Brewer, A. E. Green, A. S. Gentleman, P. W. Beardsmore, P. A. J. Pearcy, G. Meizyte, J. Pickering, and S. R. Mackenzie. An infrared study of CO_2 activation by holmium ions, Ho^+ and HoO^+. *Phys. Chem. Chem. Phys.*, 24(37):22716−22723, 2022.

Contents

1 Introduction **1**

1.1 Metal-Containing Clusters and Complexes 1

1.1.1 Motivation to Study 2

1.2 Cluster Source 4

1.2.1 Laser Ablation Source Variations 6

1.3 Reactivity and Structure of Metal-Containing Clusters and Complexes 8

1.3.1 Trapped Ion Electron Diffraction 8

1.3.2 Ion Mobility Studies 8

1.3.3 Infrared Action Spectroscopy 9

1.4 Thesis Overview 10

2 Experimental and Computational Methods **13**

2.1 Spectroscopic Theory 13

2.2 Infrared Action Spectroscopy 16

2.2.1 Infrared Spectroscopy 16

2.2.2 Time-of-Flight Mass Spectrometry 16

2.2.3 Principles of IR-(M)PD Spectroscopy 17

2.3 Oxford Experiment 18

2.4 Fritz Haber Institute in Berlin Experiment 21

2.5 Analysis in this Thesis 23

2.6 Density Functional Theory 24

2.6.1 Exchange-Correlation Functional 26

2.6.2 Basis Set 27

Part A. Individual Ligands on Transition Metal Clusters **29**

3 Free Electron Laser Infrared Action Spectroscopy of Nitrous Oxide Binding to Platinum Clusters, $Pt_n(N_2O)^+$ ($n = 1$–8) **31**

3.1 Introduction 32

3.2 Experimental and Computational Methods 34

3.3 Time-of-Flight Spectrum and Analysis 36
3.4 Potential Energy Landscapes 40
3.5 IR-MPD Spectra 40
3.6 N_2O Binding Motifs in Calculations 42
3.7 IR-Induced Reactivity 44
3.8 Summary and Conclusions 45

4 Infrared Study of Nitrous Oxide Adsorption on Gas-Phase Gold and Cobalt Clusters, $Au_n(N_2O)^+$ ($n \leqslant 7$) and $Co_n(N_2O)^+$ ($n \leqslant 5$) 47
4.1 Introduction 48
4.2 Experimental and Computational Methods 49
4.3 Reactivity of Gold Clusters 50
4.4 N_2O Binding Motifs in $Au_n(N_2O)^+$ Clusters 52
4.5 Reactivity of Cobalt Clusters 52
4.6 Summary and Conclusions 56

5 Cooperative Binding Effects of Oxygen and Carbon Monoxide on Anionic Gold Clusters, $Au_nO_2CO^-$ ($n = 2$–8, even n) 57
5.1 Introduction 58
5.2 Experimental and Computational Methods 61
5.3 Selective O_2 Binding in the Time-of-Flight Spectrum 64
5.4 IR-MPD Spectra 64
5.4.1 O_2 Stretch Region (1000-1200 cm^{-1}) 64
5.4.2 CO Stretch Region (1900-2200 cm^{-1}) 66
5.5 Cooperative Binding in the Calculations 67
5.5.1 O_2 Binding Motifs 67
5.5.2 CO Binding Motifs 71
5.5.3 Possibility of Coexisting Isomers 73
5.5.4 Binding Energy Considerations 74
5.6 Summary and Conclusions 75

Part B. Multiple Ligands on a Single Metal Centre 77

6 NO Binding at Group 9 Metal Centres: $Co(NO)_n^+$ and $Rh(NO)_n^+$ ($n \leqslant 8$) 79
6.1 Introduction 80
6.2 Experimental and Computational Methods 83
6.3 Time-of-Flight Spectra 84
6.3.1 Cobalt 84

6.3.2 Rhodium . . . 86
6.3.3 Iridium . . . 86
6.4 IR-PD Spectra . . . 88
6.5 Plethora of Low-Lying Isomers . . . 90
6.6 IR-PD Spectra of Pure NO Clusters: $(NO)_n^+$ and $NO_2(NO)_m^+$ (n = 3−8, m = 2−9) . . . 100
6.6.1 Time-of-Flight Spectrum . . . 101
6.6.2 IR-PD Spectra . . . 102
6.6.3 Fragmentation Pathways . . . 106
6.7 Summary and Conclusions . . . 107

7 Energy Flow in Mixed Ligand Complexes: $Rh(CO)_n(N_2O)_m^+$ (n = 1−5, m = 1−4) 109
7.1 Introduction . . . 110
7.2 Experimental and Computational Methods . . . 113
7.3 Time-of-Flight Spectrum . . . 114
7.4 IR-PD Spectra . . . 115
7.5 Calculated Structures . . . 118
7.6 Internal Energy Distributions . . . 124
7.7 Single vs. Multiple Photon Study . . . 126
7.8 Comparison with Gold . . . 127
7.9 Summary and Conclusions . . . 129

8 Energy Flow in Isotopically-Enriched Metal Ligand Complexes: $Au(^{12/13}CO)_n(N_2O)_m^+$ (n = 2−3, m = 1−2) 131
8.1 Introduction . . . 132
8.2 Experimental and Computational Methods . . . 133
8.3 Time-of-Flight Spectrum . . . 134
8.4 IR-PD Spectra . . . 137
8.5 Vibrational Modes of the Molecules . . . 139
8.6 Summary and Conclusions . . . 143

9 Conclusions 147

Appendices 151

Appendix A 153

Bibliography 155

Chapter 1

Introduction

1.1 Metal-Containing Clusters and Complexes

The main focus of this thesis is enhancing the knowledge of structure and reactivity of gas-phase metal-containing small clusters and complexes with atmospherically relevant adsorbates. Two types of systems will be presented: decorated transition metal (TM) clusters of multiple TM atoms with a single adsorbate; and metal-containing complexes − a single TM ion typically with more than one ligand attached. Clusters are defined as bridging intermediates between atoms and macroscopic aggregates and contain anywhere from few to a few thousand atoms [1]. This thesis, however, is only concerned with small metal clusters (up to and including ten atoms) and larger ones will not be discussed.

Metal-containing clusters and complexes can be produced controllably and characterised in terms of size, composition, and charge state. Upon varying these, the chemical and physical properties of these clusters and complexes can differ greatly, and in some cases do not follow smooth trends within the periodic group or period as well as show dramatic differences in reactivity upon addition of even one atom [1–4]. Famously, these are systems in which "every atom counts" [5]. As a result, the size, composition, and charge state are tunable properties, *e.g.* in terms of chemical reactivity in the $Ag_nAu_m^{+/-}$ $(n + m = 3)$ system [6].

In such a small size regime, quantum effects [1] become more important and the properties of these metal-containing clusters and complexes are in many instances

different from those of bulk material, *e.g.* small rhodium clusters typically possess large magnetic moment whilst bulk rhodium is non-magnetic [4]. One of the most famous examples is gold; this is known for its inertness in its bulk form, but supported gold nanoparticles have been found to participate in the CO oxidation at ambient temperature [7], with a likely reason being different electronic configurations of the surface Au atoms where the catalytic reaction takes place [8].

1.1.1 Motivation to Study

In addition to fulfilling chemical curiosity, gas-phase metal-containing small clusters and complexes offer an elegant approach to study fundamental interactions between the catalytically active metal and atmospheric gas of interest at the molecular level, *e.g.* Harding *et al.* [9] studied the activation of CH_4 on Pt_n^+ ($n = 3$–5) clusters and found that the dehydrogenation pathways are similar to those on the extended surface [10], where dissociative adsorption proceeds through a shallow minimum and the energetic barriers for the dehydrogenation and desorption processes are similar. This demonstrates how cluster studies can gain insight into the molecular activation in real catalysts.

Understanding of the fundamental interactions yields powerful insight into the metal-ligand relationships that are important for the production of next-generation catalysts. The exact chemical environment in industrial catalysts cannot be replicated by tractable metal-containing small clusters and complexes, however, they can offer basis for understanding the fundamental interactions as the effects obscuring them, *e.g.* interactions with the substrate, solvation/aggregation, and counter-ion effects, are not present [11].

An overview of studies of supported metal clusters and their catalytic activity has been published by Watanabe [12]. Catalytic ability is dependent on the electronic and geometric structure of the unsupported clusters as well as their interaction with the support, and the author encourages the study of unsupported clusters due to their promising ability to shed light on the underlying mechanisms in catalytic systems.

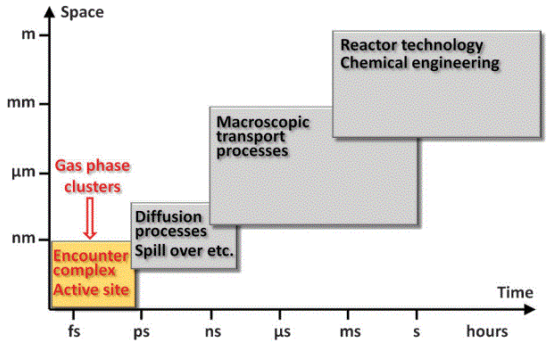

Figure 1.1.1: A schematic of the space and time dimensions of the processes involved in heterogeneous catalysis. Reproduced from Ref. [3] (https://doi.org/10.1039/C2CP40660H) with permission from the PCCP Owner Societies.

Figure 1.1.1 displays the space and time dimensions of the processes involved in heterogeneous catalysis. As indicated, the gas-phase clusters are regarded as the 'active site' [13] in the catalyst. This concept was coined by Taylor [14] in 1925 and signifies a physical place where the catalytic process(es) take place, *e.g.* defect sites that can be approximated by a few atoms due to their sub-nanometer scale. Moreover, the chemical bond breaking and forming, which happen during the catalytic transformation, are highly localised [15]. An 'encounter complex' with regards to the gas-phase clusters is a complex where the cluster that represents the active site in a catalyst adsorbs the reactant gas of interest, *i.e.* a metal cluster-molecule complex [3].

Even on metal clusters without a substrate, full catalytic cycles have been observed, *e.g.* CO oxidation by O_2 on the Au_6^- clusters by Wallace *et al.* [16] (Figure 1.1.2) and CO oxidation/N_2O reduction on Pt_n^+ ($n = 6-8$) by Balaj *et al.* [17]. Complementary to the experiments, the gas-phase metal-containing small clusters and complexes can be modelled by quantum chemical methods and results readily compared [18].

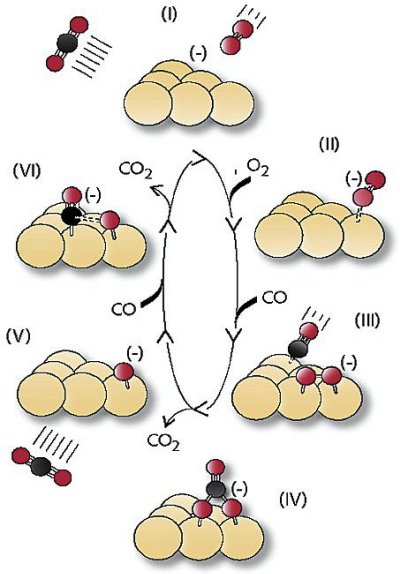

Figure 1.1.2: A schematic of the catalytic cycle of CO oxidation by O_2 on the Au_6^- clusters. Reprinted with permission from [16] (https://doi.org/10.1021/ja0175439). Copyright 2002 American Chemical Society.

1.2 Cluster Source

To produce complexes and clusters of a variety of sizes requires a cluster source which, according to the different techniques involved for getting the metal into the gas phase, can be classified into: 1) thermal heated oven, 2) electrospray ionisation, 3) laser ablation (vaporisation), and 4) sputtering sources [4].

The experimental studies presented in this thesis include the use of laser ablation sources, developed independently in 1981 by Smalley and coworkers [19], who used it to discover fullerenes in 1985 [20], and by Bondybey and coworkers [21], who coupled it with laser-induced fluorescence (LIF). The metal clusters produced following laser vaporisation are thermally excited, and usually the metal target laser ablation in presence of inert carrier gas is combined with supersonic expansion into vacuum. In this way, substantial densities of thermalised clusters are produced *via* three-body collisions [22]. An initial two-body collision is required for the cluster growth to take place, however, without a simultaneous third-body collision with inert gas, such as He or Ar, the excess energy that is released upon exothermic formation

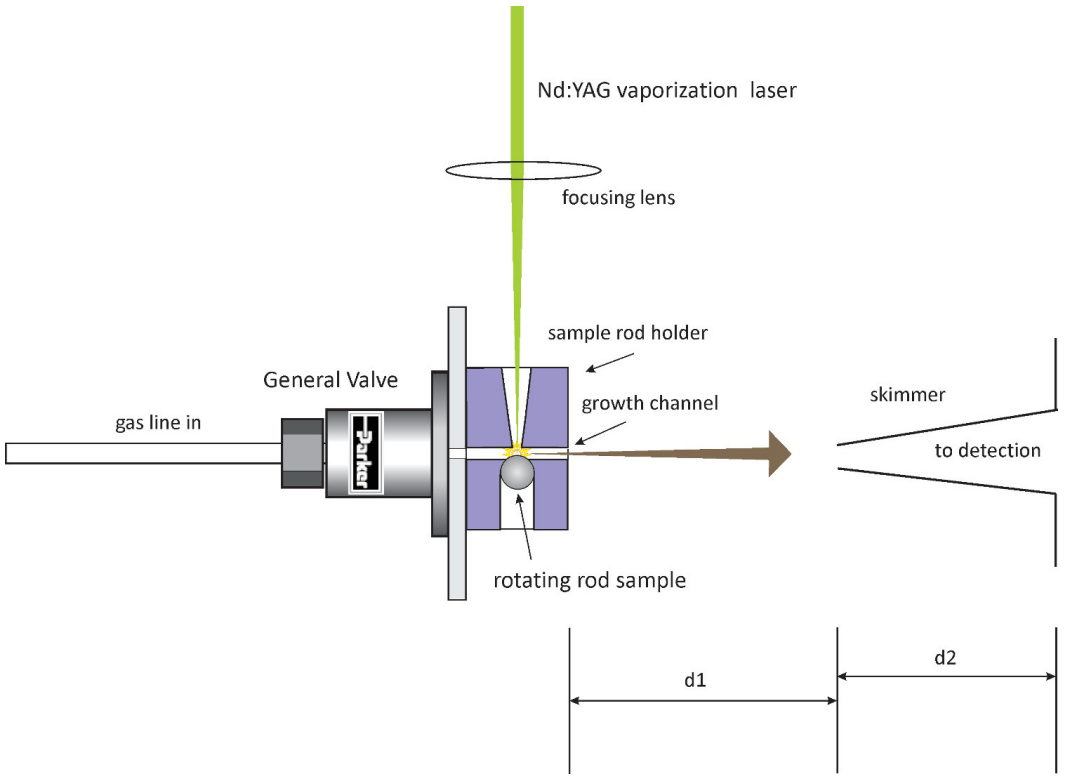

Figure 1.2.1: "Standard" laser ablation cluster source; d1 and d2 denote the nozzle-to-skimmer and skimmer-to-wall distances, respectively. Reprinted from [23] (https://doi.org/10.1063/1.3697599), with the permission of AIP Publishing.

of new metal-metal bonds would not be disseminated. Such a case would result in an instant fragmentation of the two reactants upon a collision. Thus, an initial three-body collision is required to form a dimer, and for further cluster growth multiple two-body collisions can suffice. The Smalley type laser ablation source termed as "standard" is shown in Figure 1.2.1. It is optimised towards producing large metal clusters due to inclusion of the 'growth channel' that promotes extensive metal-metal collisions in presence of cooling collisions with carrier gas molecules [23].

The temperature (or internal energy distribution) of produced metal clusters can be lowered by cooling down the cluster channel with liquid nitrogen. This promotes larger cluster production, *e.g.* up to Na_{200} [24], and permits adsorption of weakly-bound ligands [25]. The cluster temperature is important in determining their

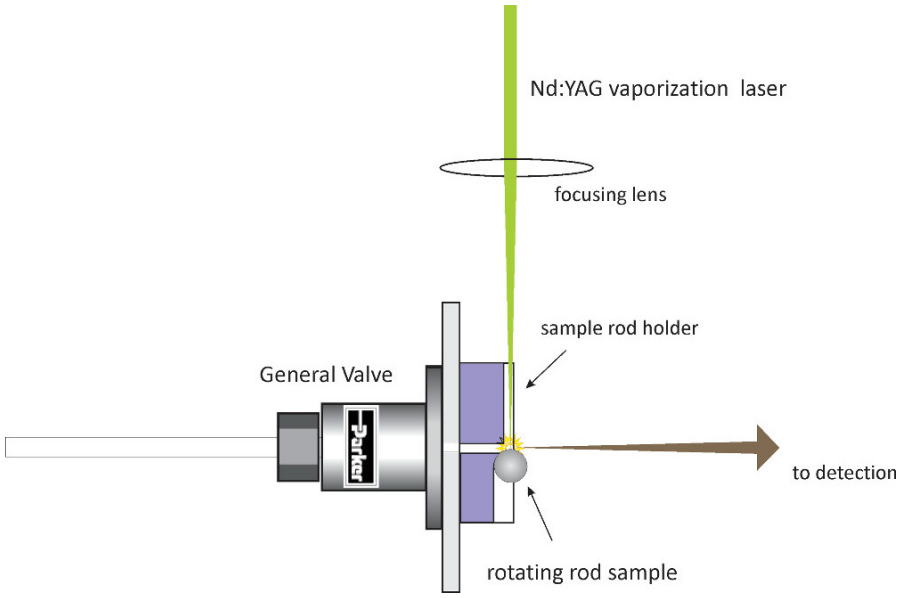

Figure 1.2.2: "Cutaway" laser ablation cluster source. Reprinted from [23] (https://doi.org/10.1063/1.3697599), with the permission of AIP Publishing.

reactivity; there is more chance to overcome the reaction barriers by clusters with more internal energy.

The laser vaporisation source usually includes the use of pulsed (Q-switched) second harmonic 532 nm light from the Nd:YAG laser that ablates a rotating metal disc or rod in presence of inert carrier gas pulses. Rotating the metal target helps to maintain similar efficiency of the metal plasma generation throughout the experiment and prolongs the lifetime of the target [26, 27]. Upon ablation of the metal target, plasma is discharged that contains neutral and charged metal atoms along with ejected electrons. A Q-switched laser is normally used due to its ability to achieve sufficiently high pulse energies for metal evaporation as well as for easier timing control with the buffer gas pulses that carry the clusters [4].

1.2.1 Laser Ablation Source Variations

A different type of laser ablation cluster source is termed "cutaway" (Figure 1.2.2); it is optimised for producing solvated metal atom complexes as the design allows

for the most efficient supersonic expansion needed for weakly-bound (especially, messenger-tagged) complexes. The growth channel present in the "standard" cluster source (Figure 1.2.1) is absent in the "cutaway" design, and this permits expansion closer to that one of free jet (free jet expansion produces coldest molecular beams) [23]. Using this type of laser ablation source, Reddic and Duncan produced the Mg-Ne^+ complex with rotational temperature of 4K [28].

Duncan and coworkers observed an improvement of the signal for some systems upon varying the distance between the metal rod sample and the ablation laser. As a result, a close variant to the "cutaway" source was constructed that involves a small channel region before the laser and the rod offset from the position of the gas pulse. This design was termed as the "offset" source (Figure 1.2.3), and proved to work well for the generation of $M(CO)_n^+$ complexes by Duncan and coworkers [29–31]. Even though it is not clear why this source works better for some systems, the authors suggested it might be due to a smaller extent of cation-electron recombination in the expansion [23].

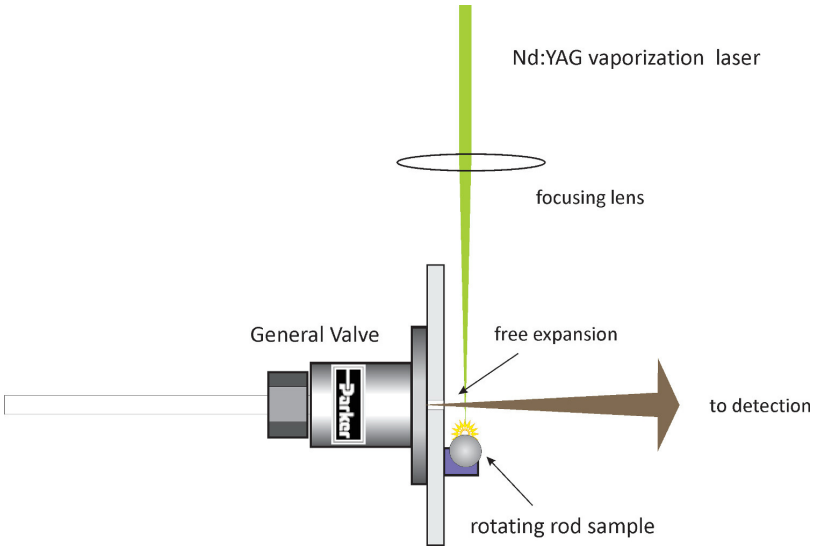

Figure 1.2.3: "Offset" laser ablation cluster source. Reprinted from [23] (https://doi.org/10.1063/1.3697599), with the permission of AIP Publishing.

1.3 Reactivity and Structure of Metal-Containing Clusters and Complexes

Mass spectrometry lies at the heart of studying the reactivity of metal-containing clusters and complexes; a review by Johnson and McIndoe [32] describes a selection of mass spectrometric techniques, such as field desorption (FD) and electron impact (EI), inductively coupled plasma (ICP), and electrospray (ESI) ionisations. Mass spectrometry combined with other experimental methods can also help to determine the structural parameters. The next Sections 1.3.1-1.3.3 contain descriptions of the most widely used techniques for determining the stucture and reactivity of metal-containing clusters and complexes.

1.3.1 Trapped Ion Electron Diffraction

The trapped ion electron diffraction (TIED) technique was developed by Parks and coworkers [33] to study the C_{60}^+ cluster and has been used extensively to predict the geometries of clusters and complexes of interest, *e.g.* Au_n^- ($n = 11-24$) by Xing *et al.* [34] and $(CsI)_nCs^+$ ($n = 30-39$) by Krückeberg and Schooss *et al.* [35]. This technique utilises a radio-frequency (RF) quadrupole ion trap in which an electron diffraction pattern for the mass-selected ions of interest is measured by a microchannel plate (MCP) detector and recorded by a charged-coupled device (CCD) camera, and can be compared with scattering functions of computationally predicted geometries. It is better suited for larger and heavy nuclei clusters due to their respectively larger electron scattering cross sections [36, 37].

1.3.2 Ion Mobility Studies

Ion mobility is a separation technique that involves measuring the time it takes for a molecular ion to drift through a buffer gas-filled cell steered by an electric field, with larger ions as well as planar isomeric forms taking a longer time due to their respectively larger collision cross section. This drift time can be compared to those of simulated isomers, thus providing information about their geometrical parameters.

This technique was first developed by Mason and McDaniel [38] and later combined with modern mass spectrometry by Bowers and coworkers [39, 40]. The structures of bare metal clusters such as Ag_n^+ ($n < 12$) [41] and Au_n^- ($n < 13$) [42] by Kappes and coworkers in addition to a range of charged Si, Al, Sn, and Pb by Jarrold and coworkers [43–46] have been explored using this method. A review by Kappes and coworkers [47] reports geometric structural assignments of $Au_n^{+/-}$ ($n = 3{-}20$) clusters mainly by TIED and ion mobility studies with theoretical considerations.

1.3.3 Infrared Action Spectroscopy

Vibrational spectroscopy [48–50] is used to determine the structure of chemical species, including metal-containing clusters and complexes, as well as the binding of molecules to them − depending on which infrared (IR) region is scanned. The first IR spectra of gas-phase metal complexes was recorded by means of infrared-multiple photon dissociation (IR-MPD) spectroscopy by Zakin *et al*. for the $Fe_n(CH_3OH)_m$ ($n = 1{-}12$, $m = 0{-}2$) system [51]. In these early studies, line-tunable CO_2 lasers were used that were restricted in the available IR range as well as limited to solely inducing multiple photon processes.

With development of free electron lasers (FEL) as the source of IR irradiation, the wavenumber range was expanded to include far-IR (FIR) and mid-IR regions [52, 53] whereas new tabletop lasers allow single photon processes to be explored [36], *e.g*. using H_2 tagging [54, 55]. Tagging the complex with a weakly-bound molecule that has a negligible impact on the structure is called the 'messenger technique' [56] and often result in improved resolution of the measured spectra, *e.g*. in the Mizuse *et al*. [57] study of small protonated water clusters. Such improved resolution stems from the time-energy uncertainty principle, which states that the energy is completely defined only when the lifetime of an excited state is infinite. Thus, a shorter lived excited state, such as in the case of a single instead of multiple photon absorption for weakly-bound moieties, leads to a better resolved spectrum. More details on the principles of free electron and tabletop IR lasers are given in Chapter 2.

FIR-MPD spectroscopy has been applied to study the metal-metal bond vibrations in small gas-phase isolated clusters [25], for example, FIR-MPD spectra of the Au_7, Au_{19}, and Au_{20} clusters were recorded by Gruene *et al.* [58] *via* Kr tagging and plausible structures were identified with the help of density functional theory (DFT) simulations. In this region, only free electrons lasers can be utilised, and due to strong metal-metal bonds tagging with a messenger molecule is usually employed [36].

The mid-IR region is associated with the vibrations of molecules and, as such, is diagnostic of their binding to the metal-containing clusters and complexes, and can reveal reactivity pathways, *e.g.* OCS binding to isolated gold cluster cations, Au_n^+ ($n = 1-10$), was explored by Green *et al.* [59], where size-selective IR-driven OCS decomposition was observed on even n clusters.

Other variants of the infrared action spectroscopy include resonance enhanced multiple photon electron detachment (IR-REMPED) for anions, resonance enhanced multiple photon ionization (IR-REMPI), and ultraviolet two colour ionization (IR/UV-2CI) for neutrals. All these techniques involve a change in the charge state after the absorption of infrared light [36].

1.4 Thesis Overview

The next chapter 'Experimental and Computational Methods' contains theoretical background of IR-(M)PD spectroscopy and DFT − techniques used to study the gas-phase metal-containing small clusters and complexes with atmospherically relevant adsorbates in this thesis. The two experimental setups used in Oxford and the Fritz Haber Institute (FHI), Berlin, are also described in Chapter 2.

The results chapters (Chapters 3-8) are grouped into:

Part A. Individual Ligands on Transition Metal Clusters;

Part B. Multiple Ligands on a Single Metal Centre.

Part A is comprised of three chapters describing experiments carried out in the FHI, Berlin:

> Chapter 3. Free Electron Laser Infrared Action Spectroscopy of Nitrous Oxide Binding to Platinum Clusters, $Pt_n(N_2O)^+$ ($n = 1$–8);
>
> Chapter 4. Infrared Study of Nitrous Oxide Adsorption on Gas-Phase Gold and Cobalt Clusters, $Au_n(N_2O)^+$ ($n \leqslant 7$) and $Co_n(N_2O)^+$ ($n \leqslant 5$);
>
> Chapter 5. Cooperative Binding Effects of Oxygen and Carbon Monoxide on Anionic Gold Clusters, $Au_nO_2CO^-$ ($n = 2$–8, even n).

The studies described in Chapter 3 and Chapter 4 have been published by Meizyte *et al*. [60] and in collaboration with Cunningham *et al*. [61], respectively. The reactivity and activation of N_2O on large cationic Pt, Au, and Co clusters are examined whereas Chapter 5 explores the O_2 and CO interactions on large cationic gold clusters.

Part B comprises three chapters, the experiments for which were conducted in the Oxford laboratory:

> Chapter 6. NO Binding at Group 9 Metal Centres: $Co(NO)_n^+$ and $Rh(NO)_n^+$ ($n \leqslant 8$);
>
> Chapter 7. Energy Flow in Mixed-Ligand Complexes: $Rh(CO)_n(N_2O)_m^+$ ($n = 1$–5, $m = 1$–4);
>
> Chapter 8. Energy Flow in Isotopically-Enriched Metal Ligand Complexes: $Au(^{12/13}CO)_n(N_2O)_m^+$ ($n = 2$–3, $m = 1$–2).

Chapter 6 investigates NO binding to the Co^+ and Rh^+ metal centres. New additions to the Oxford instrument, notably the inclusion of parent ion mass selectivity, allows the study of mixed-ligand complexes described in Chapter 7. Chapter 8 is a continuation of the mixed-ligand gold study published as Green *et al*. [62]. All chapters in Part B are currently being prepared for publication.

Finally, the summary and future directions of all presented work are given in the 'Conclusions' chapter.

Chapter 2

Experimental and Computational Methods

2.1 Spectroscopic Theory

The stretches in a diatomic molecule can be understood in the context of the ball and spring model. Here, the ball and spring are representative of atoms and bonds, respectively, and as such, small vibrational motion of a diatomic molecule can be approximated by a simple harmonic oscillator (SHO), to which Hooke's law applies:

$$F = -kx, \tag{2.1.1}$$

where k is the spring constant and x is the resulting displacement of a spring when F amount of force is applied. The shape of the harmonic potential (Figure 2.1.1) is of the form:

$$\begin{aligned} V(x) &= \frac{1}{2}kx^2, \\ x &= R - R_e, \end{aligned} \tag{2.1.2}$$

where R and R_e denote the internuclear and internuclear equilibrium distances, respectively.

The energy eigenvalues, the vibrational energy levels, E_υ, are given by:

$$E_\upsilon = h\nu(\upsilon + \frac{1}{2}), \tag{2.1.3}$$

where υ is the vibrational quantum number (υ = 0, 1, 2, ...). The classical vibrational frequency, ν, can also be expressed as:

$$\begin{aligned} \nu &= \frac{1}{2\pi}\left(\frac{k}{\mu}\right)^{1/2}, \\ \mu &= \frac{m_1 m_2}{(m_1 + m_2)}, \end{aligned} \tag{2.1.4}$$

where μ is the reduced mass (m_1 and m_2 are masses of the atoms in a diatomic molecule) and k is the force constant; k is analogous to the spring constant in Equation 2.1.1, and indicates the strength of a bond in the context of the ball and spring model. In this model, k increases with the bond strength and results from the electronic bonding in the molecule, which dictates the form of the intermolecular potential; k is not dependent on the isotopic substitution of atoms in molecules but overall, ν is, due to the reduced mass term.

Equation 2.1.3 for the vibrational energy levels can also be expressed in terms of the vibrational term values, $G(\upsilon)$:

$$\frac{E_\upsilon}{hc} = G(\upsilon) = \omega_e(\upsilon + \frac{1}{2}), \tag{2.1.5}$$

where ω is the vibrational wavenumber. As is evident from Equations 2.1.3 and 2.1.5, the vibrational energy levels (or term values) are equally spaced and this model does not allow for dissociation. (Figure 2.1.1).

For a more realistic model of molecular bonding, the effects of mechanical anharmonicity needs to included in the treatment of molecular vibrations. The Morse potential [63] is frequently used for the approximation of the anharmonic potential, and its shape (Figure 2.1.1) is expressed as:

$$\begin{aligned} V(x) &= D_e[1 - exp(-ax)]^2, \\ x &= R - R_e, \\ D_e &\simeq \frac{\omega_e^2}{4\omega_e x_e}, \end{aligned} \tag{2.1.6}$$

where the width of the potential is inversely proportional to a and D_e is the dissociation energy; both are constants associated with a specific electronic state of the molecule.

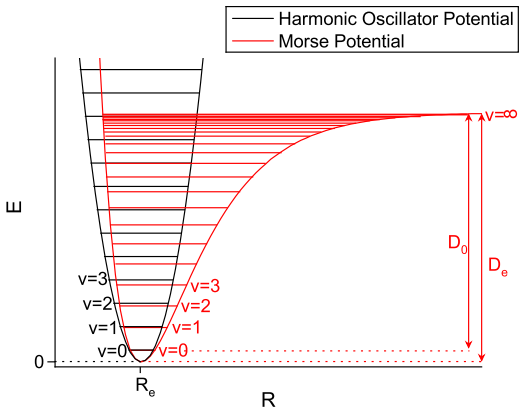

Figure 2.1.1: Shapes of the harmonic (in black) and anharmonic (in red) oscillator potentials with the spacing of energy levels shown. R_e is the internuclear equilibrium distance; D_0 and D_e denote the dissociation energies relative to the zero-point and equilibrium potential energies, respectively.

Taking this modification of $V(x)$ into account, Equation 2.1.5 becomes:

$$G(v) = \omega_e(v + \frac{1}{2}) - \omega_e x_e(v + \frac{1}{2})^2 + \omega_e y_e(v + \frac{1}{2})^3 + ..., \tag{2.1.7}$$

where ω_e denotes the vibrational wavenumber of a simple harmonic oscillator undergoing infinitesimal displacement from the equilibrium and $\omega_e x_e, \omega_e y_e, ...$ are the anharmonicity constants.

The bonds in a molecule are vibrating at specific frequencies; the higher the frequency, the weaker the bond. We can discuss these vibrations as local modes (localised on a specific bond) or normal modes (coherent motion of all or some atoms in a system), and each normal mode in a molecule can be considered as an independent harmonic oscillator with its own specific μ and k. Generally, if there are N atoms, the molecule has 3N degrees of freedom (each atom can move in x, y, and z coordinates). However, since all N are bonded, these modes also include the rotational and vibrational modes. The rotational motion can be described by rotations about three axes for non-linear molecules and two axes for linear molecules (since rotation about its axis has a zero moment of inertia). This results in the number of normal vibrational modes of 3N-6 for non-linear and 3N-5 for linear molecules.

2.2 Infrared Action Spectroscopy

2.2.1 Infrared Spectroscopy

The infrared region in the electromagnetic spectrum is the fingerprint region for molecular vibrations. The basic concept of traditional infrared spectroscopy lies in the Beer-Lambert law that is used as the means to determine how much light a sample absorbs:

$$A = \varepsilon cl = log_{10}\frac{I_0}{I}, \tag{2.2.1}$$

where A is the absorbance, ε is the molar absorption coefficient, c the molar concentration, l the optical path length, and I_0, I are the incident and transmitted light intensity, respectively.

In the gas phase, however, the number of clusters produced per laser pulse is relatively small, compared with the liquid phase, and the fraction of photons absorbed typically trivially small. Instead, in this thesis, action spectroscopy is used which is an indirect spectroscopic method that measures some change in the system that occurs as a result of photon absorption. In infrared-(multiple) photodissociation spectroscopy, the fragmentation of a molecule *via* mass spectrometry is measured, and the sensitivity of mass spectrometry is harnessed for the purpose of spectroscopy.

2.2.2 Time-of-Flight Mass Spectrometry

In the experimental studies described in this thesis, mass spectrometry has been employed to characterise clusters and complexes. Specifically, time-of-flight (ToF) mass spectrometry is used for the characterisation of singly charged chemical species. In this method, ions are accelerated through a constant potential difference V, and the kinetic energy gained by the ions can be expressed as:

$$zeV = \frac{1}{2}mv^2, \tag{2.2.2}$$

where ze is the charge, m is the mass, and v is the velocity of the ions. After the acceleration, the ions enter a field-free drift region, where they are

separated according to their velocity which is dependent on the mass-to-charge ratio (m/z). The mass spectrum is recorded by measuring the time of arrival of ions at the MCP detector:

$$t = C\sqrt{m} + t_0, \tag{2.2.3}$$

where C is a constant dependent on the experimental conditions, such as the electric fields applied in the instrument, and t_0 can be found from the recorded mass spectra analytically. The arrival at Equation 2.2.3 is by substituting $v = \frac{d}{t}$ in the Equation 2.2.2; d is the distance and t is the time travelled by the ions.

In this thesis, the time-of-flight mass spectra recorded and presented in Chapters 3-5 can be analysed and compared as it is whereas the mass spectra given in Chapters 6-8 may not produce the correct relative areas of the peaks − the spectra are constructed as overlays of individual ToF spectra recorded with various extraction from the reaction channel timings (quick extraction results in smaller clusters formed).

2.2.3 Principles of IR-(M)PD Spectroscopy

When a molecule is irradiated with infrared light with a frequency that matches the vibrational frequency of some mode in that molecule, this energy can be absorbed *via* that mode. In order to better explain the principles behind IR-(M)PD, a simplified picture of a molecule that only contains local modes is given below. Figure 2.2.1.a) depicts a photon absorption in the L2 ligand that is resonant with incoming radiation. Rapid intramolecular vibrational energy redistribution (IVR) has to take place as the energy has to get from the ligand vibration into the weak Me$\cdots$L2 bond. If this injected photon has an energy greater or equal to the binding energy (BE) of L2 to the metal centre, the Me$\cdots$L2 bond can be broken and the L2 ligand lost (2.2.1.c)). Multiple photons may be needed in the situation where the binding energy of a ligand is greater than that of the incoming photon. In order for the system to be available for multiple photon absorption, IVR has to

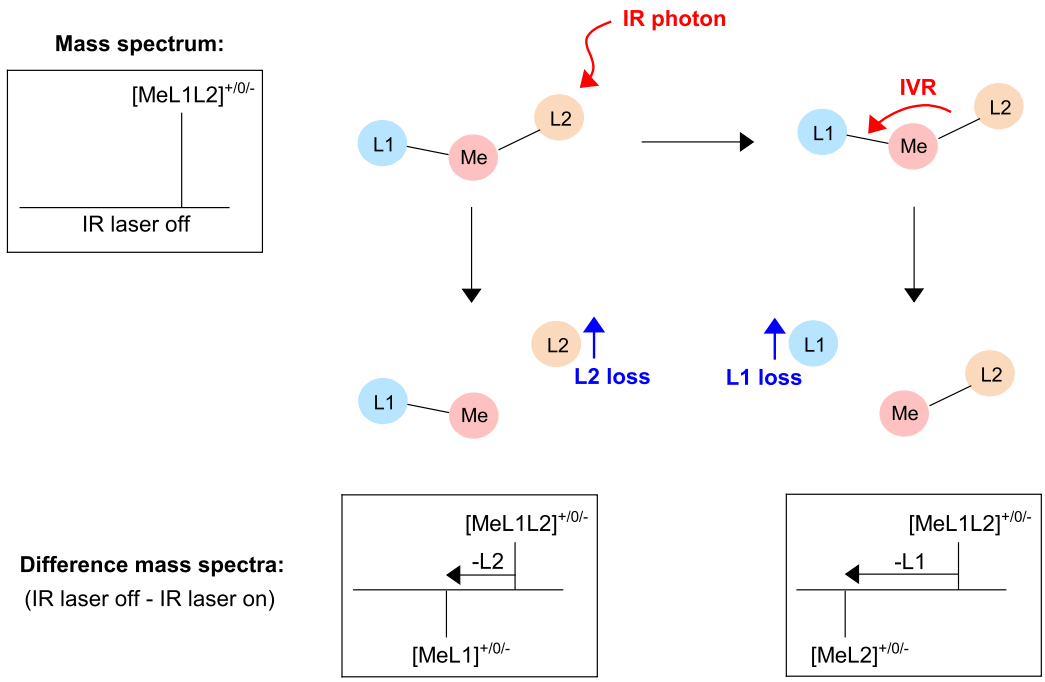

Figure 2.2.1: A schematic showing the principles behind IR-(M)PD spectroscopy of a metal-containing mixed ligand complex $[MeL1L2]^{+/0/-}$.

take place to leave the L2 fundamental available for absorption of a second photon (b)). In which case, the energy can flow to break another bond in the complex and this results in the loss of ligand L1 (d)).

In order to build a spectrum, the molecule is irradiated with tunable IR radiation. At each frequency step, a mass spectrum is recorded with and without the infrared light, and, a difference mass spectrum is constructed as a function of the photon energy.

2.3 Oxford Experiment

The experiments described in this thesis were performed using two experimental setups, the differences of which will be highlighted in this chapter. The Oxford experimental setup, visualised in Figure 2.3.1, involves a "cutaway" cluster source (Section 1.2.1) and is optimised for producing complexes containing a single metal atom with multiple ligands adsorbed on it. During the experiment, a rotating metal

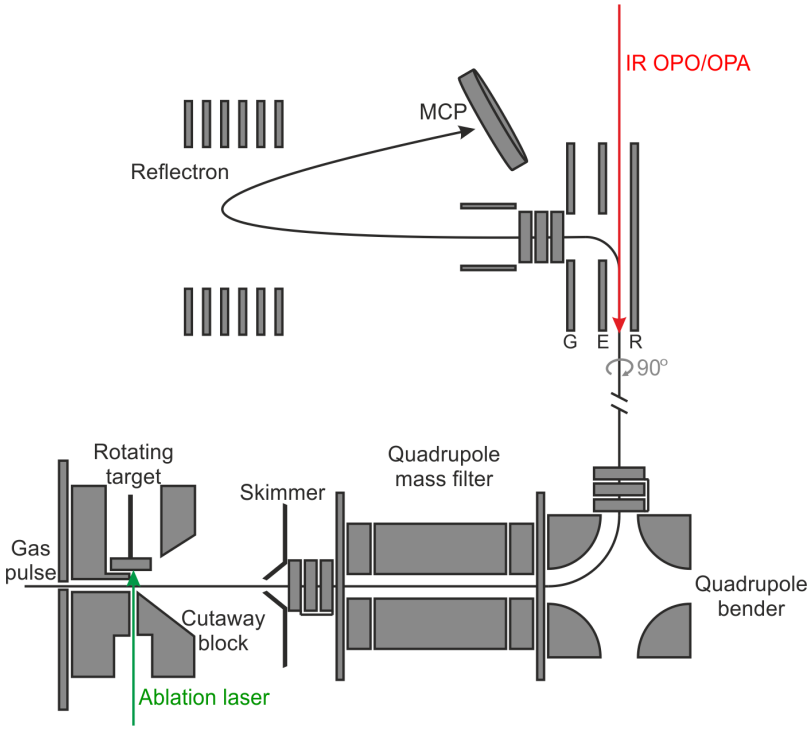

Figure 2.3.1: A schematic of the Oxford experiment.

disc target is ablated (by a pulsed 532 nm Nd:YAG laser operating at 10 Hz) in the presence of inert gas (*e.g.* Ar) seeded with the ligand of interest (usually 1%-5%) from a pulsed solenoid valve (Parker-Hannifin General valve, series 9). Singly charged and neutral complexes form by colliding with each other as well as cool by collision with inert gas molecules for stabilisation. Afterwards they form a molecular beam by weak supersonic expansion into vacuum and the beam is collimated by the skimmer.

Parent ion mass selection is provided by the arrangement of quadrupole mass filter (QMF) and bender (QMB) (Extrel 150-QC). The QMF consist of four rod electrodes arranged in a collinear manner to which direct current (DC) and radio frequency potentials are applied for the opposite rod pairs. 'RF only' mode allows all ions to pass through the QMF whereas adjusting the RF and DC potentials result in "stable" trajectories of ions with specific m/z values and these are transmitted through; ions with "unstable" trajectories are ejected. The main benefits of mass selectivity include better resolved spectra recorded against zero background in

the fragmentation daughter channel(s). In addition, mass selection permits the investigation of fragmentation dynamics.

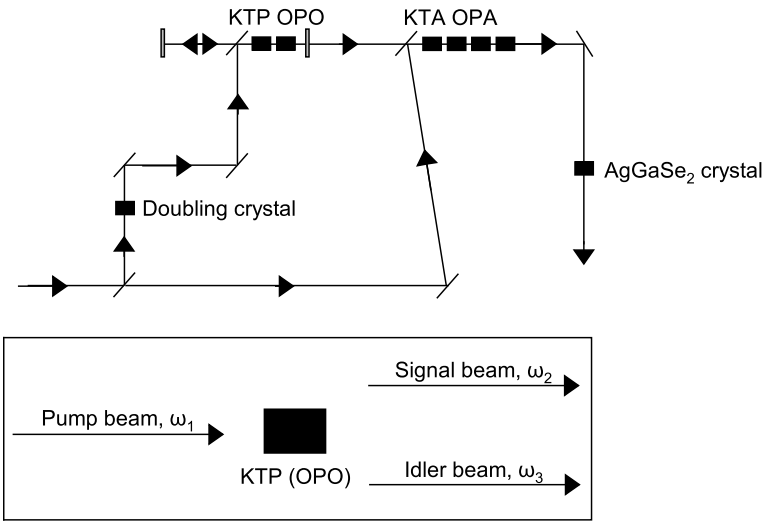

Figure 2.3.2: Simplified diagram of the OPO/OPA system showing a doubling crystal that converts the incoming 1064 nm radiation to a 532 nm beam, two KTP and four KTA crystals at the OPO and OPA stages, respectively, as well as the $AgGaSe_2$ crystal. The principles behind OPO are also illustrated. The pump beam with ω_1 frequency is converted to two lower energy beams − signal, ω_2, and idler, ω_3, with condition $\omega_1 = \omega_2 + \omega_3$.

The infrared light originates from a tabletop optical parametric oscillator/amplifier (OPO/OPA) system (LaserVision) pumped by a 1064 nm Nd:YAG laser (Continuum Powerlite Precision II), and collinearly counterpropagates to the molecular beam. A shutter is used to block the IR light when recording IR off signal in the mass spectrum. Figure 2.3.2 shows a simplified diagram of the OPO/OPA arrangement and illustrates the optical principles behind the non-linear crystals, such as $KTiOPO_4$ (KTP), $KTiOAsO_4$ (KTA), and $AgGaSe_2$ used here.

Inside the OPO/OPA system, the incoming 1064 nm beam passes through a beam splitter and one of the split beams is directed towards the doubling crystal. The resulting 532 nm beam pumps the OPO stage, where two beams of lower energy − signal, ω_2, and idler, ω_3, are generated by means of optical parametric generation obeying the total energy conservation principle. The orientation of KTP crystals is used to tune the values of ω_2 and ω_3 such that they satisfy the phase-matching

condition (due to conservation of the momentum). The OPO stage is configured as a linear optical cavity with light oscillating within, and the idler beam is then used to pump the OPA stage along with the non-split 1064 nm pump beam. At the OPA stage, the idler beam becomes the signal and is amplified as well as generates a new idler beam *via* difference frequency generation. In the experiments presented in this thesis, the idler beam was used, which corresponds to the infrared light range of 2000-4700 cm^{-1}. For some studies, the $AgGaSe_2$ crystal was introduced into the system in order to reach the 1500-2000 cm^{-1} range.

The commercial time-of-flight mass spectrometers (R. M. Jordan Co.) used for the experiments in this thesis are based on the linear Wiley and McLaren design [64], but modified to include a reflectron [65]. The pulsed grid made of R − repeller, E − extractor, and G − ground guides the ions as they enter the reflectron region (2.3.1). The reflectron allows for a better resolution due to the V-shaped trajectory of the ions achieved by applying an electric field. Ions with the same m/z ratio have different kinetic energies, and the distance travelled into the reflectron's electric field will differ accordingly so that they arrive at the MCP detector at the same time.

2.4 Fritz Haber Institute in Berlin Experiment

The experimental setup of the Berlin experiment is optimised for producing multiple metal atom clusters with a single ligand adsorbed on them in a "standard" cluster source (Section 1.2). A rotating metal rod target is ablated by a 532 nm Nd:YAG laser (10 Hz) in presence of inert carrier gas pulses (He used here) delivered by a Jordan valve (provides a shorter pulse than the solenoid valve allowing for a higher backing pressure [66]). If the outcome is more than one type of ligand adsorbed on the metal clusters, additionally, another atmospheric gas of interest is seeded in this Ar pulse. The main reaction gas of interest is introduced *via* an additional late-mixing valve downstream from the ablation point. The clusters form by collisions of metal and gas molecules as well as cool by multiple collisions with carrier gas, and, if needed to minimise the reactions taking place and enhance sticking probabilities,

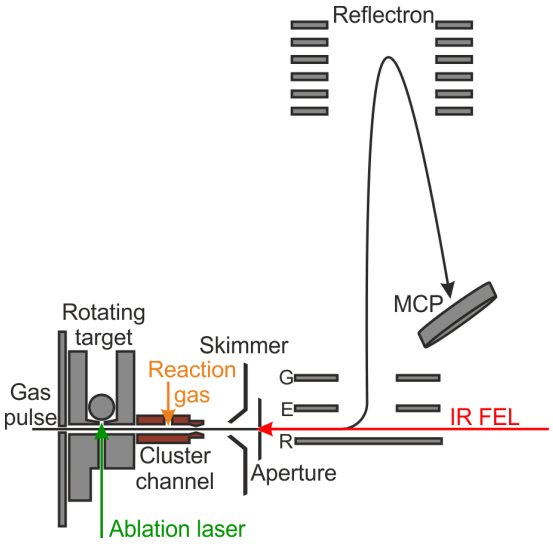

Figure 2.4.1: A schematic of the Berlin experiment; adapted from [36].

it is possible to cool the cluster source by liquid nitrogen. The resulting molecular beam is collimated by the skimmer and supersonically expanded into the vacuum.

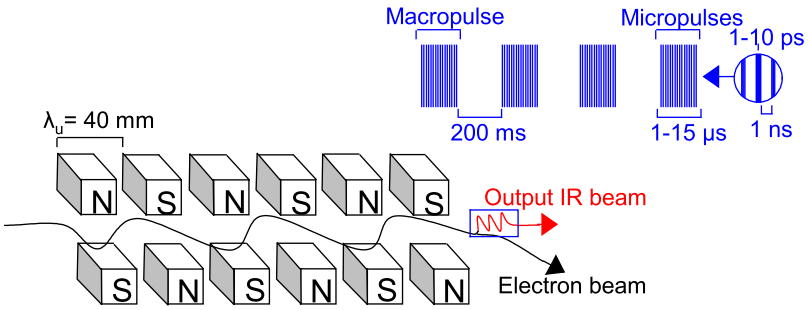

Figure 2.4.2: Structure of an undulator with the IR pulses.

Another difference to the Oxford experiment is the infrared light source which originates from the free electron laser [67, 68]. Figure 2.4.2 depicts a schematic for the production of IR beam in the undulator. An electron gun is used to produce a beam of electrons which are then accelerated close to the speed of light into the undulator. There, the magnetic field with a periodicity of $\lambda_u = 40$ mm, created by an arrangement of alternating pole magnets, compel the electron beam to wiggle and travel a sinusoidal path due to the Lorentz force. As a result, monochromatic but

incoherent electromagnetic radiation is emitted. Due to the undulator being placed in an optical cavity, the newly introduced electrons are forced to radiate coherently as well as with increased intensity. The wavelength of the produced radiation can be tuned by changing the physical distances of magnets. As shown in the figure, the output IR beam is made of macropulses of 1-15 μs duration and 200 ms delay between them that, in turn, are made of micropulses of 1-10 ps duration and 1 ns delay between them. The available range of the FHI FEL is 250-3400 cm^{-1} [67, 68].

2.5 Analysis in this Thesis

In Chapter 6, the spectra recorded are plotted in terms of normalised cross section of the given enhancement channel(s). The calculations were performed using a modified Beer-Lambert law [69]:

$$\sigma = -\frac{ln(1 - \frac{N_f}{\alpha N_0})}{\Phi}, \tag{2.5.1}$$

where σ is the absorption cross section, N_f and N_0 correspond to the intensity of the fragment and parent signals, respectively, and Φ is the photon flux. Equation 2.5.1 is related to Equation 2.2.1 (Beer-Lambert law). Absorbance is equivalent to the product of cross section and photon flux, $A = \sigma\Phi$, *i.e.* how much light has been absorbed. The ratio of the initial number of particles, N_0, to the final number of non-fragmented particles, N, is equivalent to the ratio of I_0 to I in Equation 2.2.1, thus $\sigma\Phi = log_{10}\frac{N_0}{N}$, and the number of the fragment particles is the difference between N_0 and N, $N_f = N_0 - N$. By making the substitution for $N = N_0 - N_f$ and simple mathematical manipulations, the expression for the modified Beer-Lambert law is derived. The α factor that describes the overlap between the ions and infrared light has not been determined, and the relative cross sections are used to present the experimental data.

In this thesis, the successive ligation binding energies, E_{bind}, (in Chapters 6 and 7) were calculated as:

$$E_{bind} = E_{MeL_n^+} - (E_{MeL_{n-1}^+} + E_L), \tag{2.5.2}$$

where E is the sum of electronic and zero-point energies; Me stands for a metal and L for n number of ligands. The energies substituted are those of the putative ground state structures that were let to optimise without constraints.

2.6 Density Functional Theory

Density functional theory is a quantum mechanical computational modelling technique and its description requires elementary quantum chemistry.

All conceivable information about a stationary state of the quantum system can be found within a wavefunction, Ψ. The Schrödinger equation for a molecular system with N electrons and M nuclei in its time-independent and non-relativistic form is written as:

$$\hat{H}\Psi_i(\mathbf{r}_N, \mathbf{R}_M) = E_i\Psi_i(\mathbf{r}_N, \mathbf{R}_M), \tag{2.6.1}$$

where E yields the total energy of the system in a specific stationary state and $\mathbf{r}$ with $\mathbf{R}$ describe the position of electrons and nuclei, respectively. The Hamiltonian, $\hat{H}$, the total energy operator, can characterise any given quantum system by:

$$\hat{H} = \hat{T} + \hat{V}, \tag{2.6.2}$$

where $\hat{T}$ and $\hat{V}$ are the kinetic and potential energy operators, respectively, and can be expressed as:

$$\hat{H} = \hat{T}_e + \hat{T}_n + \hat{V}_{ne} + \hat{V}_{ee} + \hat{V}_{nn}, \tag{2.6.3}$$

where the first two terms represent the kinetic energy of electrons and nuclei, and the other three − the attractive potential between nuclei and electrons, and the repulsive potential of electron-electron and nucleus-nucleus interactions, respectively.

However, in order to be able to solve this equation some simplification is required and is often achieved by the clamped-nuclei or Born-Oppenheimer approximation [70]. A system made up of atoms is treated as if the nuclei are fixed in space, *i.e.* they comprise a reference frame where only electrons move. The justification

for this approximation is that the nuclei are much heavier than the electrons and thus move much more slowly. And so, a simplified version of the Hamiltonian, the electronic Hamiltonian, can be written, in which the wavefunction is solely dependent on the coordinates of the electrons. Moreover, the kinetic and potential energy terms associated with the interactions of the nuclei become zero and a constant, respectively.

The basis of DFT is in the Hohenberg-Kohn theorems [71], and the main idea lies in expressing the electronic energy through electron density, $E[\rho(\mathbf{r})]$, which can be evaluated experimentally. The value of the square of the wavefunction is proportional to the probability of finding an electron at a given space and time. In order to correct for the non-local exchange potential (assumption of an average repulsion from all electrons), in DFT, the exact correlation between each pair of electrons is considered, and the general expression for the total energy of the system becomes:

$$E[\rho] = T_e[\rho] + V_{ne}[\rho] + V_{ee}[\rho]. \tag{2.6.4}$$

$T_e[\rho]$ and $V_{ee}[\rho]$ terms are unknown, and in order to tackle this problem Kohn and Sham (KS) formulated KS-DFT [72] where $T_e[\rho]$ is described by the kinetic energy of a system with non-interacting electrons that possess same density, $T_S[\rho]$. This term can be calculated precisely using a set of orbitals:

$$\rho(\mathbf{r}) = \sum_{i=1}^{N} |\varphi_i^{KS}|^2. \tag{2.6.5}$$

The total KS energy functional is:

$$E^{KS}[\rho] = T_S[\varphi_i^{KS}] + V_{ne}[\rho] + J[\rho] + E^{XC}[\rho], \tag{2.6.6}$$

where $J[\rho]$ is the classical Coulomb interaction between electrons (or Hartree energy) and $E^{XC}[\rho]$ is the energy exchange-correlation functional that can be expressed as:

$$E^{XC}[\rho] = (T[\rho] - T_S[\varphi_i^{KS}]) + (V_{ee}[\rho] - J[\rho]). \tag{2.6.7}$$

The exchange-correlation functional contains non-classical contribution to the kinetic energy (due to quantum nature of the electrons) and the interelectronic interaction terms that are unknown. As a result, the exchange-correlation functional has to be approximated, and there is a variety of methods available, each giving a different "flavour" of DFT used. It is important to note that DFT is only applicable to ground state systems because the variation principle is employed to determine the upper energy boundary for the ground state.

Finally,

$$\hat{h}^{KS}\varphi_i^{KS}(\mathbf{r}) = \varepsilon_i^{KS}\varphi_i^{KS}(\mathbf{r}), \tag{2.6.8}$$

where the KS one-electron orbitals are obtained using the self-consistent field (SCF) method [73], with

$$\hat{h}^{KS} = -\frac{1}{2}\nabla^2 - \sum_A^K + \int \frac{\rho(\mathbf{r}')}{|\mathbf{r}-\mathbf{r}'|}d\mathbf{r}' + v_{XC}(\mathbf{r}), \tag{2.6.9}$$

Here, the first term is the kinetic energy operator − the Laplacian, the second term describes the electron-nucleus attraction and the third the classical Coulombic repulsion between the electrons whereas the fourth contains all unknown non-classical interactions.

2.6.1 Exchange-Correlation Functional

Generally, an exchange-correlation functional in DFT is in the form of an integral of a function of the density and in some cases the density gradient. They can be classified according to the properties they depend on. The Local Density Approximation (LDA) functionals are dependent only on a local density at a specific point in space. The Generalized Gradient Approximation (GGA) functionals additionally incorporate the local density gradient, which accounts for any encountered non-uniformities. Meta-GGA functionals include the local density's second derivative. Intuitively, one might think that meta-GGA functionals show the best results, however, this is not always true [74]. Another class is hybrid functionals that include a combination of exact Hartree-Fock exchange [75], and a selection of this class were used in the calculations presented in this thesis.

2.6.2 Basis Set

In DFT, the one-electron molecular orbitals (MO) that generate the many-electron wavefunction are described by a basis set. Each basis set describes the radial and angular parts of the electron density by some mathematical functions. High-level basis sets contain multiple mathematical functions describing an atomic orbital. In some cases, *e.g.* for long-range interactions, basis set can be augmented with polarisation and/or diffuse functions. Additionally, for systems with heavy nuclei, the core electrons can be replaced by an effective core potential (ECP) that "simulates" the effect of core electrons and additionally introduces relativistic effects. The choice of a basis set is governed by the desired accuracy whilst taking into account the time (cost) needed for such calculation. The more complete the basis set (more mathematical functions used to describe an atomic orbital), the more time the calculation will consume.

In this thesis, the def2TZVP [76, 77] basis set was used as a compromise between accuracy and cost. Each results chapter contains more information on the computational methodology used in it.

Part A. Individual Ligands on Transition Metal Clusters

Chapter 3

Free Electron Laser Infrared Action Spectroscopy of Nitrous Oxide Binding to Platinum Clusters, $Pt_n(N_2O)^+$ ($n = 1-8$)

Abstract

IR-MPD spectroscopy has been applied to study the $Pt_n(N_2O)^+$ ($n = 1-8$) clusters which represent the entrance-channel complexes on the reactive potential energy surface for nitrous oxide decomposition on platinum clusters. Comparison of spectra recorded in the spectral regions 950-1600 cm^{-1} and 2000-2400 cm^{-1} with those simulated for energetically low-lying structures calculated using DFT show a clear preference for molecular binding *via* the terminal N atom, though some evidence of O-binding is observed for some cluster sizes. Enhanced reactivity of the Pt_n^+ $n \geqslant 6$ clusters towards N_2O is reflected in the calculated reactive potential energy surfaces and, uniquely in the size range studied, $Pt_6(N_2O)^+$ proved impossible to form in significant number density to study even with cryogenic cooling of the cluster source. Infrared-driven N_2O decomposition, resulting in the formation of cluster oxides, Pt_nO^+, is observed following vibrational excitation of several $Pt_n(N_2O)^+$ complexes.

The experiments were performed by the Mackenzie group in collaboration with André Fielicke at the Fritz Haber Institute, Berlin, using the free electron laser [67, 68]. I then carried out the analysis of results as well as the computational

work. The main findings in this work have been published by Meizyte *et al.* [60], and some figures as well as parts of the text are reproduced with permission from the PCCP Owner Societies.

3.1 Introduction

Nitrous oxide is a significant atmospheric pollutant both as a greenhouse gas (GHG) and for the role it plays in ozone depletion [78]. As a result of its relatively high global warming potential coefficient, N_2O is considered to be the third principal long-lived GHG after CO_2 and CH_4 [79] and one of the most potent waste gases resulting from human activity that has a significant impact on both future ozone layer and climate [80]. N_2O discharge is not covered by the Montreal Protocol [81] but, given its harmful environmental impact, there is considerable interest in using heterogeneous catalysis to reduce anthropogenic emissions [82].

The platinum group metals (Ru, Rh, Pd, Os, Ir, and Pt) are well-known heterogeneous catalysts. Platinum metal itself shows versatile catalytic abilities and is frequently used in industrial as well as everyday applications. For example, the production of nitric acid for fertilizers involves ammonia oxidation using a platinum catalyst [83]. However, platinum is probably best known for its role, along with palladium and rhodium, in promoting exhaust gas reactions in the three-way automobile catalytic converters (design first developed by Stempel *et al.* [84]). Highly inert (noble even) in its bulk form, most catalytic applications of platinum make use of it in highly divided, often nanoscale form. In addition to maximizing surface area, this introduces defects which are not present in extended single crystal surfaces and it is often these defect sites which provide the sites for interesting chemistry due to unsaturated coordination [85, 86].

Transition metal clusters can serve as tractable model systems for the study of heterogeneous nanocatalysts at the molecular level [87]. In the gas phase, the fundamental interactions involved in the reactive chemistry can be studied in the absence of complex interactions present in real catalysts, such as the influence of

substrates, solvation, and aggregation effects which are challenging to analyse and often obscure the fundamental interactions of interest [11]. The subject of this study, isolated $Pt_n(N_2O)^+$ clusters, represent model entrance-channel complexes for the initial chemisorption step in the metal-catalysed decomposition of N_2O.

Reflecting the catalytic properties of platinum, the reactions of platinum clusters, $Pt_n^{+/0/-}$, have received considerable attention previously. A variety of experimental techniques, including flow reactor, beam-gas cell studies, and Fourier-transform ion-cyclotron resonance (FT-ICR) mass spectrometry, have been employed to study the reactions of $Pt_n^{+/0/-}$ with small molecules. These include dehydrogenation of small hydrocarbons [88–94] as well as H_2, CO_2, N_2O *etc.* [95–99]. Pt_4^+ exhibits particularly low reactivity, also supported by a theoretical investigation [100], and a photofragmentation study of bare Pt_n^+ clusters by Ferrari *et al.* [101] suggests the reason lies in the anomalously large HOMO-LUMO gap for tetrahedral Pt_4^+. Interestingly, Pt_4^- activates carbon dioxide and dehydrogenates methane very efficiently, perhaps because of its own planar structure [94, 102].

Of particular relevance here are the single collision studies of $Pt_n^{+/-}$ reactions with N_2O in which the cationic clusters, in particular, exhibit dramatic size-dependent rate constants changing by several orders of magnitude upon the addition of a single metal atom [98]. In this small cluster regime, famously, every atom counts. In all cases the reaction proceeds exclusively *via* an O atom transfer generating sequential cluster oxides, $Pt_nO_m^+$. Additional collisions are required to stabilize the molecular adsorption of N_2O.

Several studies have established the catalytic abilities and even full catalytic cycles using platinum clusters. Water formation was observed in the catalytic oxidation of H_2 on Pt_n for $n = 7-30$ by Andersson and Rosén [95]; Shi and Ervin [103] found small Pt_n^- ($n = 3-6$) cluster anions to be effective catalysts for CO oxidation under thermal conditions. A full catalytic cycle of CO oxidation/N_2O reduction for Pt_n^+ ($n = 6-8$) was reported by Beyer, Bondybey, and coworkers [17].

N_2O represents an interesting adsorbate for infrared studies, with the possibility of both N- or O-binding reflected in the degree of activation. This is very clearly observed in infrared action spectroscopy of N_2O binding at single metal centers, for example, $Me(N_2O)_n^+$ (Me = Cu, Ag, Au [104] and Co, Rh, Ir [105] and Li, Al [106]) by Cunningham *et al.* [107]. These studies have revealed interesting binding motifs and structural isomers as well as the important role played by low-lying electronically excited states.

The Mackenzie group has previously studied N_2O adsorption on small gas-phase Rh_n^+ clusters ($Rh_n(N_2O)^+$, $n = 4-8$) [108, 109] in detail using the same methods as those employed in this work. Interesting IR-induced reactivity was observed in which excitation of infrared active modes results in N_2O decomposition and cluster oxide formation. Rh_5^+ proved special in this regard with a single coadsorbed oxygen atom changing the chemistry observed from N_2O loss on $Rh_5(N_2O)^+$ to $Rh_5O_2^+$ formation from $Rh_5(ON_2O)^+$ [110]. These results, along with those from related blackbody infrared [111] and collisional excitation studies [112], were explained in terms of relative reaction barriers and dissociation thresholds, demonstrating how spectral characterization of entrance-channel complexes yields important information on the full reactive potential energy surface.

3.2 Experimental and Computational Methods

The experimental setup has been described in detail previously in publications [113–115] and Section 2.4. Briefly, a rotating natural Pt target is ablated by a Nd:YAG laser (532 nm, 10 Hz). Ablated atoms cool and cluster by colliding with helium within a reaction channel to which nitrous oxide is added by an additional late-mixing pulsed valve downstream of the ablation point. The resulting gas mix, now entrained with a range of pure and decorated clusters, expands into the vacuum forming a molecular beam which is then skimmed before entering the extraction region of a reflectron time-of-flight mass spectrometer used to detect the presence of cationic species. In an attempt to suppress direct oxidation and

maximize the generation of molecularly bound $Pt_n(N_2O)^+$ clusters, the cluster source was cooled with liquid nitrogen to -140 °C.

To record IR-MPD spectra, the cluster beam is subjected to alternate pulses of output of the FHI FEL [67, 68], operating for these purposes in the 950-1600 cm^{-1} and 2000-2400 cm^{-1} ranges, and corresponding parent ion depletion and fragment(s) channel enhancement are recorded as a function of wavenumber. In this way the spectra yield information on the infrared active modes of the parent cluster as well as dissociation branching ratios which can be compared with the results of DFT simulations.

Energetically low-lying structures and relevant transition states connecting them have been calculated at the def2TZVP [76, 77]/TPSSh [116, 117] level using Gaussian 16 software package [118]. This basis set/functional pair reproduces the transition metal-ligand bond dissociation energies [119] and showed similar energetic ordering of the $Pt_nO_2CO^+$ cluster geometries [120] to using the TPSS [117] functional with the def2TZVP basis set [76, 77] that previously was proved to generate reliable IR-MPD experimental results [121, 122]. To account for weak intramolecular interactions, the GD3-BJ dispersion term [123] was introduced, in addition to scalar relativistic corrections for the Pt atoms in the form of a quasirelativistic Wood-Boring effective core potential (WB-ECP) [124] freezing 60 inner electrons. As starting structures, the coordinates of bare Pt_n^+ clusters for n = 3−5 were taken from earlier work by Harding *et al.* [122]. To provide a better match with experimental data, computed harmonic vibrational frequencies were scaled by a factor of 0.955, determined by calculating the vibrational frequency of the N=N stretch in the "free" N_2O [125]. All energies reported here include zero-point corrections and are given relative to the lowest energy molecularly adsorbed structure. Potential energy profiles were generated by identifying plausible transition states between two minima and performing Intrinsic Reaction Coordinate (IRC) [126, 127] calculation in order to verify the path.

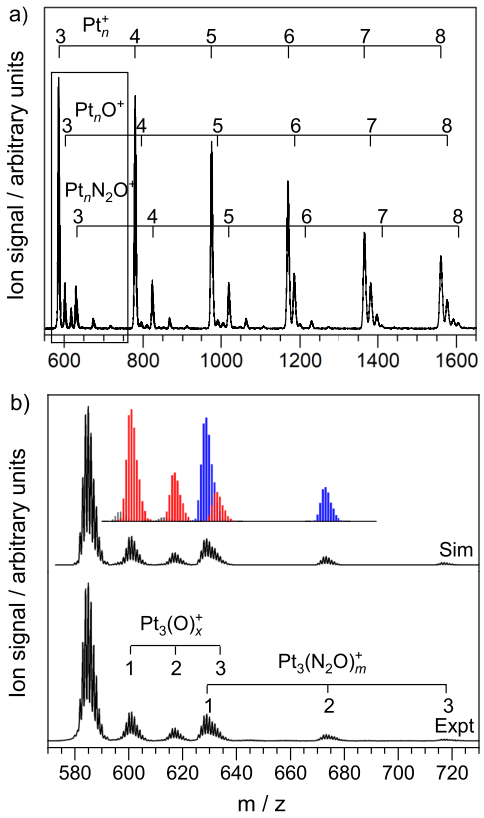

Figure 3.3.1: a) Time-of-flight mass spectrum; b) experimental and simulated time-of-flight mass spectrum of the Pt_3^+ clusters – both produced by laser ablation of a natural platinum rod in He to which N_2O is added downstream. The cluster source was cooled to -140 °C with liquid N_2. The principal species produced are simple cluster oxides, $Pt_3O_x^+$, and $Pt_3(N_2O)_m^+$ with traces of Pt_3C^+ and Pt_3CO^+. Adapted from Ref. [60] (https://doi.org/10.1039/D0CP02800B) with permission from the PCCP Owner Societies.

3.3 Time-of-Flight Spectrum and Analysis

Figure 3.3.1.a) displays the time-of-flight mass spectrum produced upon ablating a natural platinum rod in presence of He and N_2O introduced downstream *via* the late-mixing valve. The progressions of $Pt_nO_x^+$ and $Pt_nN_2O^+$ clusters dominate the mass spectrum. An IR-MPD study concerning the platinum oxide clusters has been published by the combined Mackenzie-Fielicke groups [128].

There are significant challenges when interpreting the time-of-flight spectrum due to natural platinum having six stable isotopes, which leads to the signal overlaps between different species. Figure 3.3.1.b) demonstrates an example of the

deconvolution of Pt_3X^+ (X = adsorbate) peaks that was performed for all species concerned. This was done by fitting various proportions of the isotopic patterns of relevant species (Figure 3.3.2.a)) to the experimental mass spectrum until the best match was found. Traces of Pt_3C^+ and Pt_3CO^+ are also observed − they are assumed to come from trace contaminants arising from polishing the target rod.

The ratio of the areas of each peak in Figure 3.3.1.a) reflect reactivity pathways of the encounter complex, $[Pt_nN_2O^+]^*$, which can be summarised as:

(1) (direct dissociation) $[Pt_nN_2O^+]^* \rightarrow Pt_n^+ + N_2O$,

(2) (oxidation) $[Pt_nN_2O^+]^* \rightarrow Pt_nO^+ + N_2$,

(3) (N_2O adsorption) $[Pt_nN_2O^+]^* + M \rightarrow Pt_n(N_2O)^+ + M^*$, M = third body.

With respect to a primary reaction, first of all, an encounter complex forms which, in the absence of additional collisions or radiative cooling, must either dissociate (1) or react (2). Without DFT calculations this experiment is "blind" to process (1), but evidence for process (2) is observed in the mass spectrum in the form of platinum oxide. Multiple collision conditions allow for a stabilisation of the initial encounter complex resulting in N_2O adsorption products in the mass spectrum. Secondary reactions with same outcomes as mentioned processes can proceed as well.

Figure 3.3.2.a) shows the calculated normalised signal abundances to a unity within each n (Pt_n^+ not shown) from the areas of the peaks in Figure 3.3.1. For $n = 3$, the branching ratios for processes (2) and (3) are similar. For $n = 4$ and 5 however, minimal Pt_nO^+ formation is observed, with $Pt_n(N_2O)^+$ being the dominant product. For $n \geqslant 6$, the situation changes and the production of Pt_nO^+ dominates, with virtually none of the $Pt_6N_2O^+$ clusters observed.

In order to better see the differences in reactivity, the Pt_nO^+ signal as a fraction of total primary reaction products, $[Pt_nO^+]/([Pt_nO^+] + [Pt_nN_2O^+])$, is plotted in Figure 3.3.2.b). The differences in reactivity between small and large Pt_n^+ clusters are highlighted. Balteanu *et al.* [98], in a single collision study, only observed process (2) products, due to the lack of stabilising collisions required

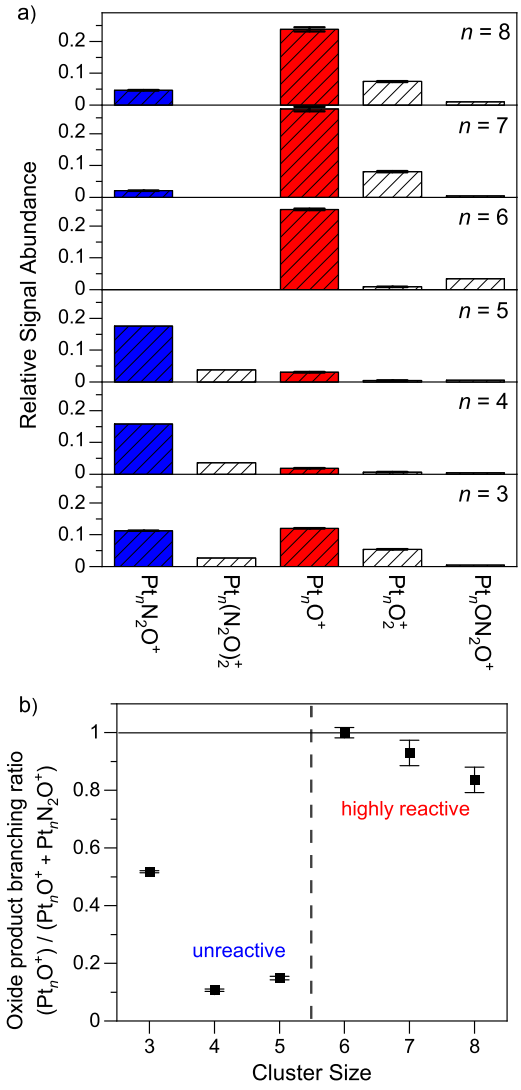

Figure 3.3.2: a) Histogram with normalised ion abundances (to a unity within each n; Pt_n^+ not shown) for reaction products generated in the cluster source by the reaction of Pt_n^+ ($n = 3–8$) with N_2O. The uncertainties shown reflect the fitting of overlapping isotope patterns for different species (see inset Figure 3.3.1.b)); b) fractional oxide production as a measure of $Pt_n^+ + N_2O$ reactivity. A step change in reactivity occurs between $n = 5$ and 6. Adapted from Ref. [60] (https://doi.org/10.1039/D0CP02800B) with permission from the PCCP Owner Societies.

for process (3). Interestingly, an increase in reactivity, similarly to this study, was observed between $n = 5$ and 6.

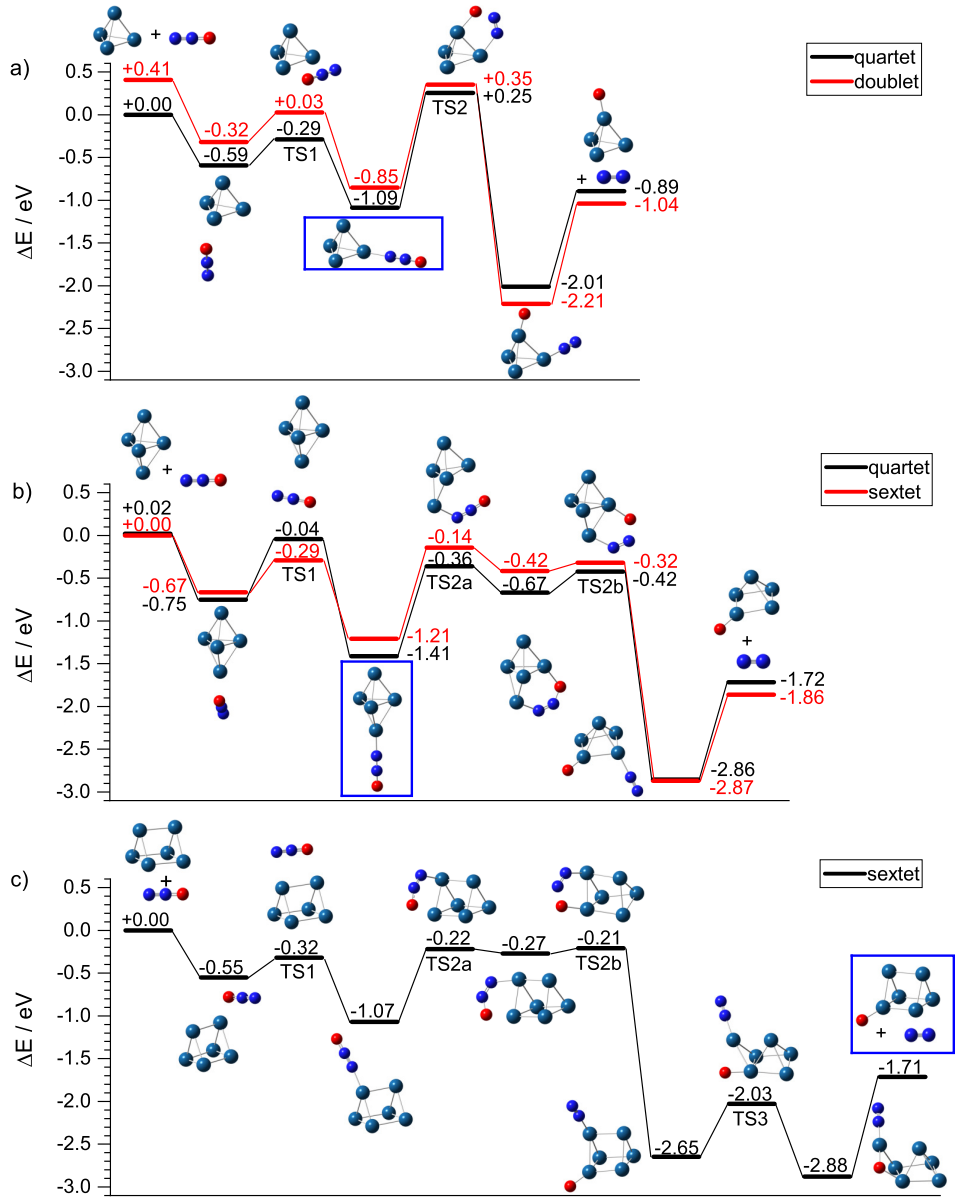

Figure 3.4.1: Intrinsic reaction coordinate for a) Pt_4^+, b) Pt_5^+, and c) $Pt_6^+ + N_2O$ entrance channels. Blue boxes highlight the predominant species observed in the mass spectrum for each n identified spectroscopically. The barrier to N_2O dissociation on the Pt_n^+ cluster is pronounced for $n = 4$ and submerged for $n = 6$. This is reflected in the observed reactivity (Figure 3.3.2): Pt_4^+ is the least reactive favouring N_2O adsorption whereas Pt_6^+ does not form any adsorption products and mainly produces oxides. Only the lowest electronic states are shown. For $n = 4$, geometries of both doublet and quartet are virtually indistinguishable; for $n = 5$, they are not − higher in energy sextet structures are given in the Appendix A. Adapted from Ref. [60] (https://doi.org/10.1039/D0CP02800B) with permission from the PCCP Owner Societies.

3.4 Potential Energy Landscapes

The reactivity can be understood in terms of reaction barrier heights on the potential energy surface plot. Figure 3.4.1 shows the intrinsic reaction coordinate for a) Pt_4^+, b) Pt_5^+, and c) $Pt_6^+ + N_2O$ reaction channels. Only the lowest energy electronic states are shown. The blue boxes show the predominant species formed in the mass spectra (full analysis in Sections 3.5 and 3.6). In each case, the two minima towards the left hand side represent the O- and N-bound entrance-channel complexes of the respective $Pt_n(N_2O)^+$ species (process (4)) and TS1 − a transition state for the N_2O rotation connecting the two minima. The N-bound N_2O entrance channel is separated from the product channel by a potential barrier TS2 which involves a significant N_2O rearrangement, ultimately leading to the production of the Pt_nO^+ cluster and N_2 (process (3)). In all cases, the overall reaction is calculated to be exothermic by more than 1 eV.

Balteanu *et al.* [98] reported the difference in reactivity between the Pt_4^+ and Pt_6^+ clusters as more than a factor of three orders of magnitude. By looking at Figure 3.4.1, this can be attributed to the fact that whilst Pt_4^+ has a considerable TS2 barrier (1.34 eV for the quartet spin state), this barrier is submerged for the Pt_6^+ species (0.85 eV). The TS2 barrier for the Pt_5^+ clusters is 1.05 eV for the quartet multiplicity, however, Balteanu *et al.* [98] reports an intermediate activity (a factor *ca.* 44 less than for Pt_6^+).

3.5 IR-MPD Spectra

The IR-MPD spectra of the $Pt_n(N_2O)^+$ ($n = 1-8$) clusters are given in Figure 3.5.1. N=O and N=N stretch regions are covered, and the respective vibrations at 1285.0 cm^{-1} and 2223.5 cm^{-1} in "free" N_2O molecule [125] are indicated by dashed lines. As discussed previously, negligible $Pt_6(N_2O)^+$ is produced and thus no spectrum can be recorded of this species.

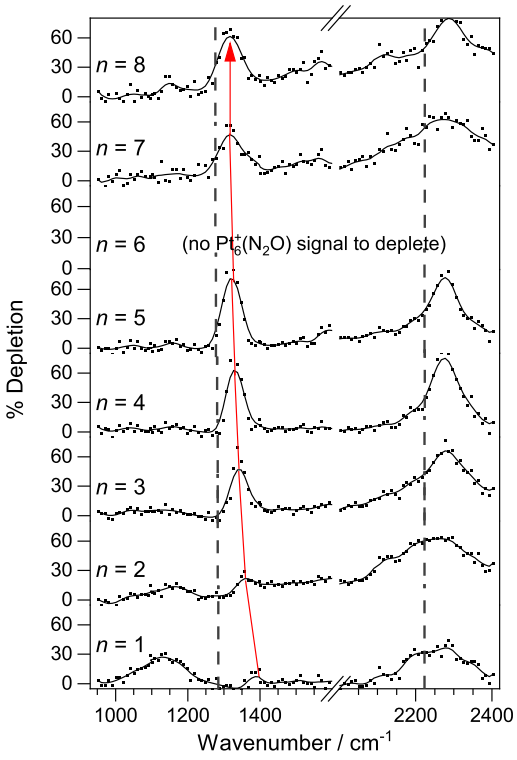

Figure 3.5.1: IR-MPD spectra of the $Pt_n(N_2O)^+$ ($n = 1-8$) clusters recorded in depletion of the parent cluster ion. The dashed lines at 1285.0 cm^{-1} and 2223.5 cm^{-1} indicate the wavenumbers of the N=O and N=N stretches of "free" N_2O, respectively [125]. Adapted from Ref. [60] (https://doi.org/10.1039/D0CP02800B) with permission from the PCCP Owner Societies.

For $n \geqslant 3$, the spectra exhibit clear features slightly blue-shifted from the "free" N_2O band positions. The presence of both of these bands is an indication of molecularly-bound N_2O on the metal clusters. The blue shift of both bands indicates preferential N_2O binding *via* the N atom on the $n \geqslant 3$ clusters (supported by computational results in Section 3.6) and reflects the dominance of σ donation from the N_2O to the cationic Pt_n^+ clusters over π back-bonding.

For the smallest species, $n = 1-2$, the observed vibrational bands are considerably broader and there is evidence of components both blue- and red-shifted with respect to the "free" N_2O stretches. Red-shifted bands, around the N=O stretch (Figure 3.6.1), are indicative for the presence of O-bound clusters. They are red-shifted by 100 cm^{-1}, compared with the corresponding "free" N_2O band, indicating

molecular activation. Small clusters have fewer degrees of freedom and are less efficient in annealing to the lowest energy (N-bound) structures, allowing trapping of energetically higher-lying isomers (O-bound geometries). Interestingly, the spectrum of the $Pt_8(N_2O)^+$ clusters exhibit both blue- and red-shifted bands in both spectral regions, possibly reflecting a mixture of N- and O-bound structures, as is the case for $n = 1$ and 2. Similar higher resolution infrared studies of $M(N_2O)_n^+$ (M = Co, Rh, Ir, Cu, Ag, Au, Li, and Al) [104–107] also observed clear signatures of N- and O-bound geometries albeit both bands were blue-shifted from the "free" N_2O band positions.

There is a general red shift of the N-bound signature band in the N=O stretching region from $n = 1$ to 8 (marked by a red arrow in Figure 3.5.1). It can be explained in terms of charge dilution for the larger complexes. The broader nature of the corresponding bands in the N=N stretching region obscure any such trend. Interestingly, a similar broadness of the bands in the N=O versus N=N regions was observed in the IR-MPD spectra of the $Au_n(N_2O)^+$ and $Co_n(N_2O)^+$ clusters [61, 107]. It was argued that it could be a consequence of increased FEL power in the N=N stretching region leading to lifetime broadening (Section 1.3.3) and the need for fewer higher energy photons in the N=N (higher wavenumber) than N=O (lower wavenumber) stretching region for dissociation to take place, which are relevant here as well.

3.6 N_2O Binding Motifs in Calculations

The comparison between experimental and computational spectra for low-lying isomers of a) $Pt_3(N_2O)^+$ and b) $Pt_4(N_2O)^+$ is given in Figure 3.6.1. The lowest energy structures show the N_2O molecule dissociatively adsorbed, but given the low binding energy of N_2 and the overall exothermicity of the dissociation, it is unlikely that in such cases the N_2 would remain bound. Moreover, the IR-MPD spectra show evidence for molecularly-bound structures, and these are selected as the zero-point energy references, as indicated.

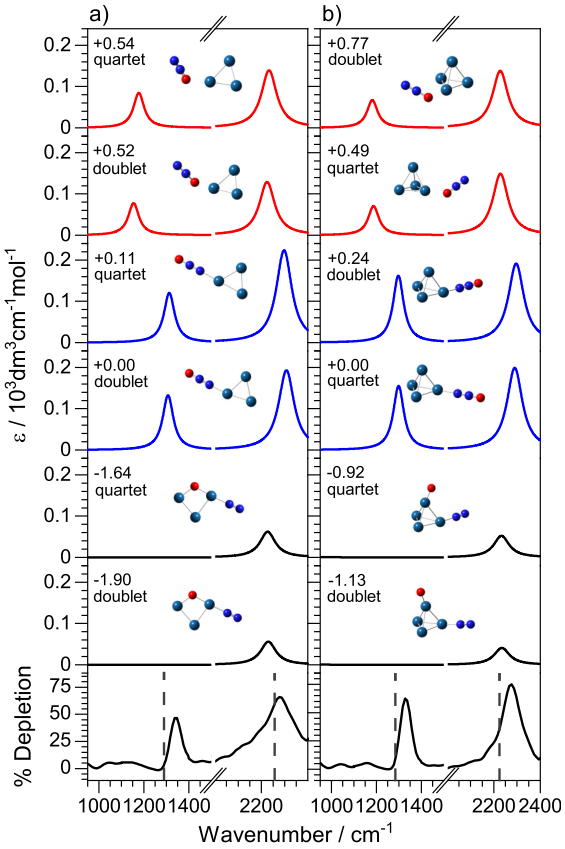

Figure 3.6.1: Comparison of experimental and simulated IR-MPD spectra for a range of low-lying isomers of the a) $Pt_3(N_2O)^+$ and b) $Pt_4(N_2O)^+$ complexes. All molecularly-bound isomers within 1 eV of the lowest energy structure are presented. Blue spectra represent N-bound isomers and red spectra O-bound variants. The dashed lines at 1285.0 cm^{-1} and 2223.5 cm^{-1} represent the fundamental bands in "free" N_2O [125]. Adapted from Ref. [60] (https://doi.org/10.1039/D0CP02800B) with permission from the PCCP Owner Societies.

In both a) and b), low-lying doublet and quartet electronic states are found, but due to similar positions of the bands, the experiment is inconclusive to the electronic state of the clusters. The N-bound isomers lie lower in energy than the corresponding O-bound isomers by *ca.* 0.5 eV, reflecting the assignment of the bands in Figure 3.5.1. In all given structures, the N_2O is bound at a single atom rather than a bridging site, and a good match between the experimental and computational spectra are provided. The nature of the isomers and their energetic ordering are qualitatively similar for the $Pt_5(N_2O)^+$ species and are not shown in Figure 3.6.1.

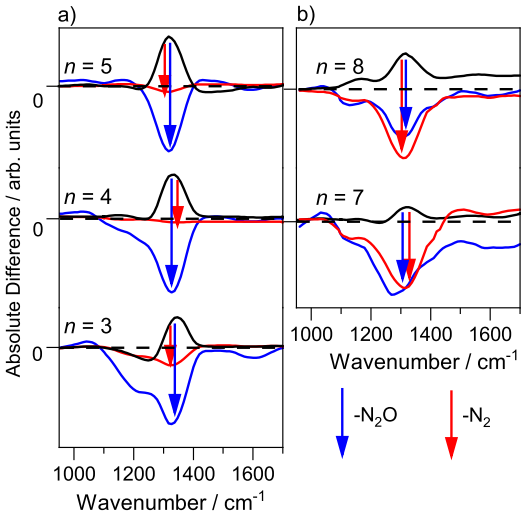

Figure 3.7.1: IR-MPD spectra of the $Pt_n(N_2O)^+$ clusters in the N_2O (N=O) stretch region (black line). Red and blue spectra show the simultaneous enhancements observed in the Pt_nO^+ and Pt_n^+ mass channels representing IR-driven reactive (N_2 loss) and desorptive (N_2O loss) processes. Adapted from Ref. [60] (https://doi.org/10.1039/D0CP02800B) with permission from the PCCP Owner Societies.

3.7 IR-Induced Reactivity

In any infrared action spectrum, the depletion of a parent ion signal must be matched by an enhancement in the signal for some daughter species. By tracking the parent ion depletions and absolute signal enhancements in different daughter channels simultaneously, it is possible to determine the branching ratios for the two most likely possibilities:

(4) (N_2O loss) $Pt_nN_2O^+ + h\nu \rightarrow Pt_n^+ + N_2O$,

(5) (IR-driven dissociation) $Pt_nN_2O^+ + h\nu \rightarrow Pt_nO^+ + N_2$.

Figure 3.7.1 shows such analysis for the $Pt_n(N_2O)^+$ (n = 3–5, 7, 8) clusters in the N=O stretching region (corresponding behaviour is observed in the N=N stretching region as well). In each case, the spectra in blue show the enhancement of Pt_n^+ (reflecting process (4)) and in red the Pt_nO^+ clusters (process (5)).

In terms of reactivity, the behaviour of small clusters (n = 3–5) is different to the large ones (n = 7, 8). For n = 3–5, the excitation of the N=O stretch leads to the almost exclusive N_2O loss (process (4)), consistent with these clusters reaching

the dissociation threshold before the transition state of the N_2O decomposition. For $n = 7$, 8, N_2O loss (process (4)) as well as N_2 desorption (process (5)) are observed suggesting that the reactive transition state lies below or at a comparable energy to the dissociation threshold. All in all, the infrared-induced reactivity is similar to the reactivity seen in the time-of-flight spectra in Figure 3.3.2.

Efficient generation of the Pt_nO^+ daughter species have been seen in several studies of other systems by the Mackenzie group, including $Rh_n(N_2O)^+$ [108, 109], $Rh_nO(N_2O)^+$ [108, 110], $Pt_nO_2(CO)^+$ [120], and $Au_n(OCS)^+$ [59]. Also, these studies [108, 112] demonstrated that the products observed following infrared excitation mirror those of collisional activation, implying that the entrance-channel complexes are "heated" until the dissociation/reactive channels open. Previous studies have not revealed any mode selective character to the chemistry induced as the vibrational modes involved are not completely localised, and the current system is no exception. However, the ability to selectively increase the internal energy (IE) of known clusters with spectral knowledge of their structure represents a unique feature in the exploration of these catalytically-relevant reactive potential energy surfaces.

3.8 Summary and Conclusions

A combined experimental IR-MPD and computational study of N_2O reacting with and binding to Pt_n^+ $(n = 3-8)$ has revealed key features on the potential energy surface of the $Pt_n^+ + N_2O \rightarrow Pt_nO^+ + N_2$ reaction. The laser ablation/molecular beam conditions employed in this study are shown, in most cases, to lead to the efficient formation of the entrance-channel complexes on the reactive surface, the structures of which can be probed by multiple photon dissociation action spectroscopy. One notable exception are the Pt_6^+ clusters which react completely to generate the oxides with no evidence of the $Pt_6(N_2O)^+$ species observed.

The observed reactivity can be well-understood in terms of potential energy surfaces calculated at the DFT level. Furthermore, the simulated vibrational spectra for the calculated energetically low-lying entrance-channel complexes match

well with the action spectra recorded. For several cluster sizes there is clear evidence for infrared-driven cluster chemistry observed in the loss of N_2 following infrared excitation of the N=O stretching mode of the parent $Pt_n(N_2O)^+$. These results are in good agreement with calculated reactive barrier heights compared to the N_2O binding energies.

It would be beneficial to extend the DFT calculations to include the $Pt_7(N_2O)^+$ and, especially, $Pt_8(N_2O)^+$ clusters, for which in their spectrum there is a red-shifted band, possibly due to the O-bound N_2O isomers. Potential energy surfaces have not been mapped out for the reaction coordinate of $Pt^+_{7,8}$ + N_2O, and would confirm whether the reactive barrier is submerged as in the case of Pt^+_6 + N_2O.

Chapter 4

Infrared Study of Nitrous Oxide Adsorption on Gas-Phase Gold and Cobalt Clusters, $Au_n(N_2O)^+$ ($n \leqslant 7$) and $Co_n(N_2O)^+$ ($n \leqslant 5$)

This chapter presents a similar type of study to that of N_2O on Pt_n^+ described in Chapter 3 but using Au_n^+ and Co_n^+ clusters. The experiments were performed by the Mackenzie group in collaboration with André Fielicke in the Fritz Haber Institute in Berlin using the free electron laser [67, 68]. Most of the spectroscopy of $Au_nN_2O^+$ and $Co_nN_2O^+$ species is presented in Cunningham's DPhil thesis [107], however, further work that was accomplished is described in this chapter. In Cunningham's thesis, most important results include the IR-MPD spectra of $Au_n(N_2O)^+$ species, where for $n = 1-5$, one band in each of the vibrational stretch regions of N=O and N=N was observed along with a shoulder in the N=N stretch region that according to DFT calculations might indicate the existence of molecular O-bound N_2O. The signature band of molecular O-bound N_2O in the N=O stretch region was found to lie in the lower wavenumber region than what had been scanned and in order to confirm its existence the IR-MPD spectra in that region needed to be recorded. For $n = 6$ and 7, no such shoulder was found, and the spectra were assigned to the molecular and terminal N-bound N_2O .

This chapter contains additional work I have undertaken, principally to better

understand the reactivity taking place in the cluster channel. In more detail, I performed the reactivity analysis of both $Au_n(N_2O)^+$ and $Co_n(N_2O)^+$ (n = 1−5) clusters from their time-of-flight spectrum. I have also undertaken follow-up experiments of the $Au_n(N_2O)^+$ clusters in the spectral region of 1000-1200 cm^{-1} that was not scanned during the original beamtime. The published study [61] includes these further experiments and analyses described in this chapter.

In this chapter, the reactivity of Au_n^+ as well as Co_n^+ clusters with N_2O is analysed from the resulting mass spectra observed and compared to Pt_n^+. Regarding $Au_nN_2O^+$, the fingerprint region for molecular O-bound N_2O N=O vibration is explored by means of IR-MPD spectroscopy and it is confirmed that there is no evidence of such species produced in the experiment.

4.1 Introduction

A reactivity study for Au_{1-4}^+ with N_2O was performed by Dietrich *et al.* [129] using a Penning trap mass spectrometer. They found the major reaction channel: $Au_{1,2}^+ + N_2O \rightarrow Au_{1,2}N + NO^+$. Additional reaction products were also observed indicating a preferred breaking of the N=O bond for $Au_{1,3}^+$ and the N=N bond for Au_2^+.

Regarding the structures of bare Au_n^+ clusters ($n \leqslant 9$), FIR spectroscopy complemented with DFT simulations has been employed by Ferrari *et al.* [130] using Ar tagging. A planar geometry was found for the $Au_7Ar_m^+$ species and three-dimensional for the $Au_9Ar_m^+$ complex (larger clusters form 3D structures for stability). Interestingly, the $Au_8Ar_m^+$ clusters showed a coexistence of both 2D and 3D structures at 200 K. Ion mobility study at room temperature coupled with DFT theoretical considerations was performed for the Au_n^+ clusters ($n < 14$) by Gilb *et al.* [131] and indicated the onset of 3D isomers at $n = 8$. By contrast, this crossover point for the Au_n^- clusters occurs at $n = 12$ [34, 42, 132]. FIR-MPD spectroscopy combined with DFT as well as *ab initio* molecular dynamics (MD) [58, 133–135] calculations were performed for neutral gold clusters, and the onset of 3D structures was determined to be at $n = 11$.

There is extensive evidence that for other metals the crossover to planar structures occurs at smaller cluster sizes, *e.g.* $n = 5$ for Ag_n^+ [41, 136–138]. The relativistic effects associated with s/p orbital shrinkage and d/f orbital expansion that in turn induce $s - d$ hybridization and increase $d - d$ overlap were calculated to be strongest for the gold atom [139, 140] and are attributed as the cause for such unusually large planar gold structures in all mentioned studies.

The reactions of $Co_n^+ + N_2O$ ($n = 4{-}30$) were explored under single collision conditions using FT-ICR mass spectrometry by Anderson *et al.* [141] and tandem mass spectrometry by Hirabayashi *et al.* [142] for $n = 3{-}7$. The former study found that most clusters react generating the Co_nO^+ species and, in some cases, additionally undergo Co atom(s) loss. The latter study observed different reactivity between even- and odd-sized n clusters that resulted in the $Cu_n(N_2O)^+$ and $Cu_{n-1}O(N_2O)^+$ products, respectively.

The structures of $Co_nAr_m^+$ ($n = 4{-}8$) have been studied by FIR-MPD coupled with DFT simulations by Gehrke *et al.* [143], and the calculations showed that Ar tagging leads to altering of the bare Co_n^+ geometries. Furthermore, all compounds were calculated to be in a high spin state and exhibit significant Jahn-Teller distortions. Argon-tagged Co_n^+ and $Co_{n-1}Cr^+$ ($n = 3{-}5$) clusters were also investigated by IR-MPD spectroscopy by Jia *et al.* [144]. The $Co_nAr_m^+$ structural assignments are in good agreement with those of Gehrke *et al.* [143], excluding the $Co_5Ar_5^+$ species. The Cr dopant did not influence the structures by much but was found to play a role in magnetic coupling in a size-dependent fashion.

4.2 Experimental and Computational Methods

The experimental setup has been described in detail previously in publications [113–115] and Section 2.4. Briefly, a rotating Au or Co target is ablated by a Nd:YAG laser (532 nm, 10 Hz). Metal clusters form and thermalise by collisions with He atoms and nitrous oxide is added downstream *via* the late-mixing pulsed valve. The resulting gas mix, now entrained with a range of pure and decorated clusters, expands into

the vacuum forming a molecular beam which is then skimmed before entering the extraction region of a reflectron time-of-flight mass spectrometer used to detect the presence of cationic species. The experiment was run at room temperature.

The IR-MPD spectra of the clusters produced are recorded using the FHI FEL [67, 68] with counterpropagating alternating IR on/IR off pulses in the ranges of 1000-1400 cm^{-1} and 2100-2450 cm^{-1} covering the N_2O N=O and N=N stretch regions. Parent ion depletions and corresponding daughter enhancement(s) are tracked as a function of wavenumber, yielding infrared action spectra as well as any fragmentation branching ratios. The resulting IR spectra have been interpreted with the help of simulations based on low energy structures determined from DFT.

Energetically low-lying structures have been calculated at the def2TZVP [76, 77]/TPSSh [116, 117] level using Gaussian 09 software package [145]. This basis set/functional combination was selected having provided a good match with experimental data in previous studies [121, 122]. Scalar relativistic corrections for the Au atoms were introduced *via* the use of quasirelativistic WB-ECP [124] that freezes 60 inner electrons. To provide a better match with experimental data, computed harmonic vibrational frequencies were scaled by a factor of 0.955, determined by calculating the vibrational frequency of the N=N stretch in the "free" N_2O [125]. All energies reported here include zero-point corrections and are given relative to the lowest energy molecularly adsorbed structure.

4.3 Reactivity of Gold Clusters

The time-of-flight mass spectrum produced by laser ablation of a gold rod in presence of He carrier gas with N_2O gas added downstream is given in Figure 4.3.1.a) with b) showing an enlarged region of the reaction products of Au_3^+ with N_2O. By integrating under each peak in a), the signals corresponding to each species produced were calculated and the histogram given in c) constructed.

Overall, little reactivity is observed between the Au_n^+ clusters and N_2O adsorbate(s). For all n, the bare gold signal accounts for $> 60\%$ of all reaction products.

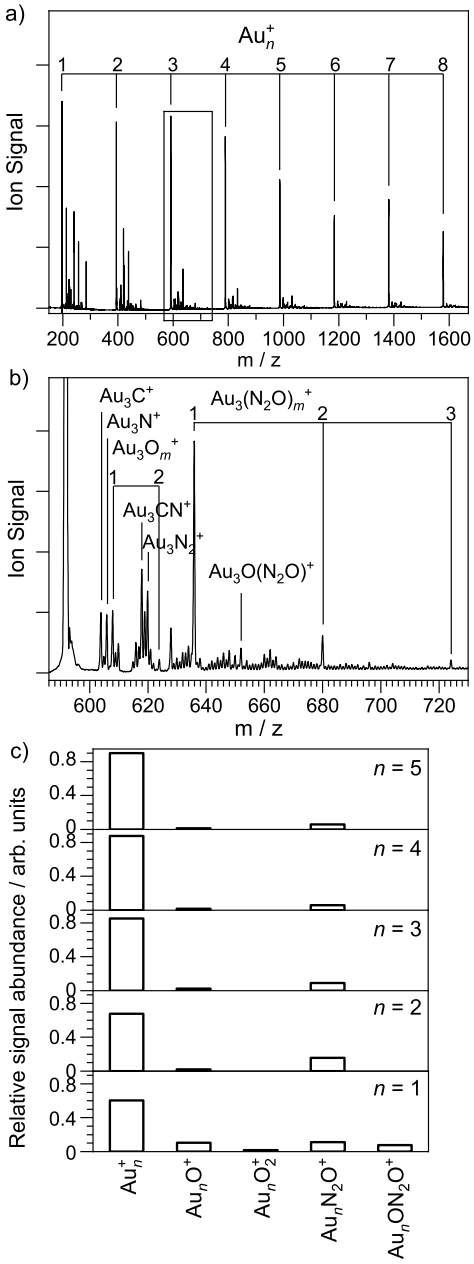

Figure 4.3.1: a) Time-of-flight mass spectrum of the Au_n^+ clusters produced by laser ablation of a gold rod in the presence of helium carrier gas (10 bar backing pressure) with N_2O added downstream *via* the late-mixing valve; b) shows an enlarged area of the Au_3^+ clusters and their reaction products; c) Histogram illustrating the relative abundances of each of the ion signals in the ToF mass spectrum: Au_n^+, Au_nO^+, $Au_nO_2^+$, $Au_nN_2O^+$, and $Au_nON_2O^+$. The sum of the signals within each n has been normalised to 1. The figure is adapted from Ref. [61] (https://doi.org/10.1039/D0CP05195K) with permission from the PCCP Owner Societies.

Judging by the intensity of the Au_n^+ signal, the Au^+ clusters appear to be the most reactive, with reactivity dropping as n increases. The second most intense signal is due to the complexation with N_2O resulting in the $Au_n(N_2O)^+$ species. A small amount of Au_nO^+ is also produced, presumably arising from the reaction with N_2O resulting in the release of N_2. Exclusively for $n = 1$, $Au_nO_2^+$ and $Au_nON_2O^+$ are produced. Traces of Au_3C^+ and Au_3CN^+ are also observed but are assumed to originate from polishing the target rod.

These results are different to those of the single collision reaction study done by Dietrich *et al.* [129], and can be explained in terms of experimental conditions. A single collision environment allows for a build-up of the internal energy of clusters promoting reactions taking place whereas multiple collision conditions (such as in the current study) − for thermalisation. However, in similar (approximately thermal multiple collision) experimental conditions as here, the Pt_n^+ clusters [60] proved to be much more reactive towards N_2O than the Au_n^+ clusters.

4.4 N_2O Binding Motifs in $Au_n(N_2O)^+$ Clusters

The IR-MPD spectra of $Au_n(N_2O)^+$ ($n = 3-7$) species is presented in Figure 4.4.1, and only a flat line around 0 on the y-axis is observed in the newly scanned spectral region of 1000-1200 cm^{-1}. $\sigma-$donation from the lone pairs on the O atom lead to weakening of the N=O bond whilst N-binding leaves N=O essentially unchanged from that in the "free" N_2O. This confirms the absence of O-bound N_2O isomers, as shown in the computed spectra of energetically low-lying calculated isomers in Figure 4.4.2 for the $n = 3-5$ clusters. A similar explanation is expected to be pertinent for the larger clusters ($n = 6$, 7) as well.

4.5 Reactivity of Cobalt Clusters

Following the same experimental method as in Section 4.3 for gold, the time-of-flight spectrum produced by laser ablation of a cobalt rod is given in Figure

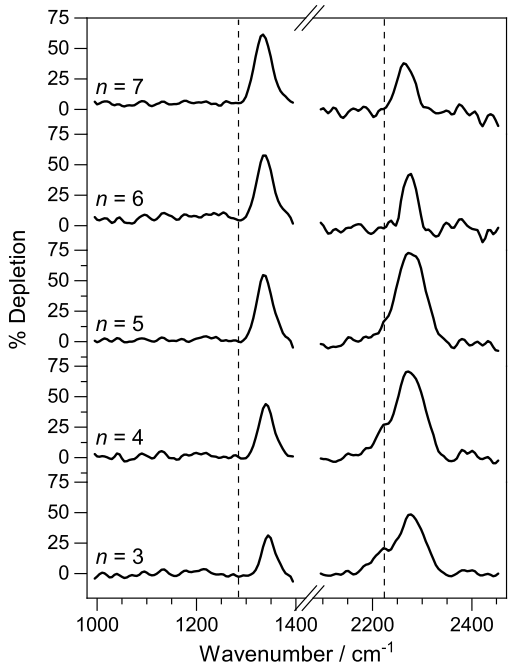

Figure 4.4.1: IR-MPD spectra of the $Au_n(N_2O)^+$ ($n = 3-7$) clusters given as percentage depletion of the parent ion signal. The vertical dashed lines at 1285.0 and 2223.5 cm^{-1} indicate the wavenumber of the N=O and N=N stretches in the "free" N_2O molecule, respectively [125]. The figure is adapted from Ref. [61] (https://doi.org/10.1039/D0CP05195K) with permission from the PCCP Owner Societies.

4.5.1.a) with b) showing an enlarged region of the reaction products of Co_3^+ with N_2O. A histogram visualising the reactivity pathways is given in c) by integrating the areas of the peaks in a).

The Co_n^+ clusters are more reactive towards N_2O than the gold counterpart due to cobalt atom having a less filled *d* shell. The smaller clusters, $n \leqslant 2$, predominantly form the N_2O adsorption products whereas the larger clusters, $n \geqslant 3$, react readily with N_2O forming simple oxides. There is closer resemblance to the reactivity of Pt_n^+ clusters with N_2O [60], where distinct differences between small (molecular N_2O adsorption) and large (oxide production) clusters were found.

The apparent production of cobalt oxides has been seen in single collision studies [141, 142], however, for some species, the loss of a cobalt atom was also observed. Given the lack of parent ion selectivity, the present study is blind to this reaction channel. As mentioned previously, due to the thermalisation of the

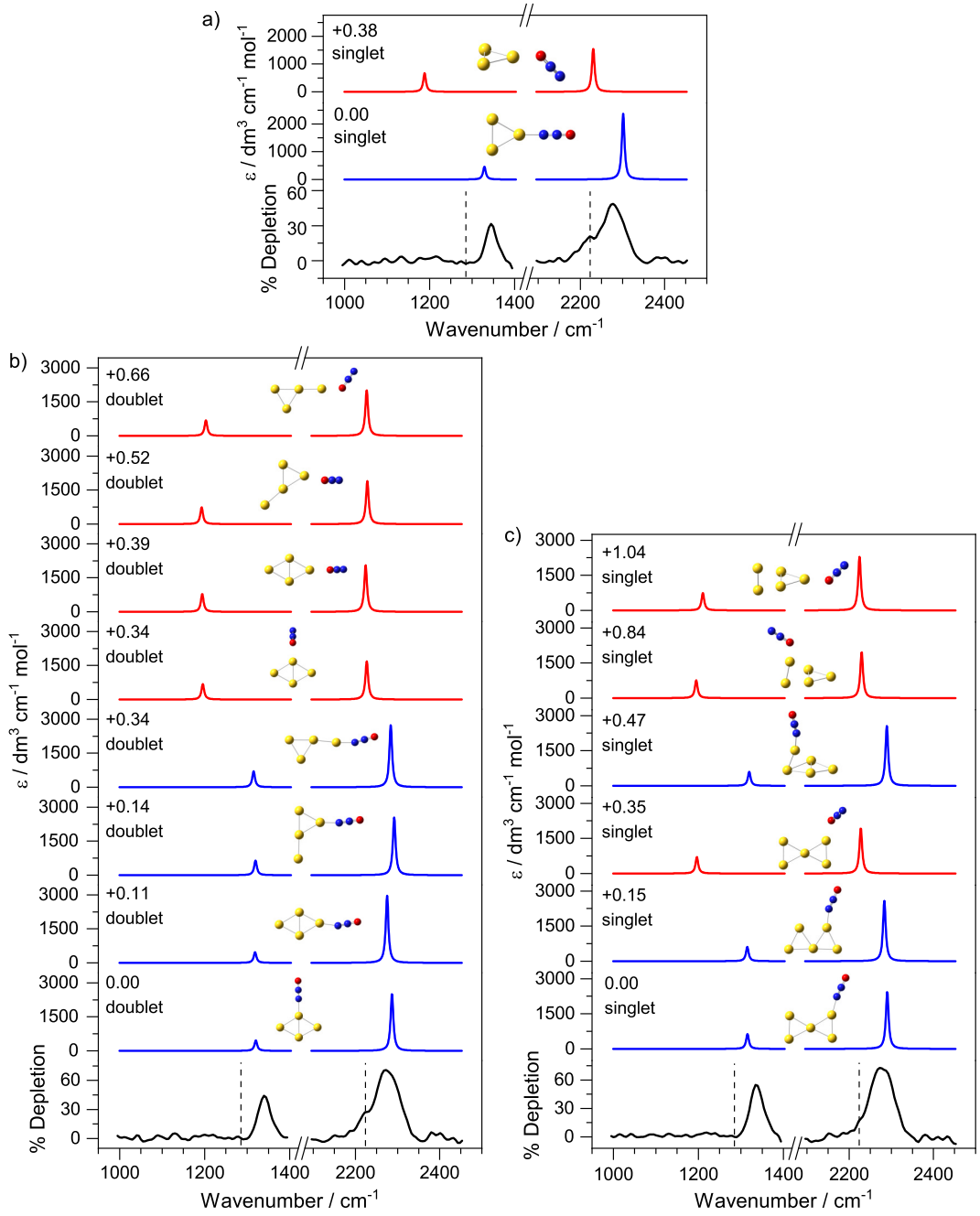

Figure 4.4.2: The comparison between experimental and computational spectra for energetically low-lying isomers of the a) $Au_3(N_2O)^+$, b) $Au_4(N_2O)^+$, and c) $Au_5(N_2O)^+$ clusters. Simulated bands due to N-bound and O-bound isomers are indicated in blue and red, respectively. The vertical dashed lines at 1285.0 and 2223.5 cm^{-1} mark the wavenumber of the N=O and N=N stretches in the "free" N_2O molecule, respectively [125]. The figure is adapted from Ref. [61] (https://doi.org/10.1039/D0CP05195K) with permission from the PCCP Owner Societies.

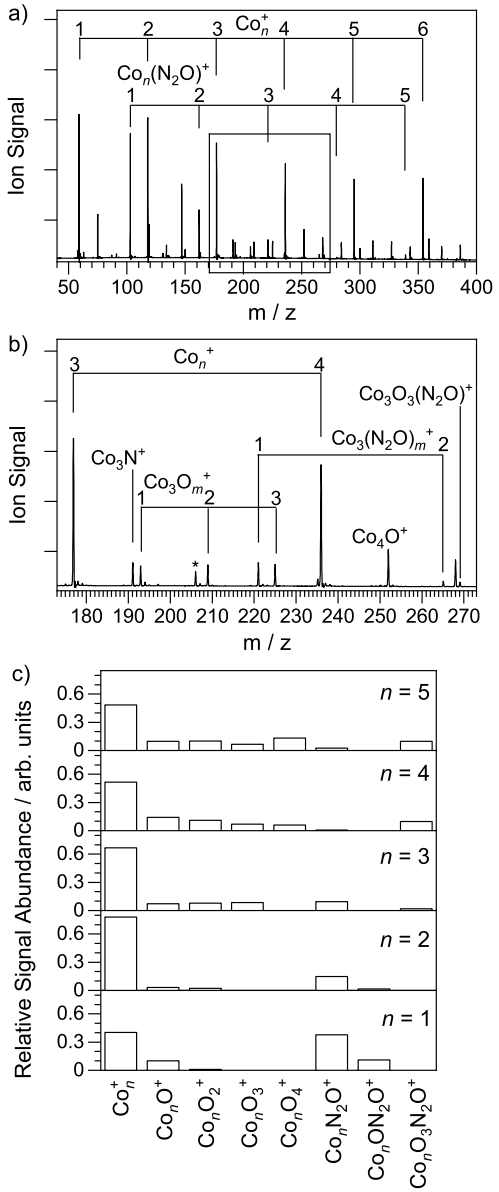

Figure 4.5.1: a) Time-of-flight mass spectrum of the ions produced following laser ablation of a cobalt rod in the presence of helium carrier gas (10 bar backing pressure) and N_2O added downstream *via* the late-mixing valve; b) shows an enlarged area of the Co_3^+ clusters, the asterisk marks $Co_2(N_2O)_2^+$ species; c) Histogram illustrating the relative abundances of each of the ion signals in the ToF mass spectrum: Co_n^+, $Co_nO_x^+$ ($x = 1{-}4$), $Co_nN_2O^+$, $Co_nON_2O^+$, and $Co_nO_3N_2O^+$. The sum of the signals within each n has been normalised to 1. The figure is adapted from Ref. [61] (https://doi.org/10.1039/D0CP05195K) with permission from the PCCP Owner Societies.

clusters produced *via* collisions with He gas molecules, there is not enough build-up in their internal energy to promote such reactions.

4.6 Summary and Conclusions

In summary, the reactivity of Au_n^+ and Co_n^+ clusters towards N_2O was examined and showed that the Au_n^+ species are relatively inert but do produce some molecularly adsorbed N_2O as well as limited Au_nO^+ reaction products. The Co_n^+ clusters were found to be more reactive with small ($n \leqslant 2$) and larger ($n > 3$) clusters being qualitatively different in their reactivity. Small ones prefer adsorbing the N_2O molecularly whereas larger ones reacting to form oxides.

The mid-IR spectral region of 1000-1200 cm^{-1} for the $Au_n(N_2O)^+$ species did not show any bands, confirming the absence of O-bound N_2O isomers in the molecular beam suggesting efficient annealing into the global minimum N-bound structures. Overall, the $Au_n(N_2O)^+$ and $Co_n(N_2O)^+$ clusters show lack of IR-driven chemistry; upon IR irradiation, the sole -N_2O loss channel is observed, unlike some of the previously investigated systems [59, 60, 108–110, 120].

To further understand the reactivity, potential energy surfaces for the reaction coordinate of $Au/Co_n^+ + N_2O$ could be explored, and would allow better understanding of the reaction products observed in the time-of-flight mass spectrum. Carrying out DFT calculations for the larger cluster ($n = 6, 7$) structures would offer completeness to the theoretical part of the study but, most likely, no new information.

Chapter 5

Cooperative Binding Effects of Oxygen and Carbon Monoxide on Anionic Gold Clusters, $Au_nO_2CO^-$ (n = 2−8, even n)

The activation of either O_2 [146] or CO [147] molecules on anionic gold clusters has been investigated by Fielicke and coworkers previously. The experiments described in this chapter we designed to determine any cooperative or competitive binding effects arising under the coadsorption conditions of both ligands. This system is relevant in surface studies: CO oxidation at low temperature is very efficient on oxide-supported gold particles [148] and it is known that the activation of O_2 is a key factor in the CO oxidation process [149]. The exact mechanism, however, is not clear, and the aim of this study is to explore the activation of the O_2 molecule by a gas-phase cluster model.

The IR-MPD spectra of $Au_nO_2CO^-$ (n = 2−8, even n) clusters are presented in both O_2 and CO stretch regions, and complementary DFT calculations reveal two different O_2 binding modes (end-on and side-on) that account for the positions of the vibrational bands observed. O_2 binding mode is dependent on the charge distribution on the Au_n^- species, as well as whether CO molecule is coadsorbed, as evident for the Au_6^- clusters.

The experiments were performed by the Mackenzie group in collaboration with

André Fielicke at the Fritz Haber Institute Berlin, utilising the FHI free electron laser [67, 68]. Preliminary analysis of the experimental results was performed by Dr Alice Green, after which further investigation, complemented with computational work, was undertaken as part of this thesis.

5.1 Introduction

Carbon monoxide is generated primarily by the incomplete combustion of fossil fuels and fires, and while not a greenhouse gas, it is an atmospheric pollutant [150]. CO participates in the reactions with hydroxyl radicals that cleanse the Earth's atmosphere not only from carbon monoxide but also from other harmful substances. Excess CO serves to deplete the amount of OH available for this beneficial purpose [151]. CO is colourless, odourless, and tasteless as well as particularly toxic resulting in a high mortality rate in the event of intoxication, which makes exposure extremely dangerous [152] .

The structures of anionic gold clusters, Au_n^- (n < 13), were determined by a combination of ion mobility experiments and *ab initio* molecular dynamics simulations by Furche *et al.* [42], and the crossover point between 2D and 3D structures was found to be $n = 12$. This result has been confirmed by photoelectron spectroscopy by Häkkinen *et al.* [132] and TIED studies by Xing *et al.* [34] and Johansson *et al.* [153]. The latter study also involved *ab initio* MD simulations that agreed with the crossover at $n = 12$. The structures of cationic and neutral gold clusters were described in Chapter 4 Section 4.1.

The adsorption of O_2 to the Au_n^- clusters has been studied by Salisbury *et al.* [154], where the authors examined the equilibria between adsorption and desorption for the $n = 2-22$ clusters by pulsed flow-reactor methods at ambient temperature. It was found that only one O_2 molecule per cluster can be adsorbed, irrespectively of n and even then, exclusively for even cluster size numbers, with no adsorption observed for odd cluster sizes. This can be understood in terms of valence electrons. Even-numbered charged clusters have an unpaired electron which pairs up with

radical adsorbates. An odd-sized gold cluster could reach saturation by adsorbing two dioxygen molecules simultaneously, however, this is statistically improbable. The mechanism involving O_2 as a one-electron acceptor into its π^* antibonding orbital is considered to account best for these observations [16].

Fielicke and coworkers [146] measured IR-MPD spectra of the $Au_nO_2^-$ (n = 4−20, even n) clusters and discovered that O_2 is activated the most when adsorbed on the Au_{10}^- and Au_{12}^- clusters in its superoxo (η^1-O_2) form or on Au_8^- in its peroxo (η^2-O_2) form. Only a single relatively narrow peak emerged in all recorded spectra, except for the Au_8^- clusters that showed multiple (seemingly three) poorly resolved peaks for which the sum of depletions exceeded 100%. These results indicated an interconversion between isomers on the μs timescale. A photoelectron spectroscopy study of the Au_8^- clusters [155] further supported this finding by revealing two coexisting different isomeric forms. With computational aid, the superoxo form was assigned as a kinetically trapped product with the peroxo form as thermodynamic ground state. The interconversion barrier of 0.4 eV was accessible under their experimental conditions. The calculations in this study as well as Yoon *et al.* [156] indicated that the most stable geometries for n = 4−6 species contain dissociatively adsorbed O_2, however, the barrier to dissociation is too high for these species to be observed experimentally.

IR-MPD spectroscopy by Fielicke and coworkers [147] was also performed independently on the Au_nCO^- (n = 3−14) clusters. The main findings include the emergence of bands typical for atop bound CO species and implications that the π^* back-donation is the main factor responsible for the activation of the C≡O bond since electrostatic effect that increases the value of ν(C≡O) was calculated to be a minor contributor. Larger π^* back-bonding is observed in smaller complexes, which can be understood in terms of charge dilution in larger complexes. As the average electron density at a specific binding site decreases with n, less electron density is available for π^* back-donation, and with n, the value of ν(C≡O) blue-shifts. A red shift in ν(C≡O) with increasing coverage was observed, suggesting deviations from

the Blyholder surface binding model [157] (observed in small Rh_nCO clusters [115]) and indicating that the π^* back-donation is less important in the CO bonding to Au_n^-, compared to most other transition metals [158]. Due to the π^* back-donation being inefficient, small contributions from the 5σ orbital (itself slightly antibonding in the C≡O bond) can affect the shift, and with each adsorbed CO molecule the amount of σ donation is reduced resulting in the observed red-shifting of the CO band [159].

DFT calculations for the Au_nCO^- ($n = 1-6$) clusters by Wu *et al.* [160] confirmed the experimental trends seen by Fielicke. Generally, CO molecules adsorb on low-coordinated sites in atop configuration and each gold atom is able to accommodate one CO ligand [161]. Häkkinen *et al.* [162] included the analysis of spatial electronic charge of Au_2CO^- and the results showed that upon CO adsorption 0.16 of electron charge was transferred into the CO π^* orbital, inducing a red shift, as expected, and leading to a change in the structure; a tilting of the CO due to the symmetry breaking of two degenerate π^* orbitals.

Interestingly, in CO and O_2 coadsorption conditions and for some n, the Au_n^- clusters have been shown to be able to participate in cooperative binding, with no competition for adsorption sites. Wallace *et al.* [16] studied the effect of one adsorbate on the binding of a second on even-sized anionic gold clusters on the equilibrium constant *via* pulsed-helium, flow-reactor techniques at room temperature. It was found that for the Au_4^- species, the probability of subsequent adsorption of the other adsorbate was enhanced by a factor of 18, and for the Au_{10}^- species, the equilibrium constant for the adsorption of CO with O_2 preadsorbed is larger than 5 (*cf.* 0.7 without O_2). In the case of Au_2^- clusters, no CO adsorption was observed without the preadsorption of O_2. The authors argued that CO acts as an electron donor whereas O_2 as an acceptor, and so, an $Au_nO_2^-$ cluster appears less negative than Au_n^- to an incoming CO molecule and increases its binding strength.

The only infrared spectroscopy study investigating coadsorption effects was carried out by Hao *et al.* [163] for the $Au_2O_2(CO)_n^-$ ($n = 2-6$) species. All the complexes investigated exhibited a core structure of $Au_2O_2CO^-$ to which other

CO molecules coordinated weakly, *e.g.* $\Delta E([Au_2O_2(CO)_2^-] - [Au_2O_2CO^-] + [CO])$ = 0.1 eV. Interestingly, the O=O bond in O_2 was less activated when coadsorbed with CO molecule(s). The DFT calculations also indicated thermodynamically preferred structures that contain the 'CO_3' moiety, but they were not observed in the experiment, possibly due to high energetic barrier of formation.

The 'CO_3' intermediate, however, is stipulated to be important in the catalytic cycle of CO oxidation with an O_2 molecule. A temperature-dependent radio frequency-octopole ion trap mass spectrometry study by Socaciu et al. [164] revealed a metastable intermediate formed at low temperatures (100-225K), for which two alternative structures exist ($Au_2CO_3^-$ and $Au_2COO_2^-$) that have a low activation barrier (0.3-0.5 eV) for CO_2 formation. Wallace *et al.* [16] also found evidence in the mass spectrum of CO_2 molecule(s) dissociation for the Au_6^- clusters under O_2 and CO coadsorption conditions. Nonetheless, there are many factors that could inhibit CO_2 generation; inefficient coadsorption of O_2 and CO, a high barrier for diffusion, and the probability of collision within the complex lifetimes. Moreover, there are energetic barriers associated with the initiation of reaction and the desorption of CO_2 to be overcome.

5.2 Experimental and Computational Methods

The experimental setup has been described in detail previously in publications [113–115] and Section 2.4. Briefly, a rotating Au rod is ablated by a 532 nm pulse from Nd:YAG laser (10 Hz) to generate the clusters in a reaction channel, after which the clusters undergo supersonic expansion into the vacuum. The ensuing cluster beam is skimmed and cluster ions detected by a reflectron time-of-flight mass spectrometer. O_2 gas is entrained in the He carrier gas and the mixture is then pulsed by a valve into the cluster source chamber at room temperature with CO introduced by a backing line directly into the reaction channel. The cluster source was cooled to -140 °C by purging liquid N_2 in order to preserve the clusters formed.

Upon absorption of resonant infrared radiation from the FEL operating at 5 Hz, some bond in the cluster can be broken either by direct irradiation or internal vibrational energy redistribution from some other cluster chromophore of multiple photons. The technique employed here measures the signal difference with alternating IR on/IR off pulses from the FEL by reflectron ToF spectrometry, and parent ion depletion with fragment(s) enhancement are recorded as a function of a wavenumber, allowing for a suitably high mass resolution and sensitivity. Information about the vibrational normal modes is obtained, giving insight into the structure of a cluster of interest.

DFT simulations, including finding energetically low-lying structures and harmonic vibrational frequencies, were completed at the def2TZVP [76, 77]/TPSSh [116, 117] level for Au atoms and at the aug-cc-pVTZ [165]/TPSSh level for C and O atoms using the Gaussian 16 software [118] package. The augmented basis set contains diffuse functions needed to describe the electron distribution of anions. To account for weak intramolecular interactions and scalar relativistic effects for Au atoms, the GD3-BJ dispersion [123] term along with the effective core potential [124] method, which freezes 60 inner electrons, were introduced. To adequately sample the conformer space, a large number of starting structures for each species were computed (for each optimised structure further ligand was added at least in 10 different ways). For the computed spectra, O_2 and CO scaling factors were used to match the calculated band position values to the experimental ones in the corresponding wavenumber regions. For ease of comparison with the experimental spectrum, the computational line spectra have been convoluted with full width at half maximum (FWHM) of 20 cm^{-1} Lorentzian shape functions. All energies reported here include zero-point corrections and are given relative to the lowest energy molecularly adsorbed structure.

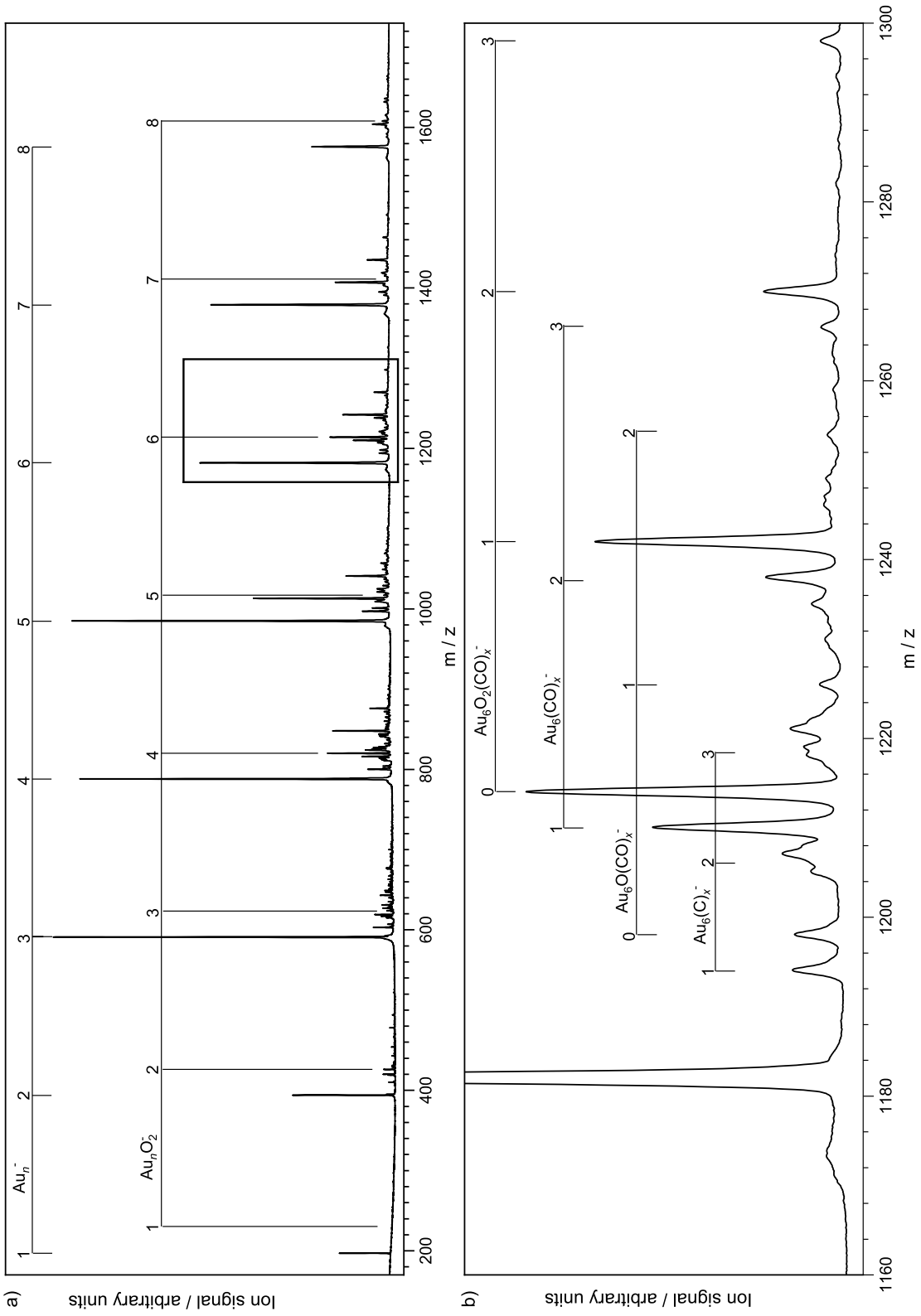

Figure 5.3.1: a) Time-of-flight mass spectrum of $Au_nO_2CO^-$ produced by laser ablation of a gold rod in the presence of 1% O_2 in He carrier gas and CO added downstream; b) shows an enlarged area of the Au_6^- clusters. The cluster source was cooled to -140 °C with liquid N_2.

5.3 Selective O_2 Binding in the Time-of-Flight Spectrum

Figure 5.3.1 shows a representative time-of-flight mass spectrum for the products formed following ablation of a gold rod in the presence of helium carrier gas seeded with 1% O_2 and CO added downstream through the late-mixing valve. An enlarged part of the mass spectrum of the Au_6^- clusters is given in b).

It is confirmed that the O_2 molecule binds to Au_n^- exclusively for even n, as evident in other studies as well [16, 154], due to even-sized Au_n^- clusters having an unpaired electron that binds with the adsorbing O_2 molecule. For $n = 2$, 4, and 6, the amount of the Au_nCO^- species produced is smaller than the corresponding amount of the $Au_nO_2CO^-$ species, and already point to some cooperative binding effects between the O_2 and CO ligands on the Au_n^- clusters in our experiment. For all even n, however, the signal of $Au_nO_2^-$ is still larger than the corresponding $Au_nO_2CO^-$, indicating no such enhanced binding effect for the O_2 molecule. Moreover, odd-sized Au_n^- clusters adsorb one CO molecule much more readily than even-sized counterparts, where the electron donation from the CO orbitals perhaps becomes more efficient without an unpaired electron on the metal cluster.

5.4 IR-MPD Spectra

5.4.1 O_2 Stretch Region (1000-1200 cm^{-1})

The IR-MPD spectra of $Au_nO_2^-/Au_nO_2CO^-$ ($n = 2-10$, even n) clusters are given in Figure 5.4.1. In the $n = 2-6$ and perhaps $Au_{10}O_2CO^-$ spectra, a single relatively narrow peak emerges which points to a single isomer giving rise to these infrared bands. The $Au_8O_2^-$ spectrum was determined to be composed of multiple bands from two different Au_8^- isomeric forms and corresponding O_2 binding motifs [146, 155].

It is important to note that all of the IR-MPD bands are strongly red-shifted (O=O bond is activated) from the unbound O_2 vibration of 1554.7 cm^{-1} [166]. Also, the signal for the $Au_2O_2CO^-$ species in this region was too small to observe the

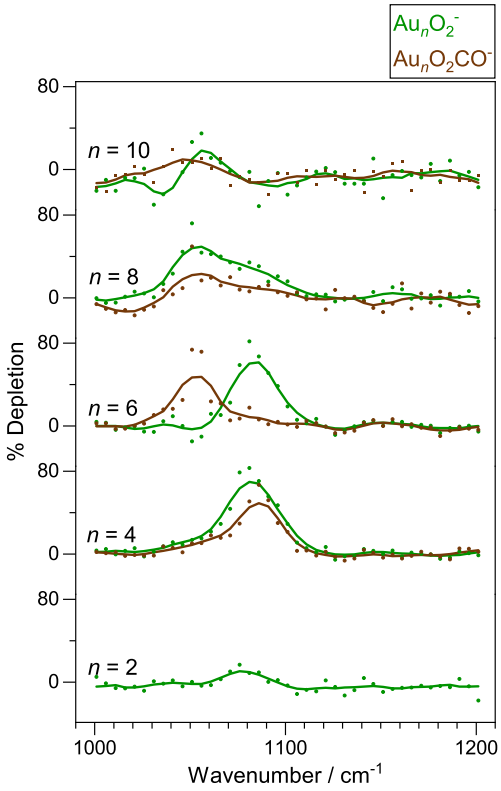

Figure 5.4.1: IR-MPD spectra of $Au_nO_2^-$ (in green) and $Au_nO_2CO^-$ (in brown) (n = 2−10, even n) clusters recorded in the 1000-1200 cm^{-1} region as percentage depletion of the parent cluster ion. The "free" O_2 vibration is at 1554.7 cm^{-1} [166].

spectrum. These clusters were scanned only after starting to heat up the source, and were not preserved in a sufficient amount.

All in all, the spectra are well-reproduced from Woodham *et al.* [146]. In the case of $Au_nO_2^-$ clusters, the observed band blue-shifts from n = 2 to 6, which is explained by charge delocalisation in larger clusters with charge transfer less efficient for larger than for smaller Au_n^- clusters. For n = 8, there is a change in the O_2 binding motif with evidence for both end-on and side-on species present in the molecular beam corresponding to the non-shifted and red-shifted portions of the band, respectively (geometries presented later in Figure 5.5.1). For n = 10, the band is red-shifted and narrow, pointing to sole side-on binding motifs of O_2 present.

Interestingly, in the coadsorption conditions, there is a very clear decrease in the band's infrared vibration frequency for n = 6 with a small shoulder where the

original band is. It may well be that a change in the binding motif is influenced by the presence of a CO ligand, with the crossover from end-on to side-on bound O_2 occurring for $n = 6$ instead of $n = 8$, as evident for the bare Au_n^- clusters. This change appears after the adsorption of a CO ligand on the cluster in the fast experimental time-frame. The differences in the spectra for other n sizes are not characteristic but the $n = 10$ clusters may present further O_2 activation with the O_2 band in coadsorption conditions broadened and with a shoulder that is red-shifted from the position of the $Au_{10}O_2^-$ band.

5.4.2 CO Stretch Region (1900-2200 cm^{-1})

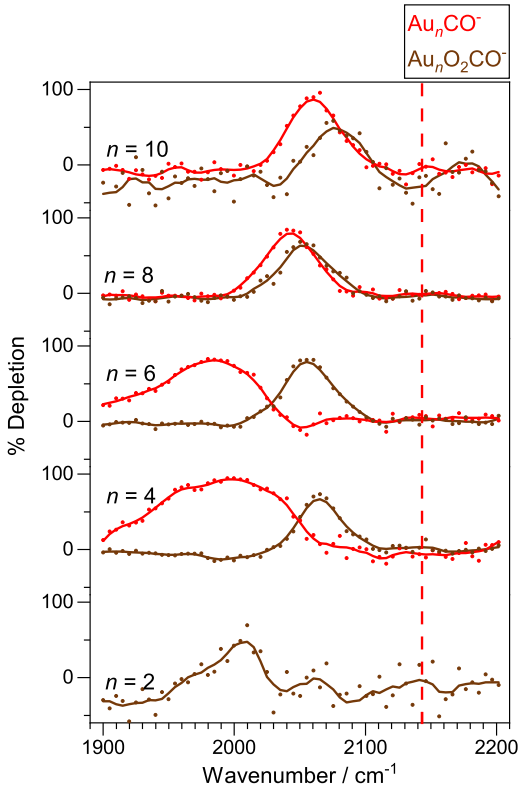

Figure 5.4.2: IR-MPD spectra of the Au_nCO^- (in red) and $Au_nO_2CO^-$ (in brown)($n = 2-10$, even n) clusters recorded in the 1900-2200 cm^{-1} region as percentage depletion of the parent cluster ion. The dashed line indicates "free" CO stretch at 2143.2 cm^{-1} [166].

The IR-MPD spectra of $Au_nCO^-/Au_nO_2CO^-$ ($n = 2-10$, even n) clusters are given in Figure 5.4.2. Here, spectral features are assigned to characteristic C≡O

stretches with a red dashed line denoting the "free" CO vibration at 2143.2 cm^{-1} [166]. Similarly to O_2, the C≡O molecule is activated in all cases albeit to a lesser degree. As mentioned previously, no Au_2CO^- species were produced in the experiment.

The bands in the spectra of the Au_nCO^- species are quite broad and undergo a small red-shift from $n = 4$ to 6. It then blue-shifts and becomes narrower for $n = 8$ before a further blue shift for $n = 10$. Fielicke *et al.* [147] measured an 80 cm^{-1} blue shift in the range of $n = 3-10$ and explained it in terms of charge dilution. The authors partially attribute the shift to electrostatic effects which were calculated using a model by Goldman and Krough-Jespersen [158] to cause a blue shift of 15 cm^{-1}. The range of the blue shift observed here is very similar to Fielicke's result.

In the spectra of $Au_nO_2CO^-$ species there is a general blue shift of the observed band going from $n = 2$ to 4 and $n = 8$ to 10 accompanied by a small red shift from $n = 4$ to 8. Upon ligation with an O_2 molecule, the position of the band considerably blue-shifts from the Au_nCO^- results for $n = 4$ and 6, and slightly so for $n = 8$ and 10. In all cases, the bands are relatively narrow.

5.5 Cooperative Binding in the Calculations

5.5.1 O_2 Binding Motifs

Figure 5.5.1 gives a comparison between the experimental and computational spectra of $Au_nO_2^-/Au_nO_2CO^-$ for $n = 4$, 6, and 8 in the O_2 stretch region. The assignment of these geometries is quite convincing in terms of the experimentally observed and calculated value of the red shift of the infrared band for $n = 6$, whereas for $n = 4$, the band position does not change. In agreement with the literature, $Au_8O_2^-$ exhibits two coexisting geometries and their stabilities are reflected in their relative areas in the experimental band. Accordingly, $Au_8O_2CO^-$ structures can be assigned as those of $Au_8O_2^-$ but with a CO molecule adsorbed − the corresponding lowest energy geometry for each $Au_8O_2^-$ isomer is shown. The apparent band at 1150-1190 cm^{-1} is determined to be an artefact due to poorer signal-to-noise ratio than for other cluster sizes.

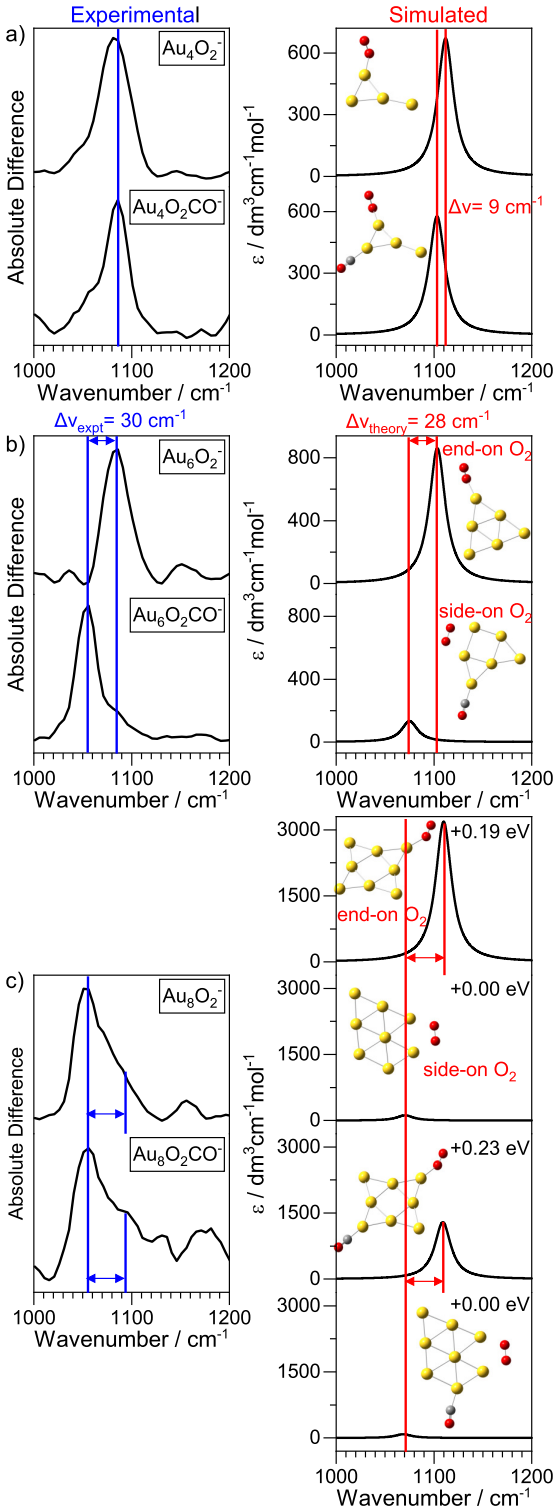

Figure 5.5.1: Putative ground state geometries and the comparison of experimental and simulated spectra of the a) $Au_4O_2^-/Au_4O_2CO^-$, b) $Au_6O_2^-/Au_6O_2CO^-$, and c) $Au_8O_2^-/Au_8O_2CO^-$ clusters in the 1000-1200 cm^{-1} region recorded as an absolute difference in the signal (IR on−IR off). Calculations support the experimental evidence for a change in the O_2 binding mode (from end-on to side-on) upon coadsorption of O_2 with CO conditions for the $n = 6$ clusters.

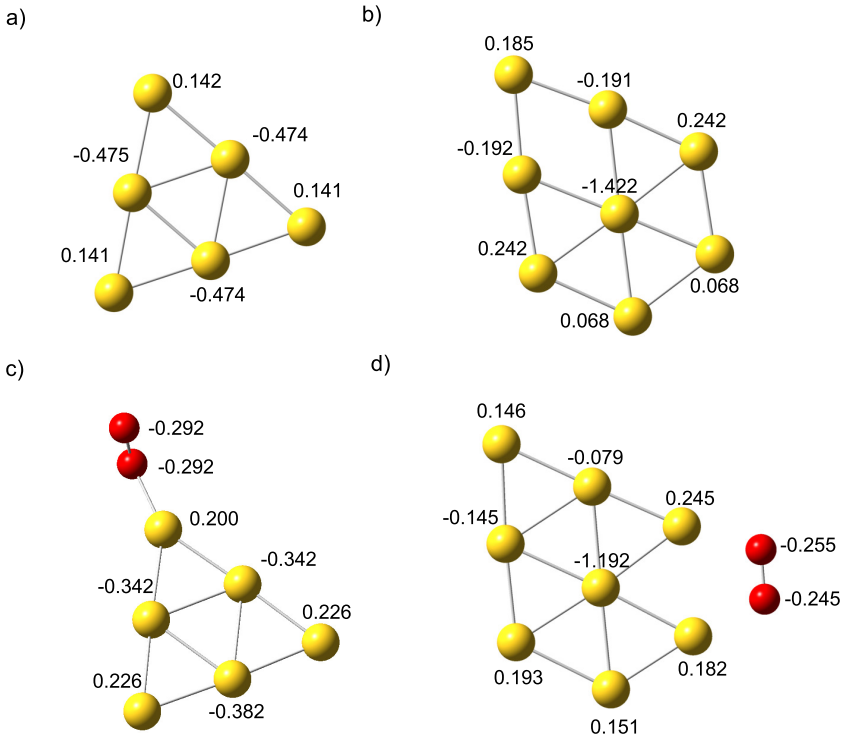

Figure 5.5.2: Partial Mulliken charges of calculated putative ground state structures for the a) Au_6^-, b) Au_8^-, c) $Au_6O_2^-$, and d) $Au_8O_2^-$ clusters.

The change in the O_2 binding mode to Au_n^- occurs at $n = 8$. In order to understand the reason an O_2 ligand adsorbs in the end-on fashion on the smaller anionic gold clusters but side-on on the larger ones, Mulliken charge populations [167] were determined. The results for the calculated putative ground state structures for a) Au_6^-, b) Au_8^-, c) $Au_6O_2^-$, and d) $Au_8O_2^-$ are given in Figure 5.5.2. It is important to note that the absolute values are not meaningful as the Mulliken analysis is strongly dependent on the basis set used [168, 169], however, relative values can be compared.

From Figure 5.5.2, the vertex atoms of the Au_6^- cluster have a positive charge whereas the ones adjacent to the vertices have a negative charge. The charge populations on the Au_8^- cluster show clear differences; there are no such positive-negative charge oscillations between the neighbouring atoms where the O_2 ligand is bound, as the Au_8^- cluster possesses a lower symmetry than the Au_6^- cluster. Seemingly, in order to not induce any changes to the core structure (which would

be energetically costly) O_2 binding is regioselective with respect to the partial charge distribution. If there is a positive-negative charge density difference of the neighbouring gold atoms, O_2 will bind in an end-on fashion. For both Au_6^- and Au_8^-, upon O_2 adsorption there is some negative charge transfer to the O_2 ligand, as expected from the aforementioned bonding mechanism.

The most intriguing finding in this chapter involves the red shift of the O_2 band for $n = 6$ upon adsorbing a CO molecule (Figure 5.5.1). It is indeed caused by a change in the O_2 binding mode with a slight distortion of the Au_6^- core cluster which has an isosceles triangle geometry (confirmed by Furche *et al.* [42] as well). Overall, for the $n = 6$ cluster, DFT calculations suggest that it is thermodynamically favourable to accommodate a CO ligand by changing the geometry of the core cluster as well as the mode of O_2 binding.

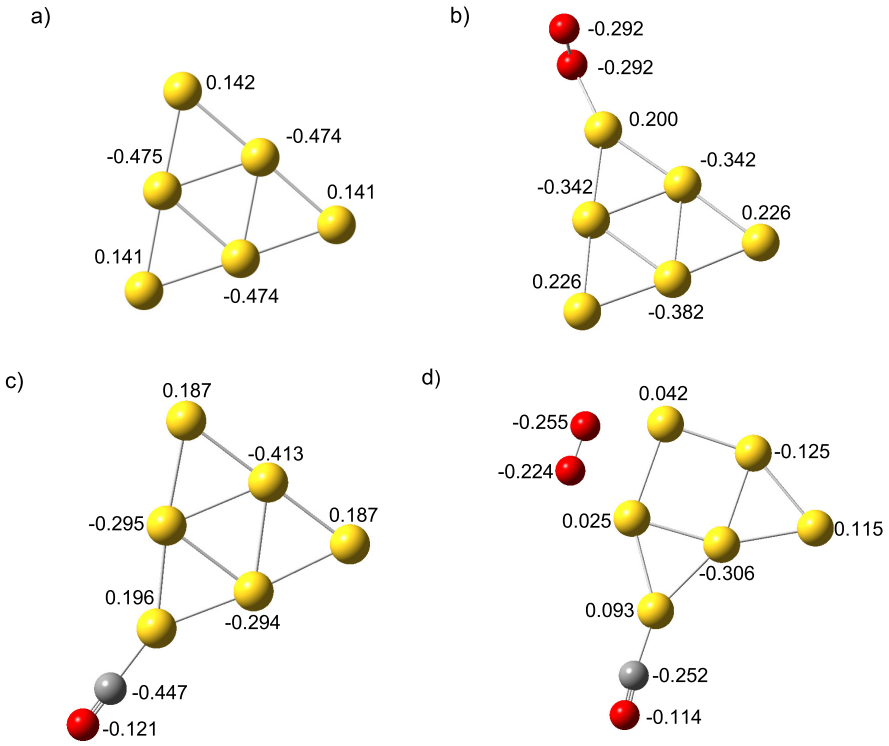

Figure 5.5.3: Partial Mulliken charges of calculated putative ground state structures for a) Au_6^-, b) $Au_6O_2^-$, c) Au_6CO^-, and d) $Au_6O_2CO^-$.

It was also concluded from the calculations that the adsorption of either an O_2 or

a CO ligand on the Au_6^- vertex site preserves the core structure of the gold cluster. However, upon adsorption on the adjacent site, the core structure rearranges itself. This is likely due to perturbation of the charge distribution, and introduction of a CO ligand to the Au_6^- cluster alters this charge distribution such that an O_2 ligand is preferentially adsorbed in the side-on fashion. Again, the Mulliken charge populations can be used in order to try to understand this. Figure 5.5.3 displays the results for the calculated ground state geometries for a) Au_6CO^-, b) $Au_6O_2CO^-$, and c) Au_6^-. By comparison of c) to a) and b) it can be seen that the least negative gold atom site that is between the vertices and next to the location of the ligand is in the case of Au_6CO^-. This may explain why upon CO coadsorption in structure d) an O_2 ligand can bind to this site in the side-on fashion, rationale being similar as for the mode of O_2 binding to the bare anionic gold clusters. Moreover, for the $n = 6$ cluster, electron density from the CO σ orbital may be transferred into the π^* antibonding orbital, thus, showing cooperative binding effects. If this was true, the C=O bond would be strengthened, resulting in a blue shift of the band in the 1900-2200 cm^{-1} region. This is shown in Figure 5.4.2.

5.5.2 CO Binding Motifs

A blue shift is also observed in the C=O stretch region for the $n = 4$ species (Figure 5.4.2) even though there is no accompanying O_2 red shift for this cluster. This may be clue to the Y-shaped structure of the bare Au_4^- cluster (confirmed by Furche *et al.* [42]). Due to steric hindrance, an O_2 ligand is unlikely to change coordination mode and adsorb in the side-on fashion. The comparison between experimental and computational spectra in the CO stretch region of the putative ground state structures of $Au_nO_2^-/Au_nO_2CO^-$ for $n = 4$, 6, and 8 for each species, as well as another energetically higher lying structure for $Au_8O_2CO^-$ is given in Figure 5.5.4. The band stays at the same position for the $n = 8$ cluster with and without adsorbed O_2, presumably because no change in the O_2 binding is observed (Figure 5.5.1).

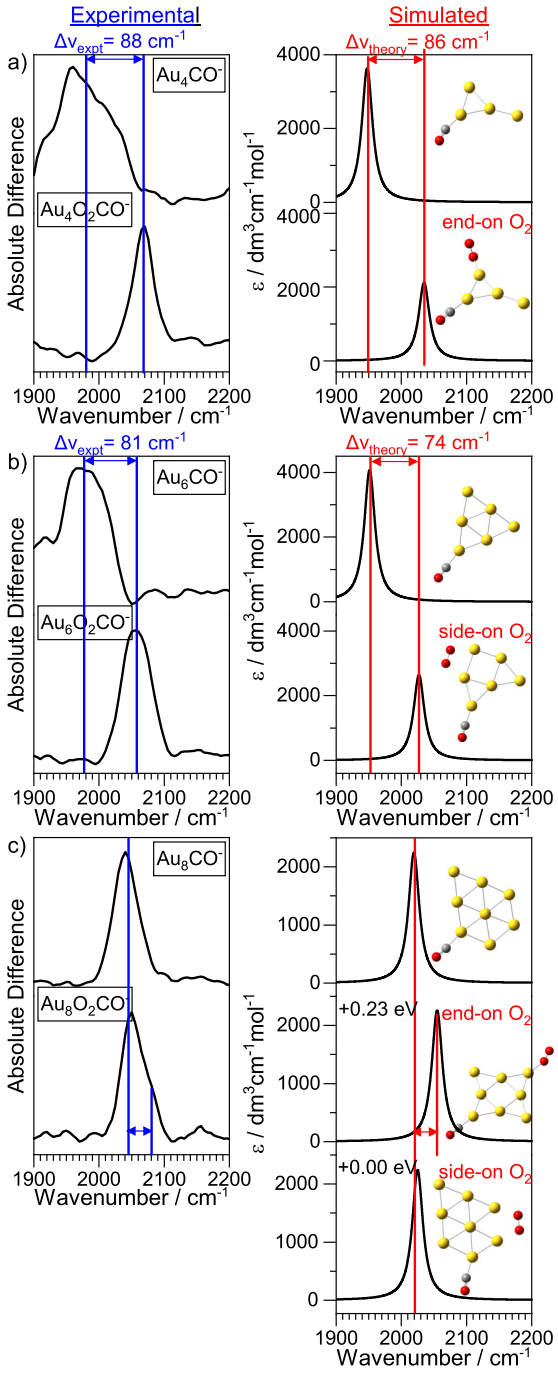

Figure 5.5.4: Putative ground state geometries and the comparison of experimental and simulated spectra of the a) $Au_4CO^-/Au_4O_2CO^-$, b) $Au_6CO^-/Au_6O_2CO^-$, and c) $Au_8CO^-/Au_8O_2CO^-$ clusters in the 1900-2200 cm^{-1} region recorded as an absolute difference in the signal (IR on−IR off).

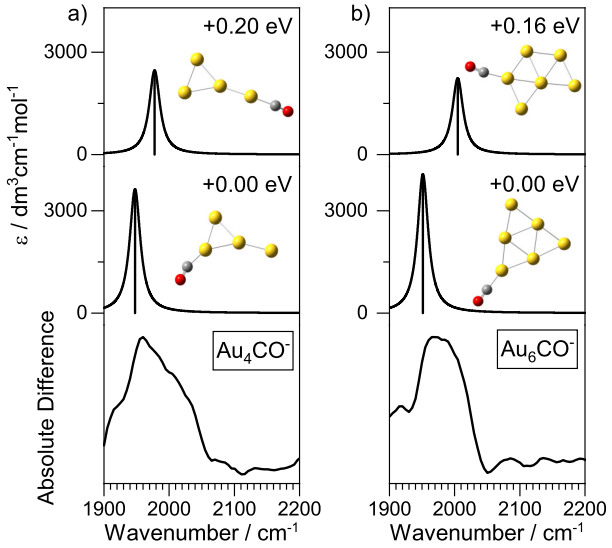

Figure 5.5.5: Low-lying computed isomers and the comparison of experimental and simulated spectra of the a) Au_4CO^- and b) Au_6CO^- clusters in the 1900-2200 cm^{-1} region; all calculated isomers with a suitable spectral agreement are given.

Similarly to the spectrum in O_2 region, a shoulder to the right is observed that points to a small abundance of the +0.23 eV isomer.

5.5.3 Possibility of Coexisting Isomers

Au_4CO^- and Au_6CO^- have notably broad bands that could originate from different isomeric forms. Figure 5.5.5 shows the likely geometries (the structures that contained either a bridging CO ligand or a 3D gold core structure were rejected and are not shown; these decisions were based on the available literature [147, 160, 161]).

Figure 5.5.6 shows the structures of the $Au_nO_2CO^-$ (n = 6, 8) species that are similar to putative ground states and cannot be discarded due the similarity in their vibrational spectra. Taking $Au_4O_2CO^-$ as a reference point, its bands are sharp, and the energetically closest isomer is 0.28 eV higher in energy than the putative ground state. For n = 6 and 8, this energy gap is much smaller (less than 0.10 eV), and thus, these structures lie within the DFT uncertainty and might coexist in the molecular beam.

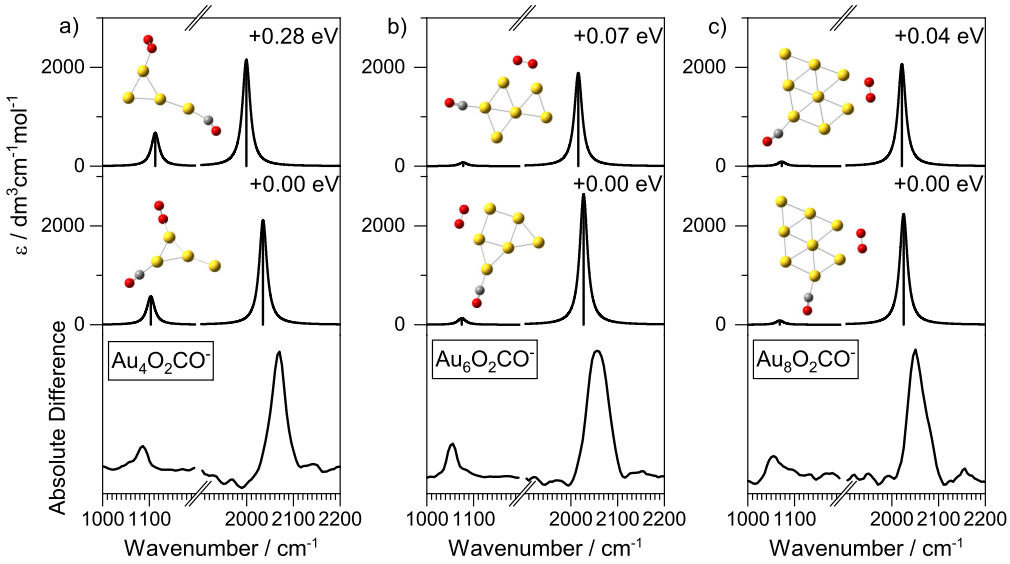

Figure 5.5.6: Low-lying computed isomers and the comparison of experimental and simulated spectra of the a) $Au_4O_2CO^-$, b) $Au_6O_2CO^-$, and c) $Au_8O_2CO^-$ clusters in the 1000-1200 and 1900-2200 cm^{-1} regions.

5.5.4 Binding Energy Considerations

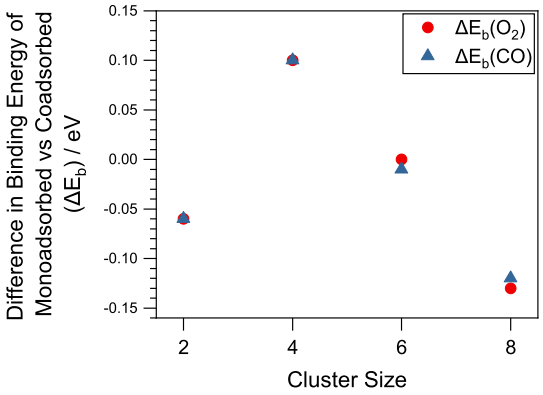

Figure 5.5.7: Differences in the O_2 (red circles) and CO (blue triangles) binding energies between the monoadsorbed ($Au_nO_2^-$ and Au_nCO^-, respectively) and coadsorbed ($Au_nO_2CO^-$) species for $n = 2–8$, even n. Positive difference indicates that the binding energy of monoadsorbed ligand is lower than the corresponding ligand's binding energy in coadsorption conditions.

Figure 5.5.7 shows calculated differences in the O_2 and CO binding energies between the monoadsorbed ($Au_nO_2^-$ and Au_nCO^-, respectively) and coadsorbed ($Au_nO_2CO^-$) species for the putative $n = 2–8$ (even n) ground state structures in

each case. Positive difference indicates an increase in the adsorbant's binding energy to the anionic gold cluster upon coadsorption of the other ligand, *i.e.* cooperative binding effects. Such an outcome is calculated for the $n = 4$ cluster for both O_2 and CO and for $n = 6$ for O_2 exclusively. This is not entirely what was expected from the binding energy considerations. From mass spectra, an enhanced coadsorbed $Au_nO_2CO^-$ (n = 2, 4, and 6) signal was observed when compared to the respective monodsorbed Au_nCO^- with no Au_2CO^- species produced at all in Section 5.3. Regarding $Au_nO_2^-$, for n = 2, 4, and 6, the amount of the monoadsorbed O_2 species produced was larger than the corresponding $Au_nO_2CO^-$ − the calculated binding energy differences should possess positive values in Figure 5.5.7.

5.6 Summary and Conclusions

In conclusion, IR-MPD spectra of the $Au_nO_2^-$, Au_nCO^-, and $Au_nO_2CO^-$ clusters were recorded in both O_2 and CO stretch regions for even n sizes. For n = 2, 4, and 6, clear cooperative binding effects were noticed in the mass spectrum, and exceptionally for $n = 6$ in the infrared vibrational analysis. The key finding was the change in the O_2 binding mode upon coadsorption conditions with a CO ligand on the Au_6^- cluster. DFT calculations were also performed to rationalise the experimental results but computed binding energies did not succeed in explaining the observed cooperative binding effects in the mass spectra.

There is some scope for further analysis. One of them would be to perform calculations for the $n = 10$ species to reveal whether different isomers are a cause for such broad bands in the O_2 stretch region. More comprehensive analysis of charge density could also be done, for example, using Hirshfeld charge analysis [170] that is not basis set-dependent as the Mulliken counterpart. The reason for O_2 activation could then be investigated, and particularly whether the negative charge transfer is directly responsible for this activation. The calculated lowest energy structures for all n contain a 'CO_3' moiety and the region where these bands are found (1200-1700 cm^{-1}) was not scanned in our study. However, it is unlikely that

these structures form in our experimental conditions as a similar experiment for $n = 2$ found no such evidence [163] and only in thermally excited clusters were the corresponding species containing 'CO_3' produced [164].

Spectroscopic work on mixed ligand systems is scarce, and investigation of other mixed ligand systems, *e.g.* N_2O and CO on anionic gold clusters, might produce interesting results, such as evidence of activation or even a reaction between these ligands.

Part B. Multiple Ligands on a Single Metal Centre

Chapter 6

NO Binding at Group 9 Metal Centres: $Co(NO)_n^+$ and $Rh(NO)_n^+$ ($n \leqslant 8$)

This chapter presents an IR-PD study of the NO complexes of Group 9 ions – $Co(NO)_n^+$ and $Rh(NO)_n^+$; it is the first such study that involves radical species in the Mackenzie group laboratory. The work on the $Ir(NO)_n^+$ system is currently being carried out and will provide opportunity to compare the results of the whole Group 9 triad. The findings are being prepared for publication.

The infrared photodissociation spectra of $Co(NO)_n^+$ and $Rh(NO)_n^+$ ($n = 3–7$) clusters recorded in the NO stretch region reveal the formation of NO dimer for the $n \geqslant 5$ complexes giving rise to "satellite" bands. The spectra in each case are different in terms of the number and position of the bands, and are rationalised with DFT assistance. The open shell nature of NO represents a particular challenge for DFT.

The experiments were performed in the Mackenzie group laboratory in Oxford; the studies concerning cobalt and rhodium nitrosyls were led by me and DPhil student Philip Pearcy, respectively, with assistance of part II student Olga Duda and Dr Alice Green. Initial computational work was performed by several Mackenzie group members but the final set of structure optimisations for both metals and the subsequent analysis of all results were carried out by me. Regarding the pure nitrosyl clusters, the experimental and computational campaign was led by me.

6.1 Introduction

Nitrogen oxides (NO_x) are known for their detrimental effect to the environment as well as the human system − a few of many examples include their role as precursors to the photochemical smog as well as acid rain and as contributors to respiratory diseases in humans [171]. They are produced both naturally (*e.g.* lightning, forest fires) and anthropogenically *via* burning fossil fuels and automobile gas exhaustion. NO_x species are a family of seven compounds, however, the most prevalent and highly regulated one is nitrogen dioxide [172]. Both NO and NO_2 are released by the combustion engines [173], which can then react and release highly reactive hydroxyl radicals that take part in various photochemical reaction cycles [174]. While toxic at higher concentrations in the body, the NO molecule has a crucial role in helping to maintain the blood pressure and is involved in the long-term memory biochemistry [175, 176].

Current strategies to mitigate the atmospheric emission of NO_x gases from automobile exhausts include the use of the three-way catalytic converter [177]. This contains finely dispersed Pd, Pt, and Rh particles that initiate a reaction between unburnt hydrocarbons, CO, and NO_x yielding N_2, CO_2, and H_2O. Such catalytic solutions are commonplace and yet, are poorly understood.

The complexation of NO^+ and $(NO)_n$ ($n = 1-10$) has been studied in a pulsed electron-beam high-pressure mass spectrometer by Hiraoka *et al.* [178]. It was found that the clusters with even n are more thermodynamically stable due to the electron-pairing effect in $(NO)_2$ and that $NO^+(NO)_2$ forms a core to which additional NO molecules adsorb for $n > 2$. Similar electron-pairing effects were also observed in laser ionisation mass spectrometry studies [179, 180].

The nitrosyl dimer in its cationic [181–184], neutral [185–187], and anionic [181, 183, 184, 188, 189] charge states has been studied extensively *via* infrared matrix isolation spectroscopy as well as by gas-phase IR spectroscopy [190–194]. There is no general agreement as to whether the $ONNO^+$ structural arrangement is *cis* or *trans* and a suite of computational work with various levels of theory [195–198]

has been undertaken aiming to provide assistance in explaining the experimental results. Theoretical studies regarding the neutral dimer structure are more coherent in their *cis* structural assignment. However, the geometrical parameters predicted do vary [199–204]. Urban *et al.* [205] summarise and review the experimental and computational work completed for the nitrosyl dimer and its ions.

Hoshina *et al.* [206] investigated $(NO)_n$ clusters in He droplets by infrared depletion spectroscopy complemented with multireference second order perturbation (MRMP2) theory calculations. Analysis revealed that $(NO)_3$ assumes a $cis-$dimer structure with a weakly-bound NO molecule whereas $(NO)_4$ involves two weakly interacting *cis*-dimer units. The anionic trimer has been studied by matrix isolation spectroscopy by Lugez *et al.* [183]; an $(NO)_3^-$ geometry containing all NO molecules *cis* to each other (C_{2v}) was determined, and this species was found to photodestruct into the $N_2O\cdots NO_2^-$ complex.

Regarding the bonding of NO to transition metals, the interaction of NO and Co atoms in cryogenic Ar matrix was studied by FT-IR spectroscopy [207]. The reactivity of Co^+, Rh^+, and Ir^+ with NO was investigated by inductively-coupled plasma/selected-ion flow tube (ICP/SIFT) tandem mass spectrometry by Blagojevic *et al.* [208]. Interestingly, for all three metals, novel second order NO chemistry was found. The final products for Co^+ and Ir^+ are their oxides and the release of N_2O with Ir^+ also forming a small amount of $IrNO^+$, and for Rh^+; RhNO + NO^+ as well as $RhNO^+$. NO bonding on the extended metal surfaces has also been studied, and a recent review presents the NO adsorption mechanisms on extended metal surfaces by scanning tunnelling (STM) and atomic force microscopies (AFM) [209].

Computational work involving NO bonding at metal centres is scarce; the radical nature of the NO molecule increases the complexity of such studies. Nevertheless, DFT calculations were carried out for the CoNO species and the NO ligand was found to bind preferably in a bent fashion *via* the N atom as a result of the occupied σ^* molecular orbital that arises from the interaction of 5σ MO of NO with d_σ orbital of Co [210]. DFT and coupled cluster with single and double (and perturbative

triple) excitations (CCSD(T)) calculations for $CoNO^+$ showed that the preferred geometry is linear *via* the N atom arising primarily from the d^{n+1} state of Co [211].

NO adsorption on Co_n^+ clusters ($n = 2-4$) was found to be dissociative for $n =$ 3 and 4 by oxygen displacement experiments by Klaassen *et al.* [212], similarly to Co(0001) surface at low coverages investigated by Bridge *et al.* [213]. Dissociative binding of NO to Co_n^+ was also found for $n = 3-5$ in single and for $n = 5-10$ in two-particle collision conditions in the beam-gas geometry in a tandem mass spectrometer by Hanmura *et al.* [214, 215].

These results are reminiscent of the NO reactions with Co^+ and $Rh_n^{+/-}$ clusters using single-collision FT-ICR mass spectrometry published previously by the Mackenzie group [141, 216–218], where N_2 production was evident for $12 < n < 20$ and $n < 17$, respectively. Koyama *et al.* [219] studied Co_n^+ ($n = 4-9$) by thermal desorption spectroscopy in multiple collision conditions in helium and found no evidence for dissociative NO adsorption. In this case, the clusters experience sufficient collisional cooling such that the barrier to NO dissociation is not overcome.

Rh_n^+ ($n = 6-16$) clusters were investigated *via* IR-MPD spectroscopy and DFT methods by Bakker, Mafuné, and coworkers [220, 221]. Generally, only a small percentage of NO was found to be adsorbed dissociatively on Rh_n^+ and was dependent on n. For Rh_6^+, the DFT calculations indicated that dissociatively adsorbed NO is the thermodynamically preferred product, however, due to the kinetic barrier to NO cleavage, it could not be accessed. In order to understand this better, the authors performed a similar study of the Ir_6^+ cluster [222], and concluded that 50% NO dissociation on Ir_6^+ occurs due to its larger oxygen atom affinity (oxophilicity). In accordance with these findings, the barrier to NO cleavage was lowered upon substitution of one Rh atom to Ir in the Rh_5Ir^+ cluster [223].

The reactivity, infrared matrix isolation, and computational studies for small neutral Co group clusters Me_n ($n = 1-3$) are summarised by Andrews and Citra [224]. For larger clusters, a recent review by Bakker and Mafuné [225] presents the

experimental and computational studies of NO adsorption on largely rhodium-based clusters.

Infrared photodissociation studies have been performed for the $(NO)_n^+$ [226, 227], $SF_6(NO)_n^\pm$ ($n = 3-31$) [228–230], and $C_2H_4(NO)_n^+$ ($n = 2-20$) [228, 231] clusters by Stace and coworkers and for $Me(NO)_n^+$ (Me = Fe^+, Cu^+, Ag^+, and Au^+) systems by Mingfei Zhou and coworkers [232–234], who also carried out DFT calculations.

6.2 Experimental and Computational Methods

The time-of-flight and IR-PD spectra were recorded in the Mackenzie laboratory in Oxford. The experimental setup has been described in detail in the publication by Iskra *et al.* [235] with recent modifications to include the mass selection of ions via the quadrupole reported by Green *et al.* [62, 236]. In this thesis, Section 2.3 contains the full description of the instrument, and only a brief one is given here.

A rotating disc target of either Co or Rh is ablated by a Nd:YAG laser (532 nm, 10 Hz). Ablated atoms cool and cluster by colliding with 1.5% NO entrained in Ar carrier gas in the reaction channel. The resulting gas mix, now entrained with a range of metal-ligated as well as pure NO clusters, is expanded into the vacuum forming a molecular beam which is then skimmed and mass-selected in the QMF/QMB assembly before entering the extraction region of a reflectron ToF mass spectrometer with cationic detection mode. The experiment is run at room temperature, however, the actual temperature (or internal energy distribution) of the molecular beam is not easily determined, as it is highly dependent on how well the clusters are thermalised in the reaction channel and/or cool in the expansion.

In order to record the IR-PD spectra, the cluster beam is subjected to alternate pulses of IR off/IR on from the tunable table top OPO/OPA system operating in the 1600-2000 cm^{-1} range. The resulting depletion of the parent ion and any enhancement of the daughter(s) channels are recorded as a function of wavenumber. The information on the infrared active modes of the parent cluster as well as dissociation yields are produced, and can be readily compared with the results of

DFT simulations. The spectra recorded in this chapter are plotted in terms of normalised cross section of an enhancement channel, calculated using a modified Beer-Lambert law (Section 2.5).

Energetically low-lying structures and any relevant transition states connecting them have been calculated at the def2TZVP [76, 77]/B3P86 [237, 238] level using Gaussian 16 software package [118]. This functional proved to provide reliable results in similar studies by our group in the past [62, 104, 105, 235]. To provide a better match with experimental data, computed harmonic vibrational frequencies were scaled by a factor of 0.9347, determined by calculating the vibrational frequency of the "free" NO stretch [166, 190], and convoluted with FWHM = 8 cm^{-1} Lorentzian shape curves, and any reported experimental wavenumber numerical values have an error of ± 10 cm^{-1}. All energies reported here are given relative to the zero-point energy in addition to the lowest energy molecularly adsorbed structure energy. Potential energy profiles were generated by identifying plausible transition states between two minima and performing IRC [126, 127] calculation in order to verify the correct path.

6.3 Time-of-Flight Spectra

6.3.1 Cobalt

A typical time-of-flight mass spectrum produced by laser ablation of Co target in presence of NO seeded in Ar is given in Figure 6.3.1. The mass spectrum is dominated by the $Co(NO)_n^+$ peaks. Smaller mass species are favoured, however, there is a visible decrease in the intensity of the signal from $n = 4$ to $n = 5$. This suggests a coordination sphere of four ligands but may reflect differing production efficiency under the conditions employed.

Another progression is due to the $CoO(NO)_n^+$ peaks, formed in significant quantities for $n = 0{-}1$. For $n = 1$, the signal is almost as intense as the signal of $Co(NO)^+$ species and is caused either by the NO_2 impurities found normally in unpurified NO gas adsorbing on the metal atom, oxide layers on the metal surface, or

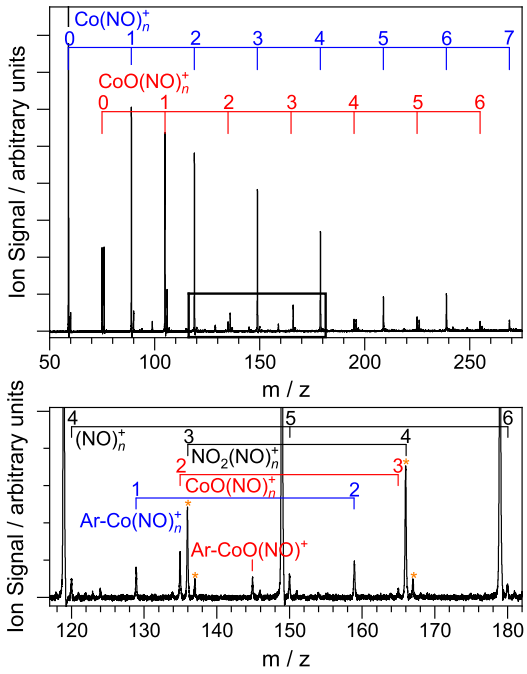

Figure 6.3.1: Time-of-flight mass spectrum produced upon ablating Co metal target in presence of NO in Ar gas mix (1.5%). The bottom panel shows an expanded region indicated in the top panel. Orange asterisks mark peaks that arise from possible water contamination.

reactions of $(NO)_n^{0/+}$ clusters with the $Co^{+/0}$ metal centre. The extent of the latter process can be estimated by the amount of CoO^+ formed since this corresponds to the oxygen transfer and N_2O release during the reaction between Co^+ and two NO molecules. Then, $CoO(NO)^+$ is produced by adsorbing an NO ligand on the CoO^+ species. Some amount of $CoO(NO)^+$ may also be produced by $Co(NO)^+$ reacting with two NO molecules, however, this process involves more steps and most likely is not a major cause of the $CoO(NO)^+$ signal observed. Since the intensity of the CoO^+ peak is more than twice smaller than the $CoO(NO)^+$ peak (Figure 6.3.1), it has to be assumed that the NO_2 impurities are a major contributor to the $CoO(NO)^+$ signal observed along with the reactions between the Co metal centre and nitrosyl clusters. Oxide layers are suggested to not contribute much or at all since the metal surface is constantly ablated by the laser and the target is kept under vacuum.

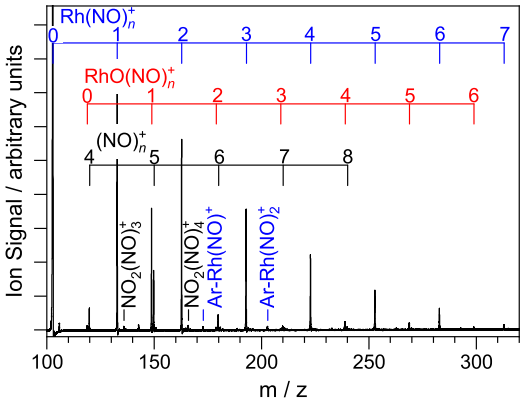

Figure 6.3.2: Time-of-flight mass spectrum produced upon ablating Rh metal target in presence of NO in Ar gas mix (1.5%).

6.3.2 Rhodium

Using the same methodology as in the Co case, a typical ToF mass spectrum produced using the Rh target is shown in Figure 6.3.2. The mass spectrum is dominated by the progression of $Rh(NO)_n^+$ peaks that decrease monotonically with n.

Regarding the $RhO(NO)_n^+$ species, a significant amount is formed for $n = 1$ solely, suggesting it is actually the $Rh(NO_2)^+$ species and not $RhO(NO)^+$. Unlike in the Co case, the RhO^+ signal is small and few other reaction products are formed. All in all, Rh appears to be less reactive than Co, consistent with the results of the ICP/SIFT mass spectrometry study [208], where Co^+ forms its oxides and Rh^+ does not.

6.3.3 Iridium

Using same methodology, a typical ToF spectrum produced using the Ir target is shown in Figure 6.3.3. Iridium has two stable isotopes of 191 and 193 mass units, which results in an increased number of peaks within the mass spectrum. Still, it appears to be richer than in the case of Co and Rh. Regarding the coordination sphere, the drop in the intensity of the signal is visibly pronounced between $n = 3$ and 4 but this number is only indicative of the relative populations and could be due to the way the mass spectrum was recorded or the conditions within the source that drive the complex formation. Overall, the mass spectrum is dominated by the

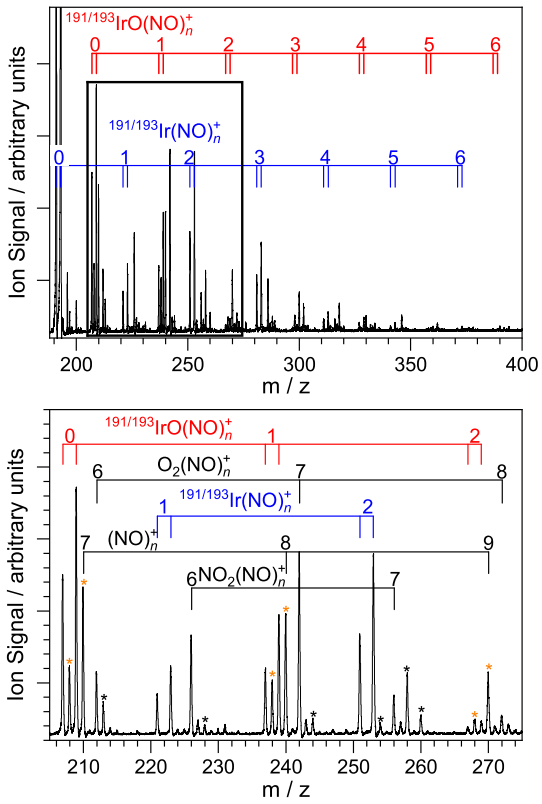

Figure 6.3.3: Time-of-flight mass spectrum produced upon ablating Ir metal target in presence of NO in Ar gas mix (1.5%). The bottom panel shows an enlarged region indicated in the top panel. Orange and black asterisks mark peaks that arise from possible water contamination and pure $(NO)_n^+$−containing species, respectively.

progression of $Ir(NO)_n^+$ peaks with smaller mass species favoured, but, unlike for Co and Rh, the intensity of $n = 2$ signal is larger than for $n = 1$.

Another progression is due to $IrO(NO)_n^+$ peaks, formed in more significant quantities for all n, *cf.* Co and Rh. The large IrO^+ signal suggests that the $IrO(NO)^+$ species primarily arises due to Ir participating in the reaction with NO molecules and promoting the release of N_2, which in turn suggests that Ir is the most reactive metal towards NO of the group 9 triad.

For all metals, there is evidence of the lone $(NO)_n^+$ clusters along with their $NO_2(NO)_n^+$ counterpart that are not adsorbed on the metal atom, which are produced within the ablation plasma. For Co, peaks arising possibly due to the $OH(NO)_n^+$ species are marked by asterisks; an indication that there is water contamination in our instrument. Masses of the $CoOH(NO)_n^+$ species coincide with masses of the

$NO_2(NO)_n^+$ progression, however, there is sufficient evidence that both are being formed in the lower mass than Co atom mass region. The water contamination is also observed in the $IrOH(NO)_n^+$ series; additionally, their masses overlap with the $(NO)_n^+$ progression but in a similar way it is also determined that both species are produced in the molecular beam.

6.4 IR-PD Spectra

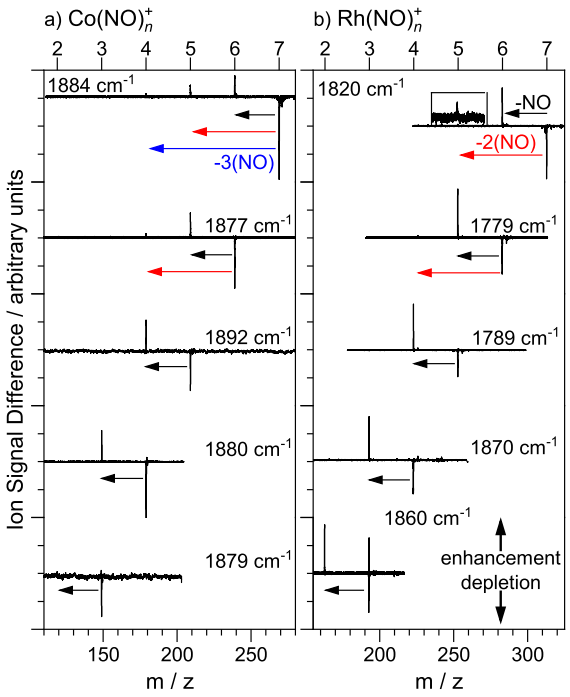

Figure 6.4.1: Time-of-flight mass spectra for the a) $Co(NO)_n^+$ and b) $Rh(NO)_n^+$ ($n = 3-7$) species recorded with IR laser on and at maximum resonance wavenumbers, as indicated. Enhancement and depletion correspond to the peaks pointing up and down, respectively. The -NO, -2NO, and -3NO loss channels are specified by black, red, and blue arrows, respectively.

An example of recorded mass spectra for both $Co(NO)_n^+$ and $Rh(NO)_n^+$ showing the depletion of the parent ion (negative signal) and the enhancement(s) of the daughter ion (positive signal) is shown in Figure 6.4.1. The parent ion is mass-selected, and for each n, the ToF spectrum is showed at the maximum resonance band with the IR laser. For all n, loss of one NO molecule is observed, from

$n = 6$ also showing 2NO loss for both metals, and, exclusively for $Co(NO)_7^+$, 3NO loss. An enhanced stability of $n = 4$ for the Co and $n = 4$ and 5 for the Rh complexes is suggested.

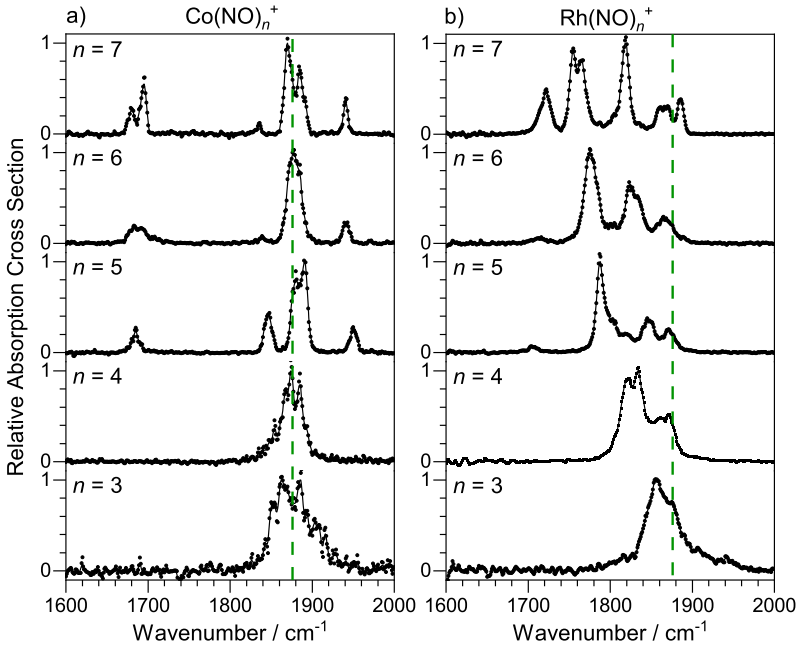

Figure 6.4.2: IR-PD spectra of the a) $Co(NO)_n^+$ and b) $Rh(NO)_n^+$ ($n = 3$–7) complexes presented as relative absorption cross sections and normalised to 1 for each n. The green dashed line indicates the "free" NO stretch at 1876 cm^{-1} [166, 190].

The IR-PD spectra of the $Co(NO)_n^+$ and $Rh(NO)_n^+$ ($n = 3$–7) complexes recorded in the loss channel of one NO molecule are showed in Figure 6.4.2. In the case of Co, for $n = 3$, 4, the bands are broad − suggestive that multiple photons are needed in order to promote the loss of an NO molecule, with $n = 4$ band slightly narrower. The closing of the coordination sphere for Co at $n = 4$, also indicated in the mass spectrum (Figure 6.3.1), is apparent by more intense and well-resolved narrow bands in the spectrum of the $n = 5$ species. In the case of Rh, there is less distinct difference between the linewidth of the bands within n as for Co. These observations will be explored by theoretical calculations in Section 6.5.

With n, the position of the most intense band does not seem to change much for Co, with spectra reminiscent of the $Fe(NO)_n^+$ complexes [232]. For Rh, however, spectral intensity red-shifts with n, and an additional band grows to become as

intense at $n = 7$. Additionally, for Rh, the band that is least red-shifted with respect to the "free" NO stretch stays at the same position with n, similarly to Co but much less pronounced in its intensity.

For both metals at $n = 5$ in the region of 1680-1720 cm^{-1}, a new binding mode appears, which suggests an increased stability of $Me(NO)_4^+$ clusters acting as a core. Mingfei Zhou and coworkers assigned this band as the signature of NO dimer in multiple publications [232–234]. In the case of Co, this extra peak evolves into more peaks that are not well-resolved for $n = 6$ but appear as a doublet for $n = 7$ (possibly two NO dimer motifs with low symmetry). For Rh, while the intensity of the extra peak is low for $n = 5$, it grows for $n = 6$, and is quite intense for $n = 7$; similarly to Co, the position remains relatively unchanged. In all cases, this red-shifted "satellite" peak is accompanied by another blue-shifted peak in the region of >1900 cm^{-1}. This blue-shifted peak was also observed by Duncan and coworkers in similar studies of the $Co(CO)_n^+$ and $Rh(CO)_n^+$ complexes [29, 239], where it was assigned to the CO molecules adding to the external coordination sphere, with their bonds strengthened as a result of electrostatic ligand polarization for both metals and an additional ligand-surface repulsion effect for the Co complexes.

6.5 Plethora of Low-Lying Isomers

The NO molecule can bind to a metal centre either in a bent or linear fashion, donating one or three electrons, respectively [240]. The calculated putative ground states for the $Me(NO)_3^+$ (Figure 6.5.1) have doublet electronic states and involve all NO molecules bound in a linear fashion for the Co complex (D_{3h}) and bent for the Rh complex (C_{3v}). As these are d^8 metals, $Co(NO)_3^+$ has 17 valence electrons whereas $Rh(NO)_3^+$ has 11. The 18 electron rule can be used to estimate the stability of a metal complex; upon having 18 valence electrons, same electron configuration as the one of inert gas' in that chemical period is achieved reflecting high stability. Perhaps understanding why the 18 electron rule does not hold for Rh is vital in explaining the differences between Co and Rh spectra.

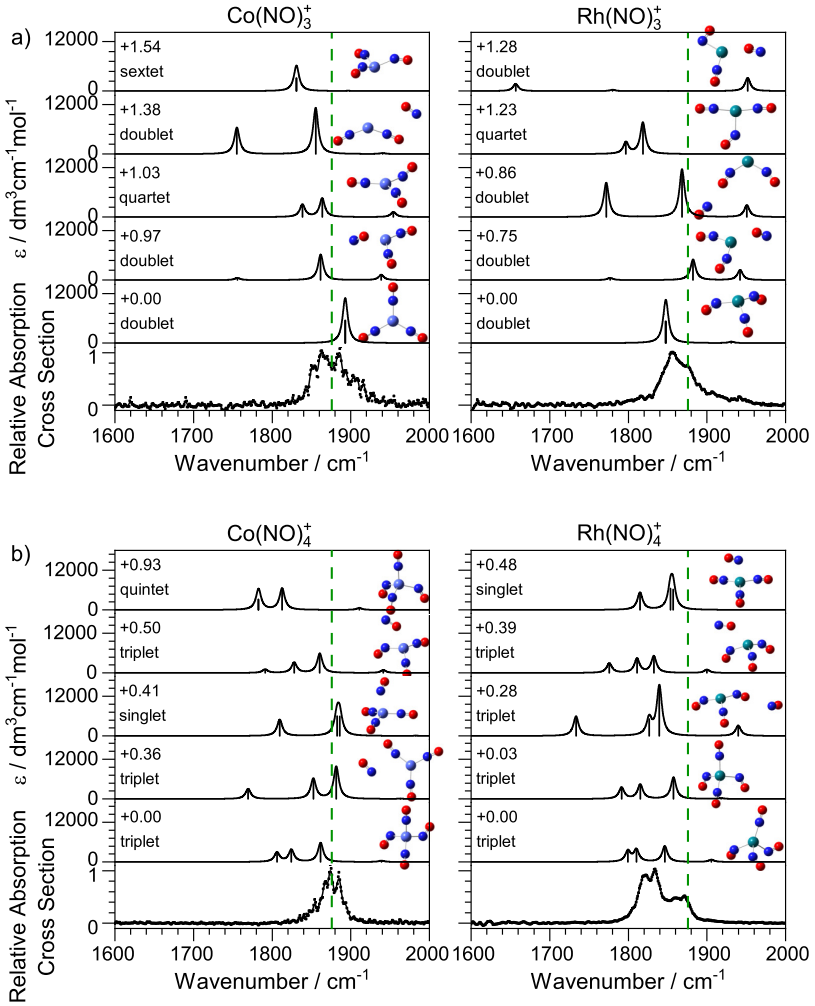

Figure 6.5.1: A comparison of the experimental and computational IR-PD spectra of energetically low-lying isomers for a) $Co(NO)_3^+$ and $Rh(NO)_3^+$; b) $Co(NO)_4^+$ and $Rh(NO)_4^+$. The green dashed line indicates the "free" NO stretch [166, 190].

For both metals, the lowest energy structure that contains one O-bound NO molecule is higher in energy by 0.97 eV and 0.75 eV, respectively, than the putative ground state, retaining its doublet multiplicity. The corresponding NO rotational barrier from N-bound to O-bound for $Co(NO)_3^+$ and $Rh(NO)_3^+$ was calculated to be 0.11 eV and 0.09 eV, respectively; it is unlikely that these isomers are trapped behind the rotational barrier and present in our molecular beam. Thus, the spectra are assigned as resulting from the calculated putative (N-bound) ground states for both metals.

The simulated energetically low-lying conformers along with their spectra of the $Me(NO)_4^+$ complexes are given in Figure 6.5.1. The putative ground state of $Co(NO)_4^+$ suitably matches the experimental spectrum recorded and involves two linear and two bent NO molecules. The coordination shell is thus 16 electrons, and perhaps the 18 electron rule cannot be satisfied completely due to steric considerations. The equivalent structure for $Rh(NO)_4^+$ is only +0.03 eV higher in energy than the lowest energy geometry (the notation of δE = +0.03 eV will be used in further text) which contains three bent NO ligands − a slightly rearranged $Rh(NO)_3^+$ core upon which linearly-bound NO adds to, resulting in 14 valence electrons. Due to the breadth and number of the peaks, it is reasonable to suppose that both of these isomers are present in the $Rh(NO)_4^+$ spectrum.

The structure with a best spectral match for $Co(NO)_5^+$ is analysed in terms of the displacement vectors in Figure 6.5.2.a). The equivalent geometry for $Rh(NO)_5^+$, albeit the NO molecules in the dimer parallel to each other, is only δE = +0.05 eV, and the vectors shown for the Co complex are representative. Overall, the experimental spectrum for $Co(NO)_5^+$ exhibits five features ($Rh(NO)_5^+$ possibly more). The vibration at 1664 cm^{-1} (in red) is perfectly located on the NO dimer with NO molecules oscillating out of phase to each other. The band at 1802 cm^{-1} (in blue) is due to linearly-bound NO molecules vibrating in phase to each other but out of phase with bent NO that is not part of the dimer. The 1845 cm^{-1} band (in green) arises from the out-of-phase movement of linearly-bound NO ligands whereas 1884 cm^{-1} is a combination band of the dimer that is in phase within but out of phase to the rest of the cluster. Finally, all five NO ligands vibrate in phase at 1942 cm^{-1}. These results confirm that the two outer "satellite" bands are due to the NO dimer but it is also important to understand why one of the bands is considerably red-shifted whereas the other one is blue-shifted.

All calculated geometries throughout this chapter give rise to combination bands in their vibrational analysis. As a result, the computed spectra are difficult to explain using the "classical" understanding of the nitrosyl activation using the

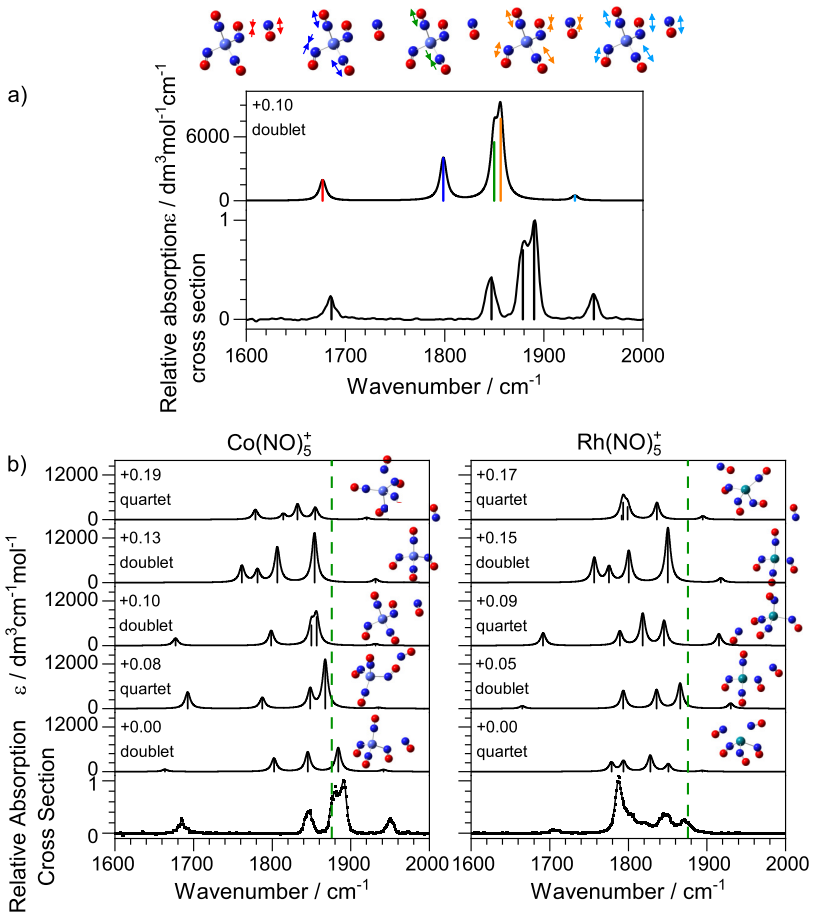

Figure 6.5.2: A comparison of the experimental and computational IR-PD spectra for a) the putative ground state structure of $Co(NO)_5^+$ with colour-coded mode vectors and b) energetically low-lying isomers for $Co(NO)_5^+$ and $Rh(NO)_5^+$.

Dewar-Chatt-Duncanson model [241, 242] and local mode picture. Nevertheless, some quantitative information can be drawn. The model states that the σ donation from the NO ligand to the metal strengthens the NO bond (making it shorter) and π back-donation from the metal to the antibonding orbital of a ligand weakens the NO bond (making it longer).

Considering the $Co(NO)_5^+$ geometry presented in Figure 6.5.2, the bond lengths were calculated as: two linearly bound NO molecules directly adsorbed to the Co atom, r(N=O) = 1.13 Å, a bent NO that is only adsorbed on the Co atom, r(N=O) = 1.14 Å, an NO in the dimer that is also coordinated to the Co atom, which for simplicity will be referred to as inner, r(N=O) = 1.15 Å, and the corresponding

outer NO in the dimer, r(N=O) = 1.12 Å. As a reference value, "free" NO calculated here has a bond length of 1.14 Å with its experimental stretch vibration at 1876 cm^{-1} [166, 190]. Thus, the three NO molecules that have bond lengths similar to the "free" NO give rise to the bands observed close to the "free" NO stretch.

The inner NO in the dimer with 1.15 Å bond length is responsible for the red-shifted band at 1664 cm^{-1} (is activated) whereas the bond of the outer dimer NO is 1.11 Å length and is strengthened − giving rise to the 1942 cm^{-1} stretch. Mulliken charges [243] calculated using DFT indicate that there is -0.03898 charge concentrated on the inner NO in the dimer and +0.304089 on the outer NO, which is consistent with the spectral shifts of the "satellite" bands observed. A quantitatively similar explanation holds true for the structures containing the dimer for the $Rh(NO)_5^+$ species.

The aforementioned trends of the relative band positions with different metals concerning the "satellite" bands in $Me(NO)_5^+$ spectra were attempted to be explained using the same idea. First of all, the experimental band position of the red-shifted "satellite" band (the band in the 1680-1720 cm^{-1} region) is larger in the Rh complex. The charges calculated on the inner NO were -0.018425 for the Rh complex (-0.03898 for the Co complex), agreeing with this tendency. Secondly, the blue-shifted "satellite" band (the band in the >1900 cm^{-1} region) has a larger frequency in the Co complex, and the charges concentrated on the outer NO were computed as +0.305313 for the Rh complex (+0.304089 for the Co complex). Whilst this result is not agreeing with the experimental trend at all, it is worthy to note that the absolute positions for this "blue satellite" band do not match very well with experimental spectra, as determined by DFT in Figure 6.5.2.b).

A representation of high stability calculated isomers for $n = 5$ for both metals is given in Figure 6.5.2.b). With regards to $Co(NO)_5^+$, the $\delta E = +0.10$ eV isomer gives rise to the spectrum that matches best the experimental results in terms of the shape of the spectrum, where the fifth NO adds to the external second solvation shell forming an antiparallel NO dimer. The second lowest energy structure for

Co contains an outer NO that seems to be physisorbed; the same binding motif was found in some calculated isomers for smaller clusters, however,the computed spectra of those geometries did not match the experimental infrared spectra. It is possible that DFT overestimates the range of weak interactions due to NO having an unpaired electron. As the energy barrier for NO rotation from the first to third lowest energy isomer is expected to be small (less than 0.10 eV), the actual observed spectrum might be some intermediate between both of these structures.

The experimental spectrum of $Rh(NO)_5^+$ is richer than that of $Co(NO)_5^+$, and could be due to the Rh complex having two low energy structures that are close in energy (0.05 eV) but give rise to different spectra. The calculated putative ground state geometry involves all nitrosyl molecules adsorbed directly on the metal centre whereas the next lowest energy structure contains the NO dimer motif for which there is evidence in the vibrational spectrum in the form of red- and blue-shifted "satellite" bands.

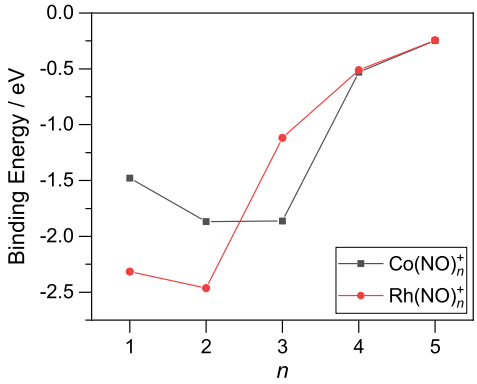

Figure 6.5.3: Calculated binding energies for the a) $Co(NO)_n^+$ (in black) and b) $Rh(NO)_n^+$ (in red) ($n = 1-5$) putative ground state complexes.

The successive NO binding energies to the putative ground state $Me(NO)_n^+$ ($n = 1-5$) geometries are plotted in Figure 6.5.3 (details in Section 2.5). An increased stability of the $Rh(NO)_2^+$ and $Co(NO)_3^+$ complexes is suggested, however, the binding energy of the additional third and fourth NO, respectively, exceeds the one photon energy. At $n = 5$, the binding energy for both metals decreases

further and approaches the single photon limit, as expected from closing of the coordination shell at $n = 4$.

Figure 6.5.4 displays the representative lowest energy isomers for $Me(NO)_6^+$. As mentioned before, the spectrum in the $Co(NO)_6^+$ case suggests a cluster with two NO dimer motifs that are not symmetric to each other giving rise to a broader than in $Co(NO)_5^+$ red-shifted "satellite" band. The lowest energy structure containing such motifs is $\delta E = +0.15$ eV. The calculated putative ground state geometry contains an antiparallel NO dimer motif, and as the corresponding structure for $Co(NO)_5^+$ was calculated to be more than 1 eV higher in energy from the assigned one, it also does not form for $n = 6$. The $\delta E = +0.07$ eV and $+0.12$ eV isomers show bands in the regions where the experimental spectrum has none; these structures may be lower in energy than the suitable $\delta E = +0.15$ eV geometry due to the introduction of erroneous DFT energies of around 0.1 eV. Another plausible explanation is that the binding interaction of sixth NO to the already outer NO on the $n = 5$ cluster is overestimated and no such trimer motifs form. The $\delta E \geqslant +0.15$ eV isomers are all suitable candidates to explain the vibrational spectrum, and might coexist as well.

The $Rh(NO)_6^+$ spectrum is once again richer than the Co counterpart. Similarly to $n = 5$, the putative ground state contains all NO molecules directly adsorbed to the metal centre (valence electron count 14). The $\delta E = +0.14$ eV isomer represents the addition followed by dimer formation of another NO to the putative ground state for $Rh(NO)_5^+$. There is sufficient evidence from the band positions that both of these isomers are produced.

Similar analysis of the calculated $Me(NO)_7^+$ geometries is also shown in Figure 6.5.4. Not much can be said about the Co complex experimental spectrum except that the assumed structure is not perturbed too much from $n = 6$ as the main spectral difference is better resolved bands, which could also be a consequence of the spectrum being comprised of less isomers. However, it is difficult to assign specific isomers as responsible for reproducing the experimental spectrum. The $\delta E = +0.52$ and $+0.53$ eV structures seem to match the spectrum well, however, it

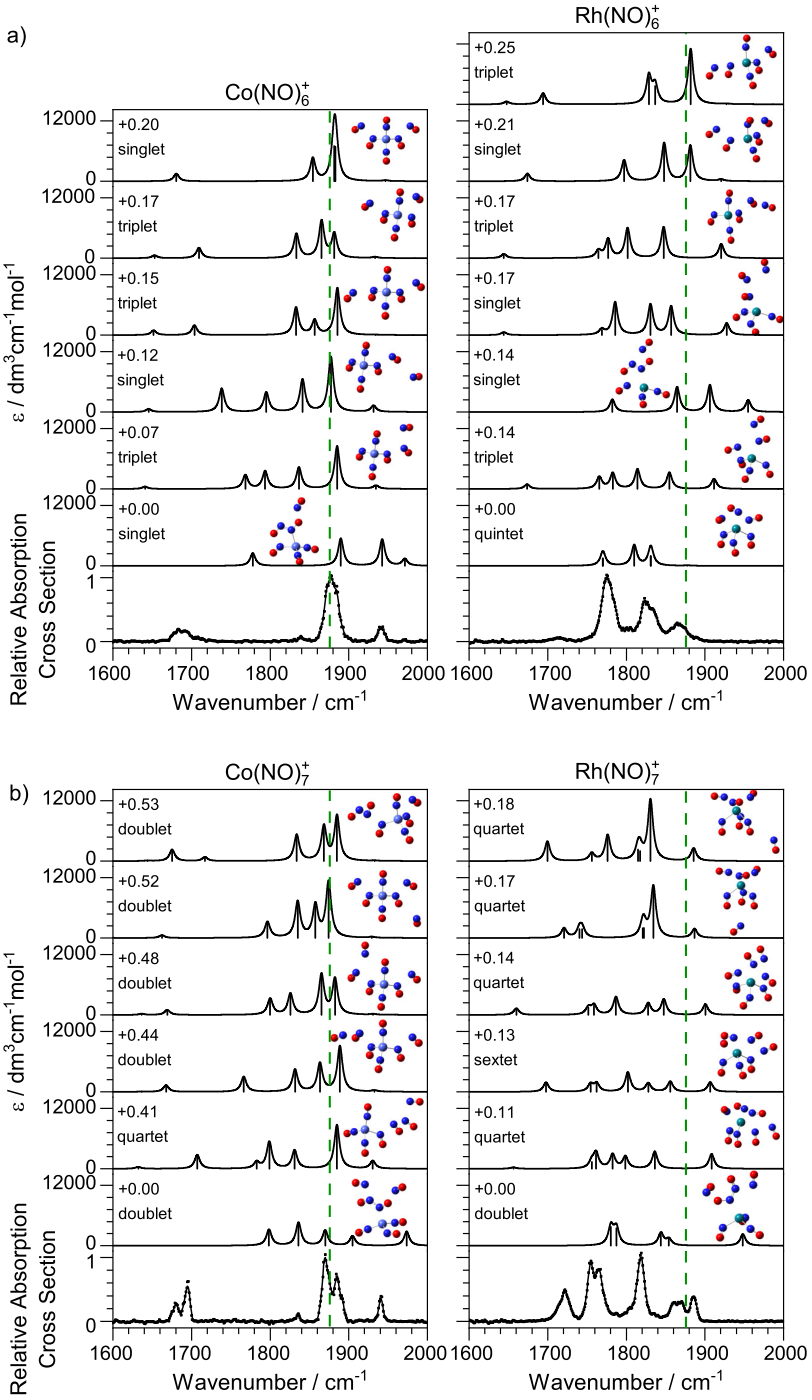

Figure 6.5.4: A comparison of the experimental and computational IR-PD spectra of energetically low-lying isomers for a) $Co(NO)_6^+$ and $Rh(NO)_6^+$; b) $Co(NO)_7^+$ and $Rh(NO)_7^+$. The green dashed line indicates the "free" NO stretch [166, 190].

is not clear why the δE = +0.53 eV isomer would preferably form. From similar calculated structures, the δE = +0.52 conformer appears to be an exclusive match with the spectrum, *i.e.* if seventh NO binds anywhere else in the cluster in a loose way, the spectrum is perturbed and looks different. The δE $\leqslant$ 0.52 eV isomers are ruled out due to the same reasons as in the $Co(NO)_6^+$ case.

Regarding $Rh(NO)_7^+$, it is clear that the "satellite" bands are much more intense than for $n < 7$, and the fact that the lowest energy isomer no longer has all NO molecules adsorbed to the Rh atom, but contains the dimer motif, is encouraging. The putative ground state is ruled out, with similar reasoning that such corresponding structure is not seen in the low-lying calculated structures for $n < 7$, and the three structures that accommodate the dimer are feasible and might coexist.

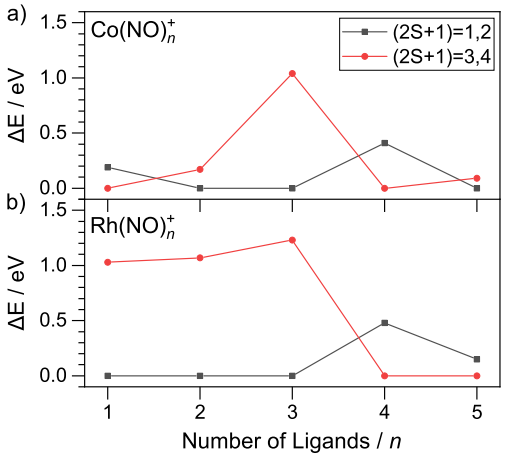

Figure 6.5.5: Calculated energies of the lowest energy isomers for a) $Co(NO)_n^+$ and b) $Rh(NO)_n^+$ (n = 1–5); in black for the lowest spin state (singlet and doublet for even and odd n, respectively) and in red for higher spin state (triplet and quartet for even and odd n, respectively).

To better understand the variation in the coordination number between Co^+ and Rh^+ centres, the computationally assigned structures with different spin states are compared in Figure 6.5.5. The spin crossover from lowest to higher multiplicity occurs at n = 4 (to triplet) for both metals and then for n = 5 remains as higher (quartet) for Rh but again, crossing over to the lowest multiplicity for Co (doublet).

The assigned $n = 5$ structure for Co contains the dimer motif and thus it is probable that this extra unpaired electron that is preferred by the $n = 5$ putative ground state for Rh (all NO molecules directly adsorbed to the metal centre) is involved in the bonding in the dimer for $Co(NO)_5^+$. The multiplicity of the putative ground state for $n = 6$ for Rh increases further to a quintet with the structure that is a little higher in energy with the dimer motif having a quartet spin state, just as the one assigned for $n = 7$ that also contains the dimer, agreeing with the observation made before.

Interestingly, for both metals the closing of the coordination shell is signified by the spin crossover to the higher multiplicity. Cunningham *et al.* [105] found that for the $Rh(N_2O)_n^+$ system the closing of the first solvation shell at $n = 4$ was accompanied by the calculated preferred spin change from triplet (for $n = 3$) to singlet. In our work here, the converse is true, and this could be an influence of N_2O being a weak field ligand whereas NO is a strong field ligand or radical nature of NO whilst N_2O has a closed electronic shell. An IR-PD study by Ricks *et al.* [29] regarding the $Co(CO)_n^+$ clusters, also observed the signature for the coordination shell closing − a calculated preferred spin crossover from triplet ($n = 4$) to singlet ($n = 5$). Since CO is a strong field ligand, this suggests that the radical nature of NO might be the key factor here.

Another important finding was made by Duncan and coworkers [29, 239]: $Co(CO)_5^+$ has a completed coordination sphere obeying the 18 electron rule whereas $Rh(NO)_4^+$ was determined to be the most stable (16 valence electrons) reflecting the behaviour of Rh nitrosyl clusters. To some extent, the nitrosyl system mimics the carbonyl system findings with Rh preferring lower coordination than Co.

An additional loss channel was observed for the $Me(NO)_n^+$ ($n = 6, 7$) species, namely -2NO visualised in red in Figure 6.5.6. Interestingly, -2NO loss shows a different spectrum than the -NO channel such that the red- and blue-shifted signature bands ascribed to the dimer are absent. In these "signature" bands, once a first photon is absorbed, a ligand from the outer coordination shell is lost, and

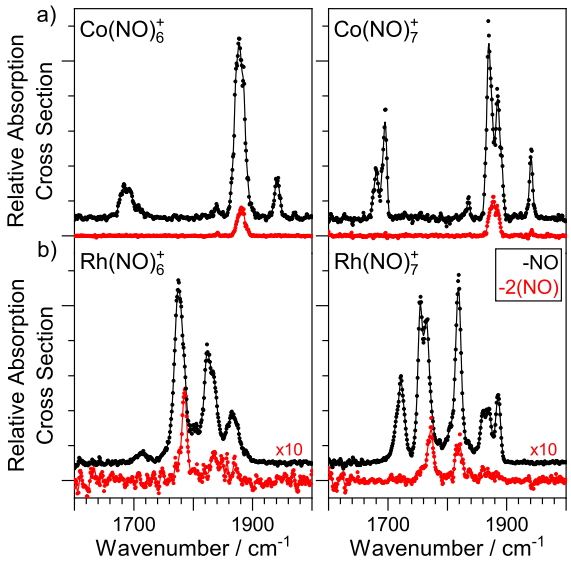

Figure 6.5.6: IR-PD spectra recorded in the loss channels of -NO (in black) and -2NO (in red) for the a) $Co(NO)_6^+$ and $Co(NO)_7^+$; b) $Rh(NO)_6^+$ and $Rh(NO)_7^+$) complexes plotted as relative absorption cross sections in each panel. Some spectra are enlarged by ten times, as indicated.

with it, crucially, the chromophore itself. As a result, no subsequent photon can be absorbed at the same wavenumber to remove a second ligand. These results strongly suggest that the dimer $(NO)_2$ moiety itself is not lost as an intact entity but rather that the -2NO channel comprises two sequential single loss processes. By contrast, the more central IR modes, which do not involve motion of the dimer (Figure 6.5.2.a)), can absorb more than one photon leading to the loss of two ligands. In this way, differences in the spectra recorded in different fragment mass channels provide exquisite detail on the nature of the vibrational mode excited.

6.6 IR-PD Spectra of Pure NO Clusters: $(NO)_n^+$ and $NO_2(NO)_m^+$ (n = 3–8, m = 2–9)

Prior to performing the experiments for $Co(NO)_n^+$ and $Rh(NO)_n^+$ systems, the IR-PD spectra of the $(NO)_n^+$ and $NO_2(NO)_n^+$ complexes were recorded. The original intention was to compare the results with Stace and coworkers [226, 227], and in this way to confirm that the IR laser wavenumber calibration is correct. The spectra,

however, proved to be significantly different, even though the laser calibration was validated with another system scanned previously.

The current working hypothesis is that due to different experimental conditions, different isomeric distributions are present in the resulting molecular beams. In the Stace and coworkers [226, 227] studies, neutral clusters are produced, which are then ionised with high energy (70 eV) electrons. Such conditions might allow the $(NO)_n^+$ complexes to assume higher energy conformers accessed in the Franck-Condon region from the neutral $(NO)_n$ surface. In the experiments presented in this chapter, charged complexes are produced *via* laser ablation of metal target prior to complexation, and the complexes are expected to be approximately thermalised. The formation of clusters can be summarised as:

Stace: NO + NO + ... $\Rightarrow$ $(NO)_n$ –EI-> $(NO)_n^+$;

Ours: NO^+ + NO + NO $\Rightarrow$ $(NO)_n^+$.

The theoretical calculations with emphasis on possible different isomeric forms within these experimental conditions are being conducted at the moment.

6.6.1 Time-of-Flight Spectrum

A representative time-of-flight mass spectrum of nitrosyl clusters and their NO_2 counterpart produced in the plasma upon ablation of a metal target is given in Figure 6.6.1. The spectrum is dominated by progressions of the $(NO)_n^+$ and $NO_2(NO)_n^+$ species with very little reactivity observed besides complexation. As NO is a radical, odd-even n alternation in the amount produced of the $(NO)_n^+$ and $NO_2(NO)_n^+$ complexes is expected. In this case, it is visible but not as pronounced as in other studies [178–180].

A small amount of oxygen-rich species are produced, *e.g.* $O_4(NO)_2^+$ and $O_3(NO)_3^+$, which presumably form due to reactions between the NO molecules with eventual release of N_2. Additionally, little N_2O complexation to the nitrosyl clusters is also observed – DFT calculations indicated that the '$N_2O\cdots NO_2$' moiety is thermodynamically more stable than the '$(NO)_3$' complex. However, the associated

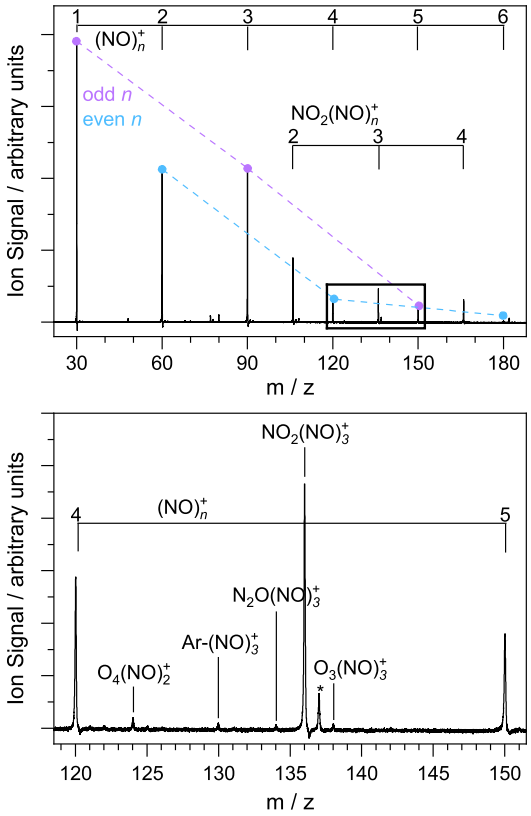

Figure 6.6.1: Time-of-flight mass spectrum of $(NO)_n^+$ clusters and their NO_2 counterpart produced in the reaction channel while ablating the Co target; formation of these clusters is not an intrinsic property of a metal but the formation efficiency does depend on the work function of a metal. Odd and even n peaks are indicated by light purple and blue colours, respectively. An enlarged mass region between $n = 4$ and 5 is shown in the bottom panel.

kinetic barriers probably are large and the amount formed is reflective of that. Some Ar-tagged species are also present but not enough to record the IR-PD spectra of.

6.6.2 IR-PD Spectra

The recorded IR-PD spectra of the $(NO)_n^+$ ($n = 3$–8) species are shown as normalised cross sections in Figure 6.6.2. For $n = 3$, there are two unresolved broad bands centred around 1610 cm^{-1} and 1720 cm^{-1} – suggesting that depletion is a multiple photon process and there is associated stability with these species. Dissociating the $n = 2$ species was not possible, presumably because of high binding energy (0.59 eV [244]).

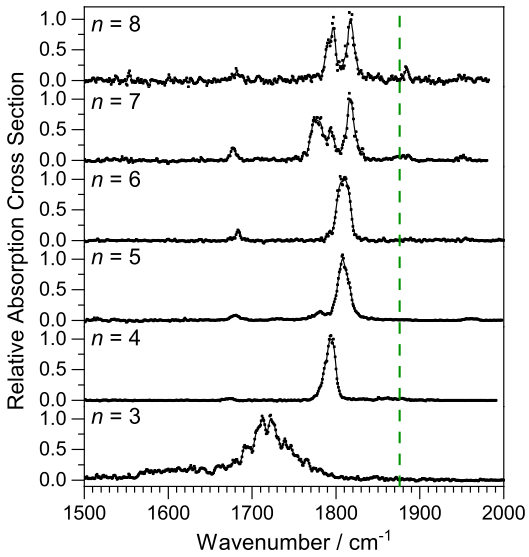

Figure 6.6.2: IR-PD spectra of $(NO)_n^+$ ($n = 3-8$) clusters presented as relative absorption cross sections and normalised to 1 for each n. The green dashed line indicates the "free" NO stretch [166, 190].

For $n = 4$, a relatively well-resolved peak emerges accompanied by a weaker "satellite" peak at *ca.* 1670 cm^{-1} that stays at the same position throughout $n = 4-8$. This is reminiscent of the $Co(NO)_n^+$ and $Rh(NO)_n^+$ systems (6.4.2), where red- and blue-shifted "satellite" bands are observed for $n = 5-7$. Perhaps here, due to lower signal-to-noise ratio, such blue-shifted "satellite" band is not as apparent, but there is some evidence for it in the spectrum of $n = 5-8$. For $n = 5$, the main band shifts to the blue slightly and a small peak to its left appears. Another band at *ca.* 1730 cm^{-1} emerges but is not very intense (can be seen in the enlarged version of the IR-PD spectra in Figure 6.6.5). Since the spectrum for the $(NO)_5^+$ species proved to be recorded most sensitively, it can be concluded that even if such a band exists for other n, it would be hard to observe. For $n = 6$, the main band stays at the same position, however, at $n = 7$, it splits into seemingly three bands which then merge into two narrower peaks at $n = 8$.

Figure 6.6.3 shows the $(NO)_n^+$ ($n = 3-5, 7$) IR-PD spectra recorded by Stace and coworkers [226, 227]. For $n = 3$, the band is centred at *ca.* 1780 cm^{-1} whereas in our work at *ca.* 1720 cm^{-1}. For $n = 4$, Stace and coworkers observe the band red-shifted

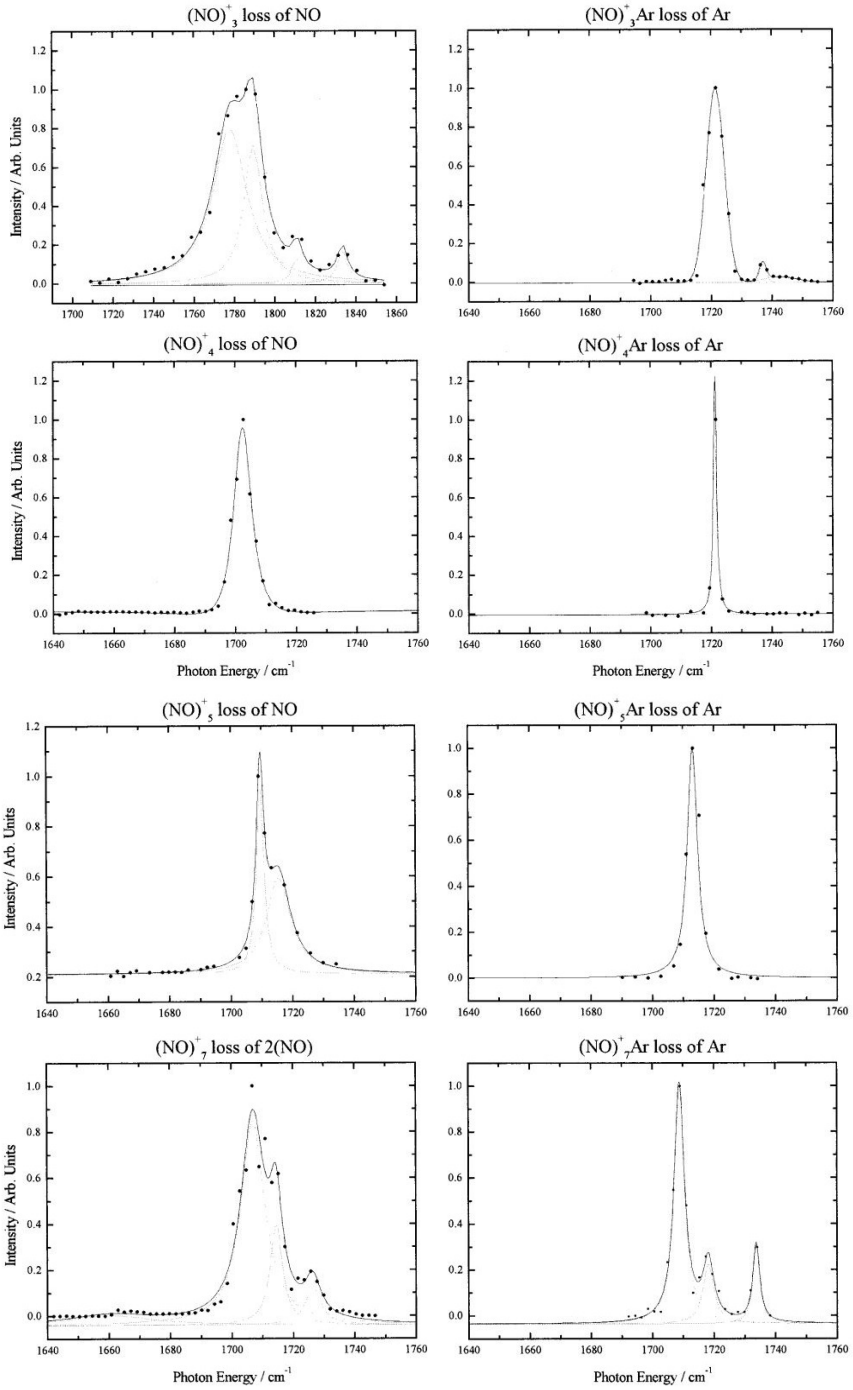

Figure 6.6.3: IR-PD spectra of $(NO)_n^+$ (n = 3–5, 7) clusters as well as their Ar-tagged counterparts. Reprinted from [226] (https://doi.org/10.1063/1.480283), with the permission of AIP Publishing.

by *ca.* 80 cm^{-1}; here, it blue-shifts by approximately the same amount. In both studies, for $n \geqslant 5$, the position of the most intense band does not change by much.

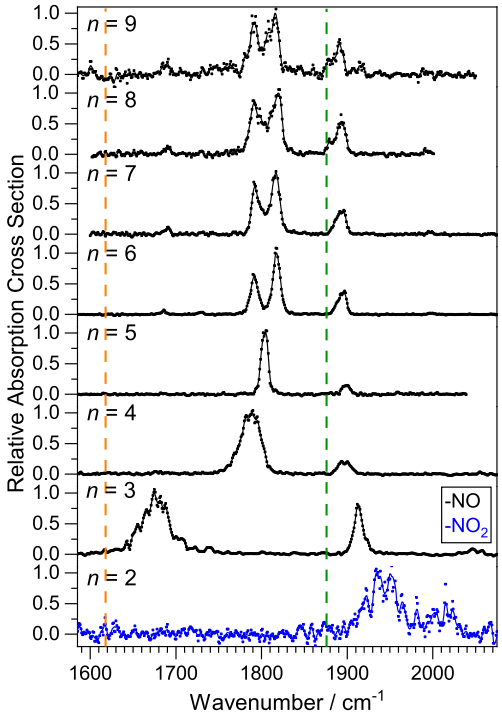

Figure 6.6.4: IR-PD spectra of $NO_2(NO)_n^+$ ($n = 2-9$) clusters presented as relative absorption cross sections and normalised to 1 for each n. The spectra recorded in the loss channels of -NO and -NO_2 are plotted in black and blue, respectively. The green and orange dashed lines indicate the "free" NO and NO_2 stretches, respectively [125, 166, 190].

The recorded IR-PD spectra of the $NO_2(NO)_n^+$ ($n = 2-9$) species in terms of normalised absorption cross section is shown in Figure 6.6.2. The spectrum for $n = 2$ is noisy (suggesting it is a multiple photon process) and, in contrast to other n, is recorded in the loss of the NO_2 moiety, which indicates enhanced stability of the $(NO)_2^+$ complex. Such different loss channels between $n = 2$ and 3 might also suggest that the 'NO_2' moiety within these species is found in the core, and with n is buried even deeper and is not available for dissociation.

For $n = 3$, the spectrum seemingly comprises two main bands that remain as such for $n = 4$ and 5 and evolve into three at $n = 6-9$. Throughout n, there is evidence for red- and blue-shifted "satellite" bands but the spectrum is not well-resolved enough to draw any conclusions about them.

6.6.3 Fragmentation Pathways

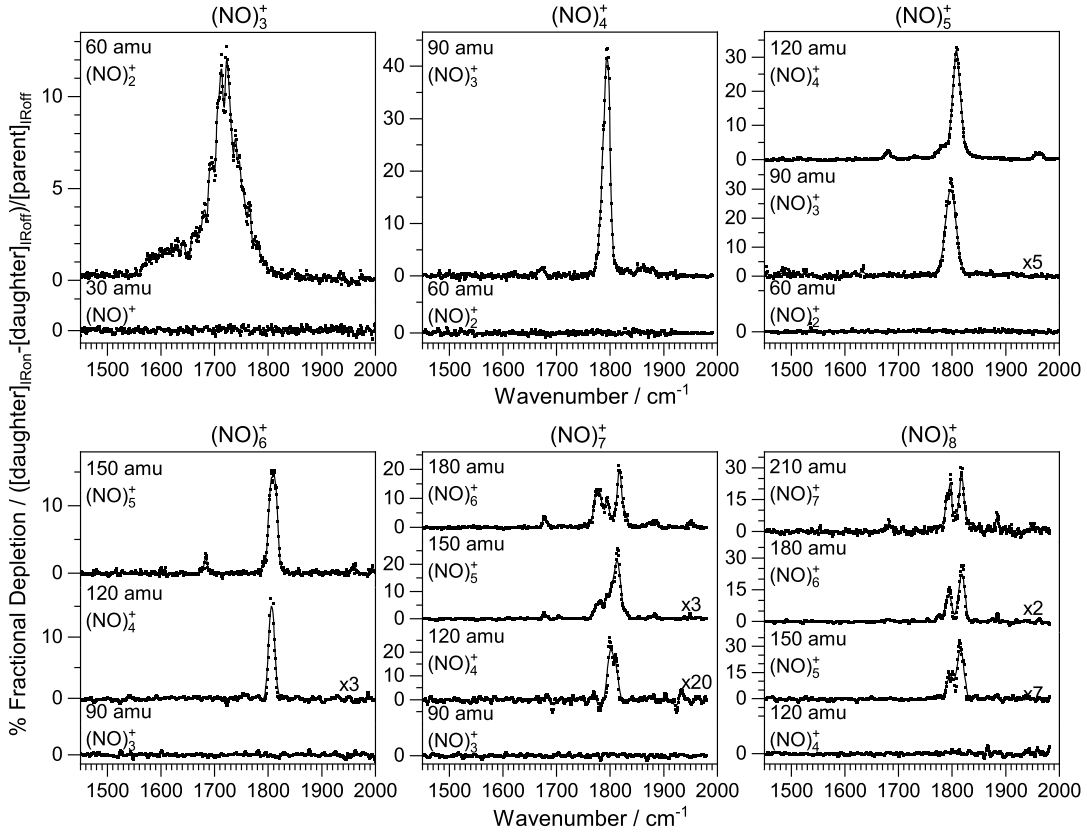

Figure 6.6.5: IR-PD spectra of $(NO)_n^+$ (n = 3–8) clusters presented as fractional depletion and recorded in multiple NO loss channels. In each panel, the label on left hand side indicates the mass and anticipated chemical formula of daughter fragments in which the spectra were recorded. The spectra in some cases are enlarged, as indicated.

The IR-PD spectra recorded in the available loss channels for the $(NO)_n^+$ (n = 3–8) species (plotted as a fractional depletion in Figure 6.6.5) for n = 3 and 4 show one NO molecule loss; for n = 5 2NO loss, which suggests an increased stability of the $(NO)_3^+$ complex. It is the smallest cluster available for electron pairing and its stability is also noted in other publications [180, 229, 231].

The dissociation pathways shown for the $NO_2(NO)_n^+$ (n = 4–9) species in Figure 6.6.6 show more than two NO loss upon IR irradiation for the n = 6–9 species (sole NO loss spectra for n = 2 and 3 are not included). Comparison of the spectra in observed loss channels show differences in the number and the relative heights of the bands, however, any further analysis needs to be based on theoretical simulations.

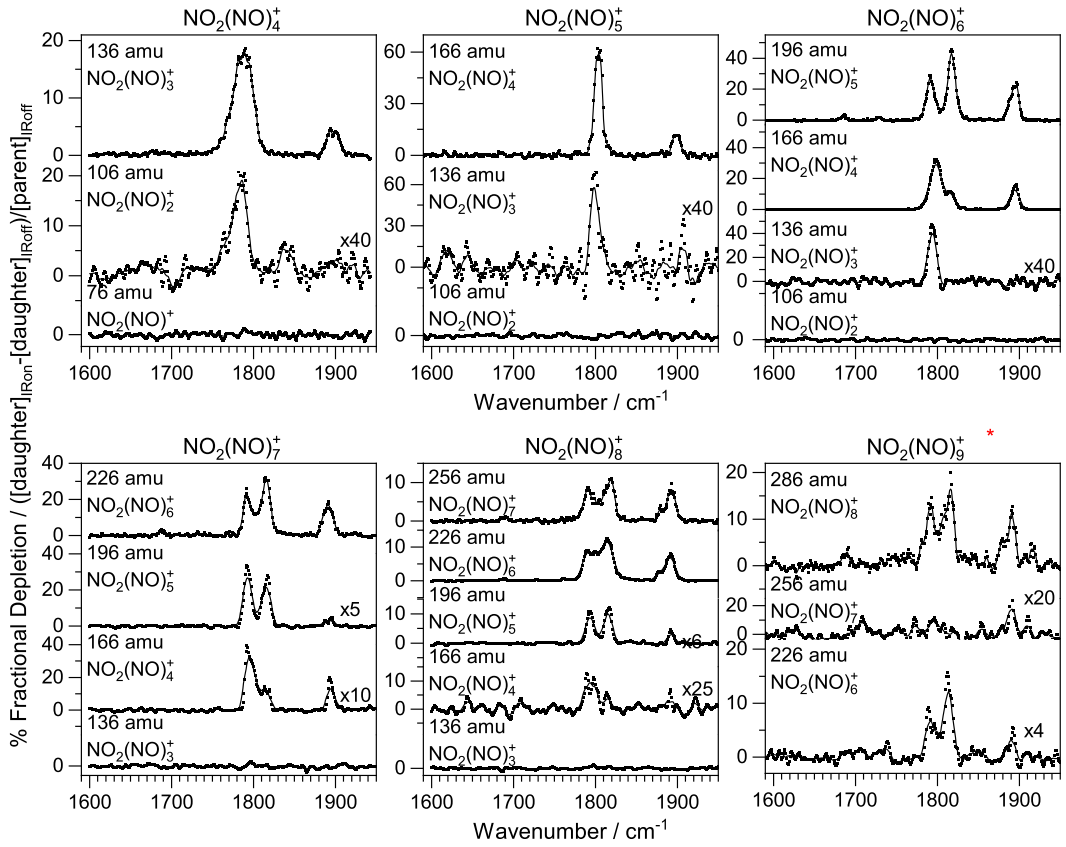

Figure 6.6.6: IR-PD spectra of $NO_2(NO)_n^+$ ($n = 4-9$) clusters presented as fractional depletion and recorded in multiple NO loss channels. In each panel, the label on left hand side indicates the mass and anticipated chemical formula of daughter fragments in which the spectra were recorded. The spectra in some cases are enlarged, as indicated. Red asterisk signifies that spectra in not all loss channels were recorded for the $NO_2(NO)_9^+$ species.

6.7 Summary and Conclusions

In summary, the IR spectra of $Co(NO)_n^+$ and $Rh(NO)_n^+$ ($n = 3-7$) clusters have been recorded in the NO stretch region. Red- (1680-1720 cm^{-1}) and blue-shifted (>1900 cm^{-1}) "satellite" bands characteristic of the NO dimer formation emerge for the $n \geqslant 5$ species. The spectral differences of both metals can to some extent be explained in terms of different coordination numbers ($n = 4$ for Co and $n = 6$ for Rh) as well as multiple coexisting isomers for rhodium nitrosyls.

Additionally, the IR spectra of unligated $(NO)_n^+$ ($n = 3-8$) as well as the $NO_2(NO)_n^+$ ($n = 2-9$) complexes were recorded in the NO stretch region. The

spectra for $(NO)_n^+$ clusters proved to be very different than Stace and coworkers [226, 227] results and different experimental conditions might be the key here. Ongoing DFT calculations will be completed for this reason focusing on the possibility of producing different isomers that give rise to different spectra.

It is important to re-emphasise here the limitations of DFT in determining the structures of complexes involving multiple open shell ligands. Theoretical calculations need to be improved by employing multi-reference methods such as MRMP2 including the complete basis set (CBS) limit [245] due to the NO molecule possessing an unpaired electron. However, such calculations are especially costly, and perhaps that is the reason there is a lack of higher than DFT level computational work involving optimisations of larger than dimer nitrosyl clusters.

Chapter 7

Energy Flow in Mixed Ligand Complexes: $Rh(CO)_n(N_2O)_m^+$ ($n = 1{-}5$, $m = 1{-}4$)

Mixed ligand O_2 and CO interactions and cooperative binding effects on the Au_n^- metal complexes were explored in Chapter 5. Here, similar ideas can be applied albeit for increasing numbers of adsorbates on a single Rh^+ metal centre. The system chosen is appropriate for comparison with analogous $Au(CO)_n(N_2O)_m^+$ experiments which we have published as Green *et al.* [62, 236], and the results presented in this chapter are being prepared for publication. It is the second study of such type in the Mackenzie group laboratory, and hopefully will encourage further exploration of the mixed-ligand single metal complexes.

Studying mixed ligand adsorption on metal centres provides a unique opportunity to explore the energy flow effects. The investigation of the $Rh(CO)_n(N_2O)_m^+$ system *via* IR-MPD spectroscopy and DFT calculations was inspired by surprising findings in the $Au(CO)_n(N_2O)_m^+$ study [62, 236], where provided the loss channel is energetically accessible (incoming IR photon is equal or greater in energy than the binding energy (BE) of the eliminated group + internal energy (IE) of the complex), the stronger bound ligand (CO) was observed to leave more efficiently, which is atypical on the basis of the Rice-Ramsperger-Kassel (RRK) theory [246–248]. According to the theory, it is much more likely for the required amount of BE + IE for dissociation to become localised at the weaker bond (in this case,

Au$\cdots$$N_2O$). Moreover, the efficiency of (CO, N_2O) moiety loss was larger when the IR photon was absorbed at the N_2O moiety than at the CO. The results of the $Au(CO)_n(N_2O)_m^+$ study are discussed in more detail in Chapter 8.

In this chapter, the spectra of $Rh(CO)_n(N_2O)_m^+$ ($n = 1-5$, $m = 1-4$) complexes reveal signature bands for the core N_2O binding motifs (O- and N-bound), and with combined DFT calculations disclose a coordination number of four, irrespective of the nature of ligands involved. The spectra are compared with the results of the similar gold system and explained in terms of different coordination numbers and electronic configurations of these metal centres.

The experiments and analysis in this chapter were performed by me using the instrument in Oxford with computational help from project students Rachael Brown, Matthew Doll, and Thomas Bithell under my supervision.

7.1 Introduction

As noted in Chapters 3 and 5, both CO and N_2O gases are detrimental to the environment as well as the human system. Naturally, there is interest in studying systems where more than one type of atmospheric gas ligands are adsorbed on the metal centre with a hope that the impact of both gases can be reduced simultaneously by inducing reactions that produce less harmful substances. Most famously, this idea is applied in the automobile three-way catalytic converter [249] described previously in Section 6.1, but is also explored in research studies, e.g. CO oxidation to CO_2 by N_2O catalyzed by the ruthenium hydride pincer complexes [250]. Full catalytic cycles are even achievable on single metal atoms; the first such cycle of CO oxidation and N_2O reduction was observed by Kappes and Staley in the ICR spectrometer for Fe^+ [251]. A suite of studies have been performed regarding the kinetics and mechanism of the reaction between N_2O and CO on a supported rhodium catalyst [252–254].

Blagojevic *et al.* [255] explored the Rh^+ catalytic ability in reducing N_2O and oxidising CO by ICP/SIFT tandem mass spectrometer and found that even though Rh^+ is thermodynamically able to transport the O atom, it reacts too slowly

to complete the catalytic cycle at room temperature, and Rondinelli *et al.* [256] confirmed these results by DFT calculations.

The binding of N_2O to small cationic gas-phase rhodium complexes has been described in Section 3.1. Regarding CO binding to rhodium clusters, Fielicke and coworkers measured the IR-MPD spectra of $Rh_nCO^{+/0/-}$ (n = 3−15) [115] and $Rh_n(CO)_m^{+/0}$ (n = 1−6, m = saturation limit) [257] systems, where the CO binding mode and site were found to be strongly dependent on the cluster size and its charge state. In the [115] study, for all charge states, preferential atop CO binding was observed for $n \geqslant 5$, in addition to the Rh_4CO^- cluster. In the $Rh_4CO^{+/0}$ and Rh_3CO^+ species, CO was found to bind at a three-fold hollow and two-fold sites in a bridging fashion, respectively. In the saturation limit study [257], the authors concluded that upon removing an electron from the $Rh_n(CO)_m^+$ complexes, CO molecules bound in a bridging way were essentially destabilised, which led to rearrangement into atop-bound carbonyls. The preferred mode of a ligand binding is associated with the binding site's electron density, however, different systems behave differently upon changing the electron density [257].

Relevant here, the IR-PD spectra of $Rh(CO)_n$-Ar^+ and $Rh(N_2O)_n$-Ar^+ complexes were recorded by Brathwaite *et al.* [239] and Cunningham *et al.* [105], respectively. In the Brathwaite *et al.* [239] study, a full coordination shell of four CO molecules was determined in addition to a special axial binding site for the fifth CO that forms a second solvation shell with the Rh^+ atom. The spectra for n = 1 and 4−7 complexes show bands that are blue-shifted, and the spectra of n = 2 and 3 complexes consist of one red-shifted and one blue-shifted band relative to the "free" CO stretch. The authors ascribed this behaviour of cationic rhodium carbonyls as "non-classical" due to the electrostatic polarisation effects being prominent and inefficient π^* back-bonding resulting in such blue shifts.

In a CO molecule, the orbitals are polarised towards the O atom, but if placed in an electrostatic field, such as in proximity to a positively charged Rh^+, and binding to this metal centre *via* the C atom, the polarisation is expected to change

to the opposite direction increasing the covalency of the molecule as well as the stretching force constant. "Non-classical" behaviour is observed for the late metal carbonyls due to their filled *d* electron shells [158].

A coordination shell of four N_2O adsorbates was determined by Cunningham *et al.* [105] marked by a switch of the calculated putative ground state multiplicity from the triplet to singlet, assuming square planar geometry favoured by low-spin d^8 complexes. In the $Rh(N_2O)_{3,4}$-Ar^+ complexes, additional spectral bands due to the existence of low-lying excited states were found (within +0.63 eV of the putative ground state), unlike similar systems examined [104].

Concerning single metal mixed ligand IR-PD studies, Barwa *et al.* performed IR-MPD studies in an FT-ICR instrument on $CoCO_2(H_2O)_n^-$ [258] and $MgCO_2(H_2O)_n^+$ [259] systems, where they explored the role of water in CO_2 activation. In the former study they found that even upon ligation with one H_2O molecule the Co metal atom already inserted in the C=O bond unlike in the non-ligated counterpart [260]. Moreover, the water molecule was also found to be dissociatively adsorbed. In the latter study, for $n \geqslant 3$, a CO_2 molecule was found to be activated *via* the charge transfer producing the Mg^{2+} ion.

An IR-PD study of the $Li(CH_4)Ar_n^+$ complexes by Rodriguez *et al.* [261] observed interesting energy flow effects within the $Li(CH_4)Ar_6^+$ system. Different spectra were obtained depending on the leaving group (CH_4 or 3xAr) − effects attributed to two different isomers being present, with either CH_4 or Ar molecule being in the outer solvation shell. The energy, however, in both cases was injected at the CH_4 moiety. IR-PD spectra of the $Li(H_2O)_{3-4}Ar^+$ complexes were also recorded by Rodriguez *et al.* [262], where isomer selective fragmentation for the $Li(H_2O)_4Ar^+$ species was observed, again, depending on the daughter channel scanned. The spectroscopic studies on mixed-ligand systems are scarce but can show interesting and unexpected results, even with using a ligand that is normally considered a tag (in this case, Ar).

7.2 Experimental and Computational Methods

The time-of-flight and IR-PD spectra were recorded in the Mackenzie group laboratory in Oxford. The experimental setup has been described in detail in the publication by Iskra *et al.* [235] with recent modifications to include the mass selection of ions via the quadrupole reported by Green *et al.* [62, 236]. In this thesis, Section 2.3 contains the full description of the instrument, and only a brief one is given here.

A rotating disc target of Rh is ablated by an Nd:YAG laser (532 nm, 10 Hz). Ablated atoms cool and cluster by colliding with either 1% or 3% CO, corresponding to the N_2O-rich and CO-rich complexes produced, respectively, and 5% N_2O entrained in Ar in the reaction channel. The resulting gas mix, now entrained with a range of metal-ligated as well as non-metal-ligated complexes, is expanded into the vacuum forming a molecular beam which is then skimmed and mass-selected in the QMF/QMB assembly before the extraction region of a reflectron ToF mass spectrometer in cationic detection mode. The experiment is run at room temperature, however, the actual temperature of the molecular beam is not easily determined, as it is highly dependent on how well the complexes are thermalised in the reaction channel and/or cool in the expansion.

In order to record the IR-PD spectra, the cluster beam is subjected to alternate pulses of IR off/IR on from the tunable table top optical OPO/OPA system operating in the 2000-2400 cm^{-1} range. The resulting depletion of the parent ion and any enhancement of the daughter(s) channels are recorded as a function of wavenumber. The information on the infrared active modes as well as the branching ratios of the parent complexes are produced, and can be readily compared with the results of DFT simulations.

Energetically low-lying structures and any relevant transition states connecting them have been calculated at the def2TZVP [76, 77]/B3PW91 [263, 264]/GD3-BJ [123] level using Gaussian 16 software package [118]. The results were also tested by the def2TZVP [76, 77]/B3P86 [237, 238] basis set/functional combination that

proved to provide reliable results in similar studies by the Mackenzie group in the past [62, 104, 105, 235, 236]. To provide a better match with experimental data, computed harmonic vibrational frequencies were scaled by a factor of 0.96467 and 0.93334, determined by calculating the vibrational frequency of the "free" CO and N=N in the "free" N_2O stretches [125, 166], respectively. The computed infrared bands were convoluted with FWHM = 8 cm^{-1} Lorentzian shape curves and any experimental reported wavenumber numerical values have an error of ± 10 cm^{-1}. All energies reported here are given relative to zero-point and additionally to lowest energy molecularly adsorbed structure energies. Potential energy profiles were generated by identifying plausible transition states between two minima and performing IRC [126, 127] calculations in order to verify the correct path.

7.3 Time-of-Flight Spectrum

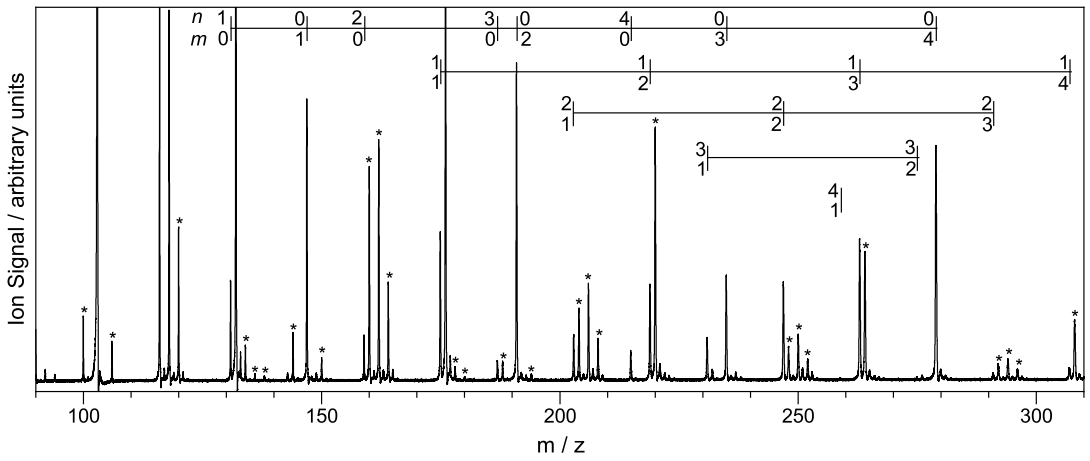

Figure 7.3.1: Time-of-flight mass spectrum of $Rh(CO)_n(N_2O)_m^+$ produced by laser ablation of Rh target in presence of 1% CO and 5% N_2O gas diluted in Ar pulsed at 6 bar. Peaks with an asterisk have an even mass − they originate from the reactions between CO and N_2O and do not contain Rh atoms.

A representative time-of-flight mass spectrum is shown in Figure 7.3.1 with a dominating distribution of $Rh(CO)_n(N_2O)_m^+$ products. From these peaks, whenever the sum of the number of different ligands adsorbed is 4 ($n + m = 4$), there is

Chapter 7. Energy Flow in Mixed Ligand Complexes $Rh(CO)_n(N_2O)_m^+$
(n = 1–5, m = 1–4)

an increase in their intensity – an indication of the coordination number being four. However, different ion transfer optimisation conditions can lead to different focusing in the mass spectrum, and spectroscopy with DFT calculations need to be considered before assigning the coordination number.

Little reactivity besides the CO/N_2O adsorption is observed for the metal-ligated species and only a small amount of rhodium oxides is produced. There is extensive evidence for various combinations of CO and N_2O complexes produced in the reaction channel that are not adsorbed on the metal atom. These reactions are not intrinsic to a specific metal, however, they do depend to some extent on the work function of the metal. In this case, such high intensity peaks are most likely due to using high energy laser pulses for the metal ablation in the experiment.

Throughout this chapter, for simplicity, a notation of CnNm will be used. It will denote singly charged rhodium-ligated species of n molecules of CO and m of N_2O. For example, a different gas mix of 3% CO and 5% N_2O was used in order to produce enough C4N1 ($Rh(CO)_4(N_2O)^+$) and C5N1 ($Rh(CO)_5(N_2O)^+$) species to perform the spectroscopy on.

7.4 IR-PD Spectra

All recorded IR-PD spectra of the mixed ligand Rh-ligated complexes are given in Figure 7.4.1. To explore the trends, spectra have been plotted with increasing n (the number of CO ligands) in the y-axis and increasing m (the number of N_2O ligands) in the x-axis.

First of all, the breadth of the observed infrared bands is considered. There seems to be a distinct point where the bands become much narrower and well-resolved, precisely when $n + m > 4$. A broad spectral bandwidth is indicative of multiple photon absorption taking place and suggests that the adsorbed ligands have relatively high binding energies which are too large to observe their dissociation from the metal atom upon absorption of a single photon. This is in agreement with the results seen in Section 7.3, where the coordination number of four ligands

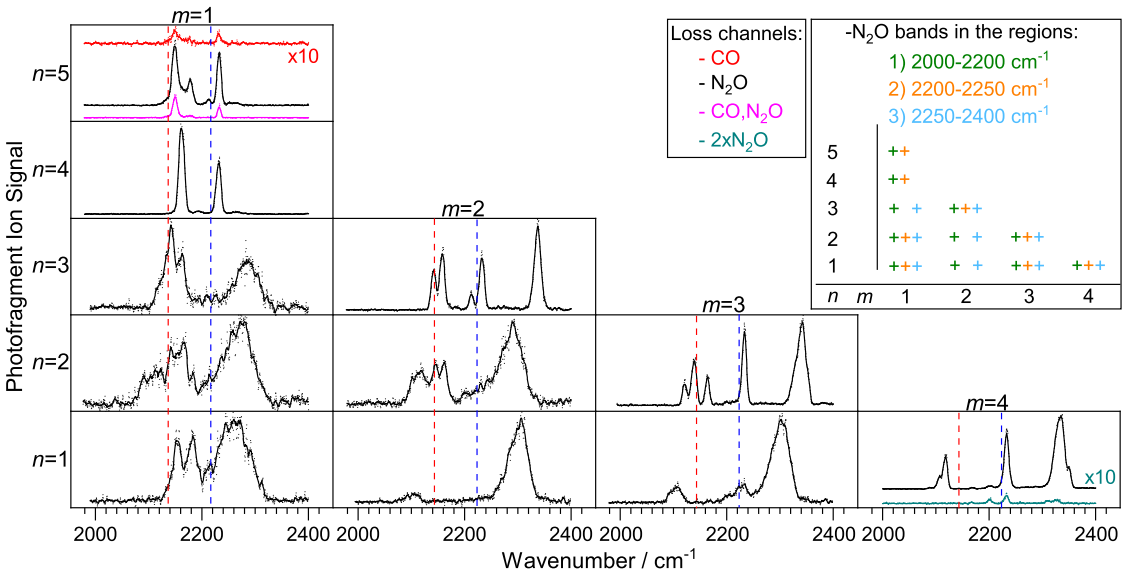

Figure 7.4.1: IR-PD spectra of the $Rh(CO)_n(N_2O)_m^+$ ($n = 1-5$, $m = 1-4$) species presented as the absolute difference in enhancement signal for all observed daughter channels. The dashed red and blue lines denote the "free" CO (2143.2 cm^{-1}) [166] and N=N in the "free" N_2O (2223.5 cm^{-1}) [125] stretches, respectively. In some cases, the spectra are enlarged by ten times, as indicated.

was suggested, and this number does not seem to depend on the composition of the ligands in the coordination sphere.

Secondly, the dominating, and in many cases the sole, loss channel for all species is N_2O loss, even for the CO-rich complexes. In two instances, additional depletion channels are observed: the C5N1 species undergo CO as well as combined (CO, N_2O) loss and the C1N4 complexes show $2xN_2O$ loss – consistent with these ligands being in the outer sphere. The spectra in additional and main channels are notably different. For the C5N1 species, the number of vibrational bands is smaller in the spectrum of the (CO, N_2O) loss channel than in the main (-N_2O); the spectrum for the CO loss is noisy due to small efficiency of fragmentation and it is not clear how many bands it contains. For the C1N4 species, the spectrum recorded in the $2xN_2O$ loss channel shows absence of the band observed at around 2115 cm^{-1} in the spectrum of N_2O loss in addition to different relative intensities between the bands. The calculations will be explored in Section 7.5 in order to understand these differences.

Chapter 7. Energy Flow in Mixed Ligand Complexes $Rh(CO)_n(N_2O)_m^+$
(n = 1−5, m = 1−4)

Thirdly, there seems to be three distinct regions where the bands are, presumably, originating from different binding motifs, and are summarised in the table in Figure 7.4.1.

Some trends in the infrared band positions can be extracted. For a fixed number of adsorbed N_2O molecules, m, with an increasing number of adsorbed CO ligands, n, (up a column in Figure 7.4.1) there is a general blue shift of the band that is to the red from the "free" CO stretch value (with an exception of C1N1 where this band is absent). For $m = 1$, a similar general blue shift is observed for the band that is blue-shifted from the "free" N_2O stretch value for $n = 1-3$ (with a change in its binding motif for $n = 4-5$) as well as for $m = 2$ and 3 (with an exception of C2N2).

Conversely, for a fixed number of adsorbed CO molecules, n, with an increasing number of adsorbed N_2O ligands, m, (across a row in Figure 7.4.1) the position of the band around the "free" CO stretch value is not perturbed by much, except for $n = 1$, where the mentioned band is blue-shifting. Considering the same trend for the blue-shifted band from the "free" N_2O stretch, it is blue-shifting for all n with new bands appearing close to the "free" N_2O stretch in the outer coordination sphere.

The N_2O σ orbital from which the charge is being transferred to the metal is antibonding with respect to the N=N bond, which is thus strengthened in the process of binding to the Rh^+ centre. For a fixed n, some charge density is distributed towards the CO molecule(s), allowing an increase in the σ donation from the N_2O orbitals that is then reflected in the N_2O band blue-shifting with increasing m.

The measured IR-PD spectral bands of the $Rh(CO)_{1-5}(N_2O)^+$ complexes around the "free" CO stretch are very similar to the $Rh(CO)_n$-Ar^+ species recorded by Brathwaite *et al.* [239] (Figure 7.4.2). The spectra are not significantly perturbed but exhibit new bands due to the introduction of an N_2O ligand.

The spectroscopic results of the $Rh(CO)(N_2O)^+_{1-4}$ species are quantitatively similar to Cunningham *et al.* [105] − a general blue-shifting of the N_2O band upon more N_2O molecules adsorbing, reflecting ever stronger σ donation. However, the absolute band positions are red-shifted from their pure N_2O complex values,

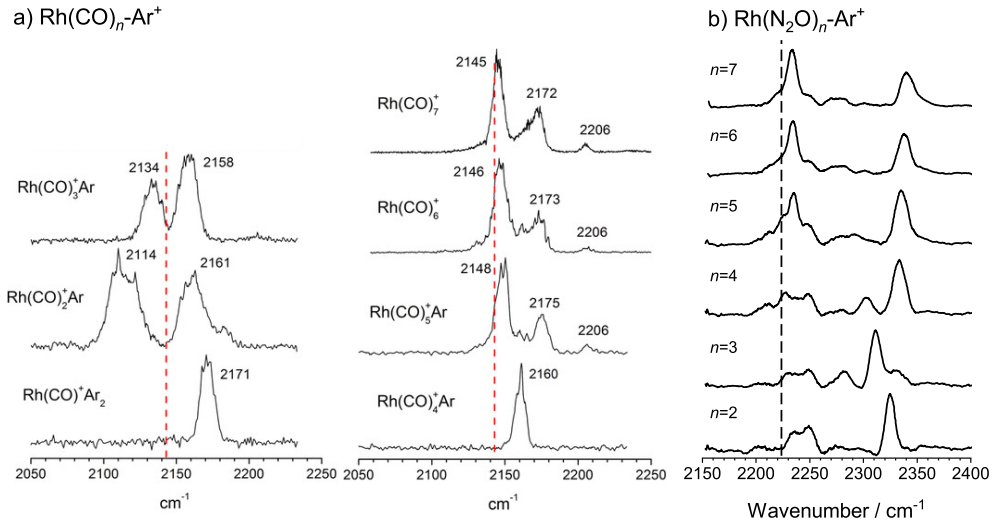

Figure 7.4.2: IR-PD spectra of the a) $Rh(CO)_n$-Ar^+ and b) $Rh(N_2O)_n$-Ar^+ species. They were recorded by Ar-tagging method and assumed not to be perturbed significantly by it. Reprinted with permission from [239] (https://doi.org/10.1021/acs.jpca.6b07749). Copyright 2016 American Chemical Society. Reproduced from Ref. [105] (https://doi.org/10.1039/C8CP05995K) with permission from the PCCP Owner Societies. The dashed red and black lines denote the "free" CO (2143.2 cm^{-1}) [166] and N=N in the "free" N_2O (2223.5 cm^{-1}) [125] stretches, respectively.

presumably because there is a competition of σ donation from the CO ligand, as well as exhibit additional peaks due to the CO ligand.

7.5 Calculated Structures

In an attempt to better understand N_2O binding and reactivity to Rh^+ as well as the effect of CO preadsorption to the metal centre, IRC profiles were calculated and plotted in Figure 7.5.1 for these two cases. For the reaction $Rh^+ + N_2O$, two entrance channels are formed: molecularly-bound N_2O either coordinated *via* the N or O atom (discussed in the next paragraph). As seen in section 7.3, no appreciable oxides were formed, and this can be explained in terms of kinetic barriers. A large barrier to N_2O dissociation (1.41 eV) that leads to the formation of RhO^+ and release of N_2 prevents the reaction taking this route, even though it is thermodynamically possible. These results agree with those of Blagojevic *et*

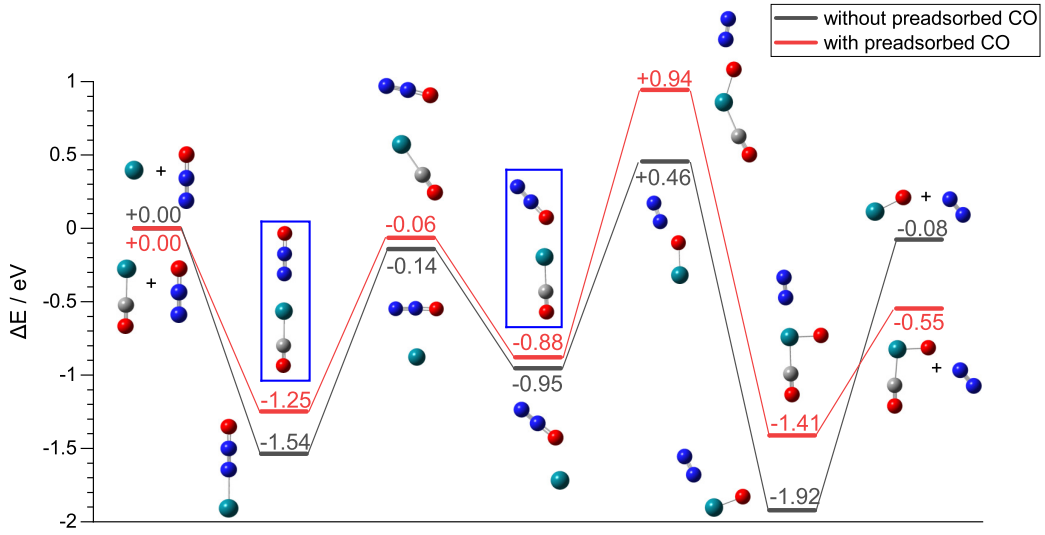

Figure 7.5.1: Intrinsic reaction coordinate for $Rh^+ + N_2O$ (in gray) and $Rh(CO)^+ + N_2O$ (in red) entrance channels. In both cases, all structural energies are plotted as relative energies to their respective reactants. Blue boxes indicate the predominant geometries formed in the molecular beam identified spectroscopically. For all structures, only the lowest energy triplet electronic state is shown.

al. [255] and Rondinelli *et al.* [256] but, to note, in their studies a CO molecule was added downstream (once the N_2 molecule was released).

The main effects of having a CO molecule preadsorbed seem to be an enlargement of the N_2O dissociation barrier and more exothermic (more thermodynamically favoured) release of N_2. Moreover, the binding energy of N_2O to Rh^+ decreases upon CO coadsorption − competitive binding is observed due to similar bonding mechanisms of CO and N_2O to the metal centre. The negative charge is being donated from the antibonding σ orbitals on the ligands to the empty symmetrically compatible orbital on the metal, and so, there is competition between these two flows, *i.e.*, they are not complementary to each other, unlike in the $Au_nO_2CO^-$ system in Chapter 5.

The comparison between experimental spectra of the trend $Rh(CO)_{1-5}(N_2O)^+$ and those predicted by low-lying calculated structures is given in Figure 7.5.2. For this specific trend, the experimental spectra are assigned to all shown computational isomers, and the discussion for this assignment is provided in the paragraphs

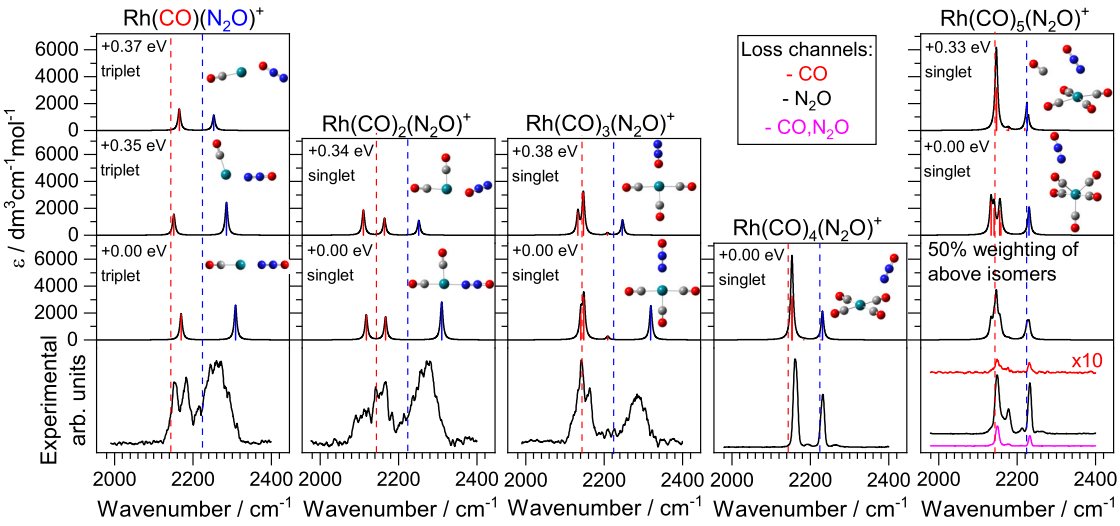

Figure 7.5.2: Calculated low-lying isomers within +0.5 eV of the putative ground state and their vibrational analysis as well as experimental spectra of the $Rh(CO)_n(N_2O)_m^+$ (n = 1–5, m = 1) species presented as the absolute difference in enhancement signal for all observed daughter channels. The band positions in red are due to the vibrations of CO ligands whereas N_2O vibrations are in blue. The dashed red and blue lines denote the experimental values of "free" CO (2143.2 cm^{-1}) [166] and N=N in the "free" N_2O (2223.5 cm^{-1}) [125] stretches, respectively. In some cases, the spectra are enlarged by ten times, as indicated.

below. Generally, a CO molecule binds exclusively *via* the O atom whereas an N_2O molecule can bind either end.

Experimental spectra show evidence for both of these N_2O motifs for the $m \leqslant 3$ complexes, and can be explained in terms of kinetic barriers, e.g. Figure 7.5.1. The barrier of rotation from O-bound to N-bound N_2O in C1N1 compound is 0.82 eV, thus, even though the thermodynamically preferred structure contains N-bound N_2O, the O-bound geometry gets stuck behind the barrier. Both of these motifs give rise to different vibrational spectra: O-bound N_2O vibrations lie close to the "free" N_2O stretch due to the oxygen atom coordinating through its lone pair and thus minimally affecting the N=N stretch whereas N-bound N_2O stretches are blue-shifted from the "free" N_2O value due to donation from the 7σ orbital.

The coordination number of four CO molecules is apparent now in the markedly high resolution of the spectra with $n + m > 4$, agreeing with results from Brathwaite

et al. [239], with CO displacing the N_2O molecule in the core upon coadsorption, suggesting a more favourable interaction of a CO ligand with the Rh^+ metal centre.

As mentioned previously, unlike other species, C5N1 shows additional loss channels, -CO and -(CO, N_2O), but this is due to these molecules adsorbing to the outer coordination sphere in a weaker way than the four ligands in the core (binding energies are discussed in Section 7.6). The difference in spectra between -N_2O and additional loss channels can be explained in terms of selective isomer fragmentation. The calculated putative ground state has five CO molecules directly coordinated to the Rh^+ atom − a secondary solvation shell, as determined by Brathwaite *et al.* [239]. It can only fragment either by losing an N_2O or CO molecule whereas the structure that is +0.33 eV higher in energy has both of these ligands in the outer sphere and can lose both at the same time. The spectrum for CO loss is not very clear, and it cannot be ruled out that the loss is not observed from both isomers. Metals with d^8 configuration that have 16 valence electrons prefer square planar geometries, *e.g.* $Rh(CO)_4^+$ [239] and $Rh(N_2O)_4^+$ [105], but then break the planarity upon having 18 valence electrons [265], as is the case here.

The comparison between experimental spectra of the trend $Rh(CO)(N_2O)_{1-4}^+$ and those predicted by low-lying calculated structures is given in Figure 7.5.3. In all cases, some of the higher energy isomers shown are contributing to the spectra observed, and this will be discussed in the next paragraphs.

Regarding the evidence for N- and O-bound N_2O isomers in the spectra, the discussion above for the $Rh(CO)_{1-5}(N_2O)^+$ trend is valid here as well. The only species that does not have a band at *ca.* 2220 cm^{-1} − a signature of the O-bound N_2O in the core − is C1N2, presumably due to the lower rotational barrier. Generally, larger complexes, with more internal energy, are more facile towards annealing to the lowest energy N-bound geometries, however, due to multiple ligand character there is more steric hindrance with increasing number of N_2O ligands.

Again, a coordination sphere of four ligands is apparent with the C1N4 complex showing an additional -2xN_2O loss channel upon IR irradiation that also involves

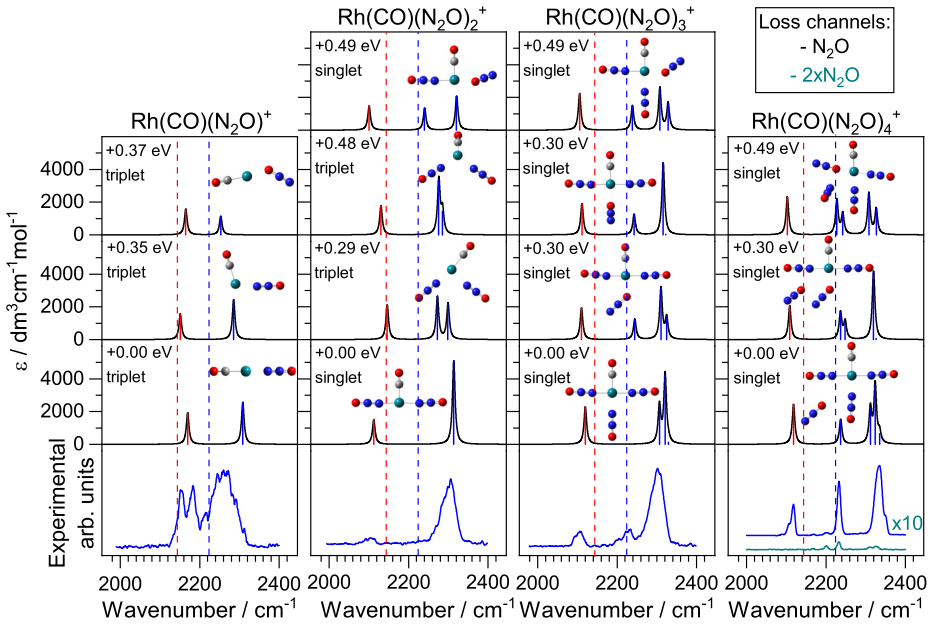

Figure 7.5.3: Calculated low-lying isomers within +0.5 eV from the putative ground state and their vibrational analysis as well as experimental spectra of the $Rh(CO)_n(N_2O)_m^+$ ($n = 1$, $m = 1{-}5$) species presented as the absolute difference in enhancement signal for all observed daughter channels. The band positions in red are due to the vibrations of CO ligand whereas N_2O vibrations are in blue. The dashed red and blue lines denote the experimental values of "free" CO (2143.2 cm^{-1}) [166] and N=N in the "free" N_2O (2223.5 cm^{-1}) [125] stretches, respectively. In some cases, the spectra are enlarged by ten times, as indicated.

an outer N_2O, signified by an appearance of the band around N=N stretch in the "free" N_2O. The spectra are markedly different in the main and additional loss channels – the CO vibrational band is absent in the spectrum of the -2xN_2O loss. This is reminiscent of the $Au(CO)_n(N_2O)_m^+$ species [62, 236], where for some complex compositions the dissociation channel depends on where the energy quanta were absorbed.

With an adsorbed CO molecule ($n = 1$), the crossover to lower multiplicity of the putative ground state structure occurs at $m = 2$, *cf.* at $m = 4$ ($Rh(N_2O)_4^+$) in Cunningham *et al.* study without CO [105], and C1N2 is the only complex size in which there is evidence for low-lying triplet state in addition to the ground singlet. Generally, a CO ligand seems to stabilise the putative ground state of the complex with regards to its multiplicity. An analogous singlet state geometry to

the putative ground state triplet for the C1N1, and triplet to the singlet for the C1N3 and C1N4 complexes are +0.68 eV, 0.78 eV, and 0.83 eV higher in energy, respectively. However, the computed spectral bands are at similar positions, and this experiment cannot differentiate unambiguously between the spin states of the complexes produced. The calculated internal energy can be of some indication but does not provide unequivocal results.

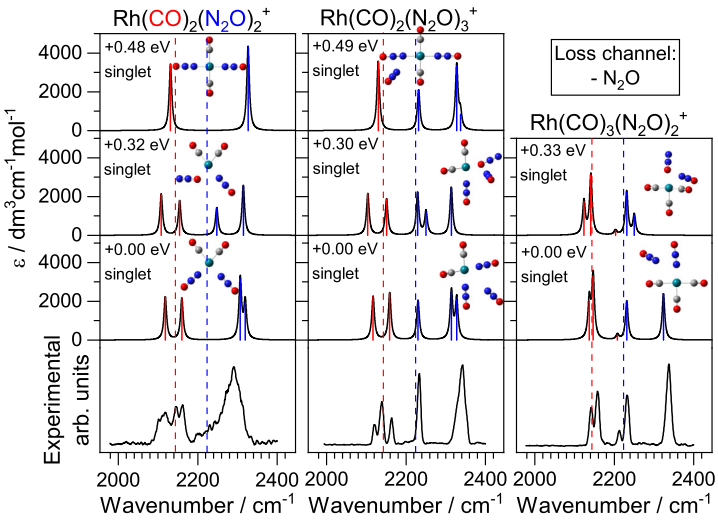

Figure 7.5.4: Calculated low-lying isomers within +0.5 eV from the putative ground state and their vibrational analysis as well as experimental spectra of the $Rh(CO)_n(N_2O)_m^+$ ($n = 2-3$, $m = 2-3$) species presented as the absolute difference in enhancement signal for all observed daughter channels. The band positions in red are due to the vibrations of CO ligands whereas N_2O vibrations are in blue. The dashed red and blue lines denote the experimental values of "free" CO (2143.2 cm^{-1}) [166] and N=N in the "free" N_2O (2223.5 cm^{-1}) [125] stretches, respectively.

The comparison between experimental spectra of the trend $Rh(CO)_{2-3}(N_2O)_{2-3}^+$ and those predicted by low-lying calculated structures is given in Figure 7.5.4. For the C2N2 species, all three isomers shown might be contributing to the spectrum; the band in the N=N in the "free" N_2O stretch region has a shoulder to the right from the main band, which appears to be caused by the O-bound core N_2O-containing isomer. The spectra for the C2N3 and C3N2 complexes include a band at 2234 cm^{-1} and 2232 cm^{-1}, respectively, that is due to the N_2O molecule bound in the outer solvation sphere. For both of these species, the signature for O-bound N_2O is slightly to the blue from this band, and the spectra show no evidence for this.

In all cases where an N_2O is found in the outer sphere, the bands are at the "free" N_2O position, with no meaningful interaction, other than a tag, to the rest of the complex [104, 105, 266, 267]. Whether an outer N_2O ligand is bound through the N or O atom there is no difference in either the spectrum or in the calculated electronic energy of the complex.

7.6 Internal Energy Distributions

The mean internal energy of a complex with i vibrational modes and with respect to the zero-point energy is calculated as:

$$\langle U_{vib} \rangle = \sum_i \frac{h\nu_i}{e^{\frac{h\nu_i}{kT}} - 1}, \tag{7.6.1}$$

where h is the Planck's constant, ν_i denotes the frequency of an ith vibrational mode, k is the Boltzmann constant, and T is the temperature. With respect to $\langle U_{vib} \rangle$, the corresponding vibrational energy distribution is of the form:

$$P(ET) = \frac{\rho(E)e^{-\frac{E}{kT}}}{q(T)}, \tag{7.6.2}$$

where $q(T)$ is the total molecular partition function and $\rho(E)$ is the vibrational state density (in this thesis calculated using the Beyer-Swinehart algorithm [268] employed by the MultiWell software [269]).

Figure 7.6.1 shows such analysis for the putative ground state geometries for the $Rh(CO)_{1-5}(N_2O)^+_{1-4}$ species along with calculated binding energies of different adsorbates to the rest of the complex for calculated putative ground state geometries.

In all cases, an N_2O ligand is bound more weakly than CO, and there is a clear drop in the binding energy of the fifth ligand corresponding to it being in the second solvation shell. These observations explain why there is no CO loss unless it is found in the outer shell. The C1N4 species undergo -2xN_2O loss that is only accessible for the thermally excited part of the tail, which is reflected in the efficiency of fragmentation (Figure 7.4.1). With regards to the C5N1 complex, the binding energy of a CO ligand is smaller than (CO, N_2O), but the amount of

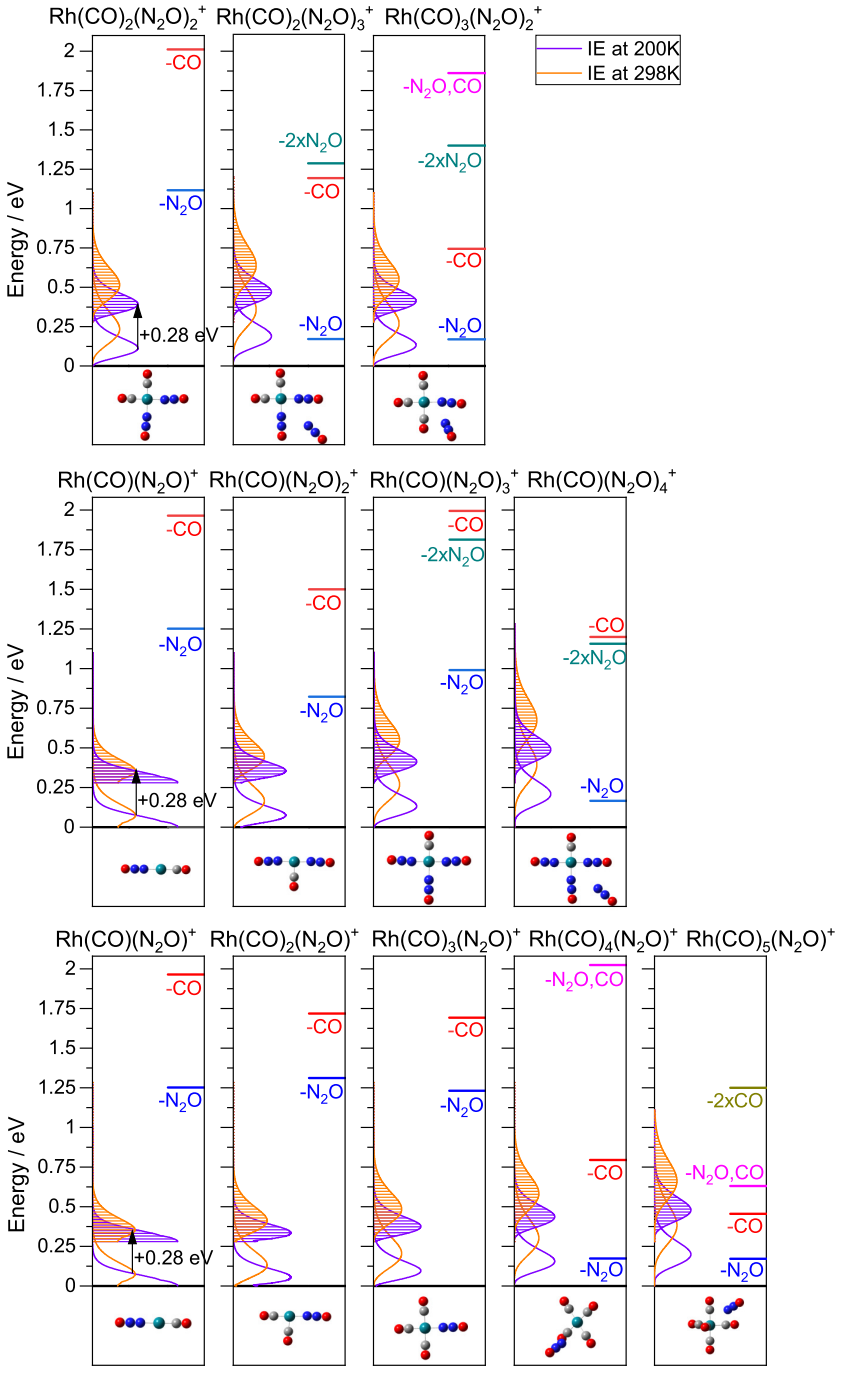

Figure 7.6.1: Internal energy distributions for the putative ground state geometries of the $Rh(CO)_{2-3}(N_2O)_{2-3}^+$ (top panel), $Rh(CO)(N_2O)_{1-4}^+$ (middle panel), and $Rh(CO)_{1-5}(N_2O)^+$ (bottom panel) species at 200K (in purple) and 298K (in orange), with dashed lines showing the distributions upon absorbing a photon of an average energy of $h\nu = 0.28$ eV. The calculated binding energies for different adsorbates are indicated.

fragmentation is larger for the latter. This extra loss channel, -(CO, N_2O), likely arises from the higher in energy +0.33 eV isomer in Figure 7.5.2.

For the complexes that solely undergo N_2O loss upon IR irradiation ($n + m \leqslant 4$), clearly more than one photon is needed in order to access the -N_2O loss channel, and this is apparent in the broad bands in Figure 7.4.1. However, a small amount of complexes that have IE within the "hot" tail in the distribution will be able to access it regardless.

7.7 Single vs. Multiple Photon Study

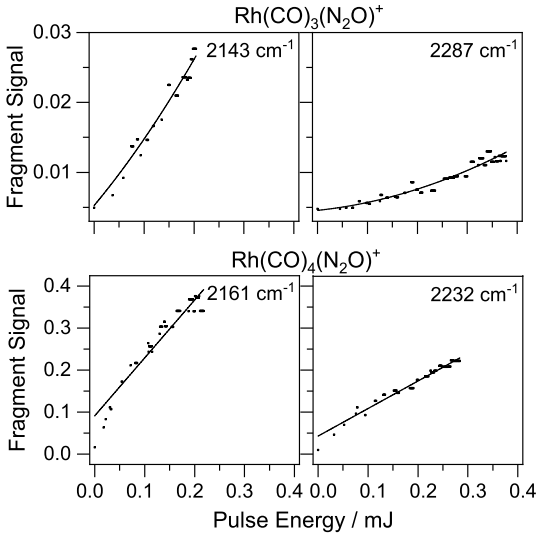

Figure 7.7.1: The dependence of the relative daughter signal (normalised to the sum of the daughter + parent) on the pulse energy of the IR laser for the $Rh(CO)_3(N_2O)^+$ (top) and $Rh(CO)_4(N_2O)^+$ (bottom) complexes at the resonance wavenumbers, as indicated. Quadratic and linear fits are employed for the plots of the $Rh(CO)_3(N_2O)^+$ and $Rh(CO)_4(N_2O)^+$ species, respectively.

The fragment enhancement signal is proportional to the pulse energy to the power of the number of photons, p:

$$signal \propto (energy)^p. \tag{7.7.1}$$

In order to better understand the light absorption processes, the normalised fragment signal (fragment/(fragment + parent)) dependence was plotted with the pulse energy

of the infrared laser for the C3N1 and C4N1 species (Figure 7.7.1). Single and multiple photon processes are signified by the linear and non-linear dependency, respectively, as observed in [62, 236, 270, 271]. Based on Figure 7.6.1, the plotted dependency curve for the C3N1 complexes should have at least quadratic dependency whereas for the C4N1 complexes it should be linear.

The quadratic fit agrees well with the data for the C3N1 species. The linear fit for the C4N1 complexes is not perfect, but still matches the linear fit better than the quadratic fit presented in references [62, 236, 270, 271]. For C4N1, at low pulse energies there is significant deviation from the linearity. It should be noted, though, that at low pulse energies the enhancement of the fragment signal is also small, and this creates greater uncertainties when integrating the area of the daughter peak than in the case of large enhancement.

7.8 Comparison with Gold

The IR-PD spectra of $Au(CO)_n(N_2O)_m^+$ (n = 1–4, m = 1–3) complexes, recorded by Green *et al.* [62, 236] with similar experimental conditions to the rhodium species, are given in Figure 7.8.1.

Rh^+ has d^8 electronic configuration, promoting low-lying excited states, whereas Au^+, a full d^{10} electron shell, only existing in the singlet state, as evident in the DFT computations (Figures 7.5.3, 7.5.2 and [62, 236]). With both metals being late in the periodic table, their carbonyl complexes are termed "non-classical". However, due to their different electronic configurations, the π^* back-bonding is less inefficient in the case of rhodium, resulting in smaller blue shifts of the CO bands from the "free" CO stretch wavenumber, similarly to the N_2O bands.

Au^+ forms linear strongly bound $Au(L)_2^+$ (L = ligand) complexes due to the Orgel effect [272] whereas Rh^+ has a coordination shell of four molecules. As a result, for the size range studied, a plethora of dissociation channels are observed for the gold species, and energy flow effects can be explored by considering branching ratios for different channels with respect to the moiety where energy is injected.

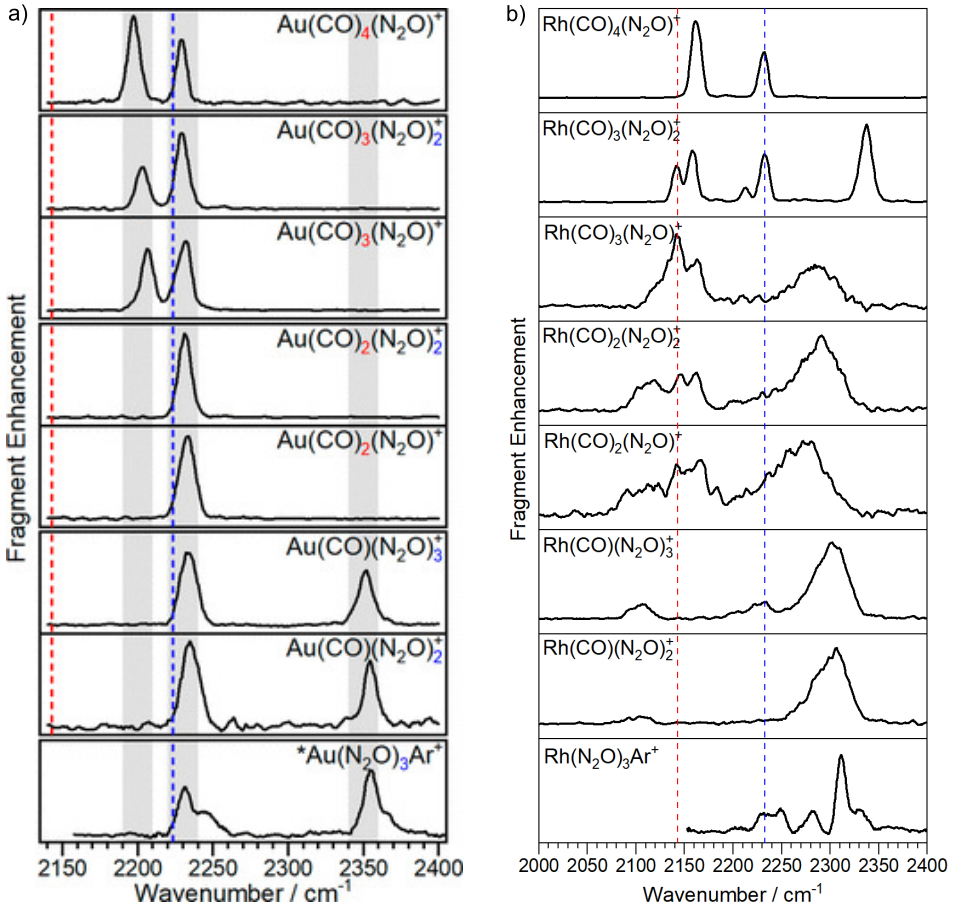

Figure 7.8.1: a) IR-PD spectra of the $Au(CO)_n(N_2O)_m^+$ ($n = 1-4$, $m = 1-3$) species recorded as a total fragment yield of mass-selected parent complexes. The spectrum of $Au(N_2O)_3$-Ar^+ was recorded by Ar-tagging [104]. Reprinted with permission from [62] (https://doi.org/10.1021/acs.jpca.1c05800). Copyright 2021 American Chemical Society. b) IR-PD spectra of the $Rh(CO)_n(N_2O)_m^+$ ($n = 1-4$, $m = 1-3$) species recorded as a total fragment yield of mass-selected parent complexes. The spectrum of $Rh(N_2O)_3$-Ar^+ was previously recorded by Ar-tagging [105]. The dashed red and blue lines denote the experimental values of "free" CO (2143.2 cm^{-1}) [166] and N=N in the "free" N_2O (2223.5 cm^{-1}) [125] stretches, respectively.

Rhodium complexes, however, fragment mainly by losing one N_2O molecule, its binding energy being substantially lower than that of CO.

Chapter 7. Energy Flow in Mixed Ligand Complexes $Rh(CO)_n(N_2O)_m^+$ (n = 1−5, m = 1−4)

7.9 Summary and Conclusions

To sum up, spectra of the $Rh(CO)_n(N_2O)_m^+$ (n = 1−5, m = 1−4) complexes were recorded in the C≡O and N=N stretch regions. With computational aid, a core of four ligands is found which, in some cases, contains both N- and O-bound N_2O motifs. O-bound structures lie energetically higher but are stuck behind a rotational barrier and cannot anneal to lowest energy N-bound structures due to steric hindrance. The spectra and fragmentation dynamics are compared to an analogous gold system, and the differences are explained in terms of different electronic structures, relative binding energies, and coordination numbers.

It would be beneficial to know the temperature (or strictly, the internal energy distribution) of the molecular beam produced in the experiment, which would allow to ascertain the isomers present. This either could be done by thermalising to a specific temperature in an ion trap or cooling the cluster source with liquid nitrogen.

The pulse energy study whether a single or multiple photons were absorbed by the C3N1 and C4N1 species in order to lose an N_2O molecule could be repeated more times in order to calculate the statistical errors involved in addition to making the results more accurate.

IR-PD spectroscopy cannot easily differentiate between different spin states of the complexes produced. In order to state with complete confidence that no excited states are involved, a complementary technique, such as x-ray magnetic circular dichroism spectroscopy in a cryogenic ion trap [273] could be performed.

From the potential energy surface presented in this chapter, there is promise in making the N_2 release more exothermic with CO preadsorption to the metal centre; other metals with low enough barrier to N_2O dissociation presented in Blagojevic *et al.* work [255] could be studied *via* IR-PD spectroscopy.

Chapter 8

Energy Flow in Isotopically-Enriched Metal Ligand Complexes: $Au(^{12/13}CO)_n(N_2O)_m^+$ ($n = 2-3$, $m = 1-2$)

This study is a continuation of our previous investigation of energy flow effects in the single metal mixed ligand $Au(CO)_n(N_2O)_m^+$ complexes [62, 236] in collaboration with Dr Alice Green with findings being prepared for publication. The motivation behind the isotopic labelling experiments was an observation of a sole band in the IR-PD spectrum of the $Au(^{12}CO)_2(N_2O)^+$ species upon scanning both C≡O and N_2O N=N stretch regions. Two possibilities were presented: either this band is an overlap between the individual C≡O and N=N vibrations or the molecule does not fragment when energy is absorbed at the CO moiety. By employing isotopic labelling, the former possibility can be tested; if it is correct, the IR-PD spectrum recorded using the ^{13}CO isotopologue should show two bands.

In this chapter, the IR-PD spectra of $Au(^{12/13}CO)_n(N_2O)_m^+$ ($n = 2-3$, $m = 1-2$) species, with all possible isotopic CO combinations, are presented in the regions of the C≡O and N_2O N=N stretches. In each case, the experimental spectrum is well-reproduced by the simulated spectrum of the calculated putative ground state from DFT, and most importantly, the isotope-induced vibrational perturbations

are replicated. The sole band observed in the spectrum of the $Au(^{12}CO)_2(N_2O)^+$ species is determined to be an overlap of the individual $^{12}C{\equiv}O$ and N=N vibrational bands due to observed red shifts of the $^{13}C{\equiv}O$ band in the IR-PD spectra of the $Au^{12}CO^{13}CO(N_2O)^+$ and $Au(^{13}CO)_2(N_2O)^+$ species.

The calculations and experiments using ^{12}CO gas were performed in collaboration with Dr Alice Green and described in her thesis [236] whereas the experiments using the ^{13}CO isotopologue were led and analysed by me.

8.1 Introduction

The foundational context and relevance of studying CO and N_2O interactions in transition metal complexes have been described previously in Chapter 7. Regarding the interplay of CO and N_2O, an ion trap mass spectrometry study by Popolan *et al.* [274] examined the reactions taking place on the Au_3^+ clusters and revealed CO_2 formation.

The adsorption of N_2O on larger cationic gold clusters has been described in Chapter 4. Regarding Au^+ reactivity towards N_2O, an ICP/SIFT tandem mass spectrometer study by Lavrov *et al.* [275] has been performed previously, and the complexation with an N_2O molecule as well as its second subsequent adsorption reaction channels were observed. Reaction of Au^+ ($^1S_0$ and ^3D) with N_2O was studied *via* guided ion beam tandem mass spectrometry by Li *et al.* [276], and was found to yield the AuO^+, AuN_2^+, and $AuNO^+$ products.

$Au(CO)_n^+$ ($n = 3{-}7$) system has been studied by Duncan and coworkers [31, 277], and $Au(N_2O)_n$-Ar^+ ($n = 2{-}7$) system by Cunningham *et al.* [104] *via* IR-PD spectroscopy coupled with theoretical considerations. Regarding the $Au(CO)_n^+$ complexes, a coordination number of two was found, and the spectra exhibited largely blue-shifted from the "free" CO wavenumber bands, consistent with gold carbonyls termed as "non-classical". The IR-PD spectra of the $Au(N_2O)_n$-Ar^+ complexes indicated trapping of less stable O-bound (*cf.* N-bound) N_2O geometries under

the rotational barrier in addition to suggesting two N_2O ligands as a coordination sphere with blue-shifted vibrational bands from the "free" N_2O N=N stretch value.

Isotopic substitution has been used in many IR spectroscopic characterisation studies for product identification [278–285], where the isotope-induced shifts in the infrared band frequency, rationalised alongside computational work, allows determination of the nature of the species produced in the experiment.

8.2 Experimental and Computational Methods

The time-of-flight and IR-PD spectra were recorded in the Mackenzie laboratory in Oxford. The experimental setup has been described in detail previously [235] and has been modified to include the mass selection of ions via the quadrupole recently [62, 236]. Section 2.3 contains the full description of the instrument, and only a brief one is given here.

A rotating disc target of Au is ablated by a Nd:YAG laser (532 nm, 10 Hz). Ablated atoms cool and cluster by colliding with 1% $^{12/13}$CO and 5% N_2O entrained in Ar in the reaction channel. Various proportions of ^{12}CO and ^{13}CO within the 1% of gas mix were used in order to produce an appropriate amount of the desirable mixed isotope species. The resulting gas mix, entrained with a range of metal-ligated as well as non-metal-ligated clusters, is expanded into the vacuum forming a molecular beam which is then skimmed and mass-selected in the QMF/QMB assembly before entering the extraction region of a reflectron ToF mass spectrometer in cationic detection mode. The experiment is run at room temperature, however, we cannot easily determine the actual temperature of the molecular beam, it is highly dependent on the thermalisation of the clusters.

In order to record the IR-PD spectra, the cluster beam is subjected to alternate pulses of IR off/IR on from the tunable table top OPO/OPA system operating in the 2130-2280 cm^{-1} range. The resulting depletion of the parent ion and any enhancement of the daughter(s) channels are recorded as a function of wavenumber. The information on the infrared active modes of the parent cluster as well as

dissociation yields are produced, and can be readily compared with the results of DFT simulations.

Preliminary isotopic substitution calculations were done for the assigned ground state structures by Green *at al.* [62, 236] at the def2TZVP [76, 77]/B3P86 [237, 238] level using Gaussian 16 software package [118]. This functional has proved to provide reliable results in similar studies by our group in the past [62, 104, 105, 235, 236]. Stuttgart Dresden ECP60 for Au atoms was used in order to include the scalar relativistic effects. To provide a better match with experimental data, computed harmonic vibrational frequencies were scaled to match the value in "free" ^{12}CO and N_2O molecules. Because the experimental spectra using ^{12}CO were assigned to the isomers shown [62, 236], the bands due to the CO stretches were scaled a second time such that the most red-shifted band matches its value in the computed spectra (for ease of comparison). Computed infrared bands are convoluted with FWHM = 8 cm^{-1} Lorentzian shape curves and any reported experimental wavenumber numerical values have an error of ± 10 cm^{-1}.

8.3 Time-of-Flight Spectrum

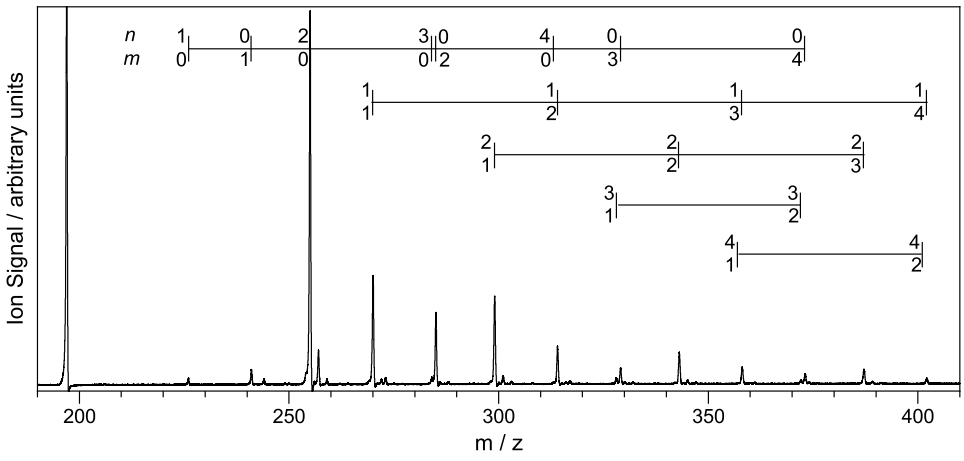

Figure 8.3.1: Time-of-flight mass spectrum of $Au(^{13}CO)_n(N_2O)_m^+$ produced by laser ablation of the Au target in presence of 1% isotopically enriched ^{13}CO and 5% N_2O gas diluted in Ar pulsed at 6 bar.

A representative time-of-flight spectrum produced upon ablation of the gold target in presence of the gas mix of 1% isotopically enriched ^{13}CO and 5% N_2O in Ar is shown in Figure 8.3.1. A range of mixed ligand $Au(^{13}CO)_n(N_2O)_m^+$ clusters are produced with $Au(^{13}CO)_2^+$ exhibiting a pronounced intensity (similarly to $Au(^{12}CO)_2^+$ [31, 62, 236, 277]) – a reflection of the Orgel effect [272]. This behaviour is caused by *sd* hybridisation that results in an enhanced stability of clusters with two ligands adsorbed in a linear fashion on the Au metal centre, also observed in other AuL_y^+ systems [104, 286, 287]. The interaction between the Au centre and CO molecule is stronger than with the N_2O molecule and is reflected in the higher intensity mass peaks of the CO-containing complexes. Overall, as expected, the distribution of the products is similar to that in our previous study by Green *et al.* [62, 236] (shown in Figure 8.3.2).

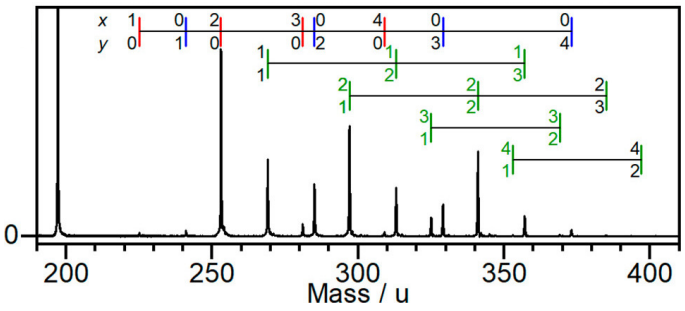

Figure 8.3.2: Time-of-flight mass spectrum of $Au(^{12}CO)_x(N_2O)_y^+$ produced by laser ablation. Different species formed are indicated by red (y = 0), blue (x = 0), and green (x and y>0) lines; green numbers highlight the species authors investigated in their work. Reprinted with permission from [62] (https://doi.org/10.1021/acs.jpca.1c05800). Copyright 2021 American Chemical Society.

Prior to performing spectroscopy, an example of mass-selected species (here, $Au(^{13}CO)_2(^{12}CO)(N_2O)^+$) is given in Figure 8.3.3 under the 'IR off' (black line). When producing the mixed isotope $^{12/13}CO$ clusters, an array of species that differ only by one mass unit are observed in the mass spectrum. Perfect mass selectivity is extremely difficult to achieve without a significant loss in the intensity of the ions that are transmitted through the QMF. Thus, the ion signal in the 'IR off' ToF spectrum is an optimised balance between signal and mass resolution. Upon

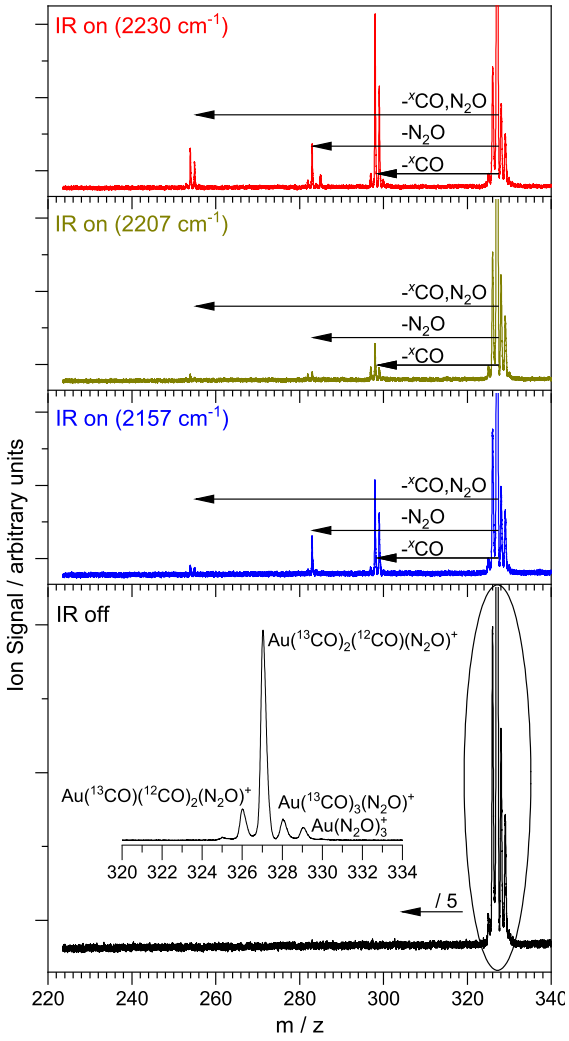

Figure 8.3.3: Mass-selected $Au(^{13}CO)_2(^{12}CO)(N_2O)^+$ species and their ToF mass spectra collected with IR laser off (shown in black) and on at 2157 cm^{-1} (blue), 2207 cm^{-1} (gold), and 2230 cm^{-1} (red). Enhancements of the daughter peaks shown correspond to the loss channels: -$^{12/13}$CO, -N_2O, and -($^{12/13}$CO, N_2O). All mass spectra are appropriately enlarged such that the daughter peaks are visible; in each case, the tick marks have same spacing. The 'IR off' panel also includes the mass spectrum reduced in size by five times to show the neighbouring peaks after mass selection.

irradiation with IR light, the parent species might fragment, and the mass spectra, recorded at each wavenumber where the parent species absorb the IR photons and result in ligand(s) loss, are shown in different colours. The largest fragmentation of the parent species is seen when the IR laser is set at 2230 cm^{-1} – close to the "free" wavenumber of the N_2O N=N stretch (2223.5 cm^{-1}) [125], see Figure 8.4.1.

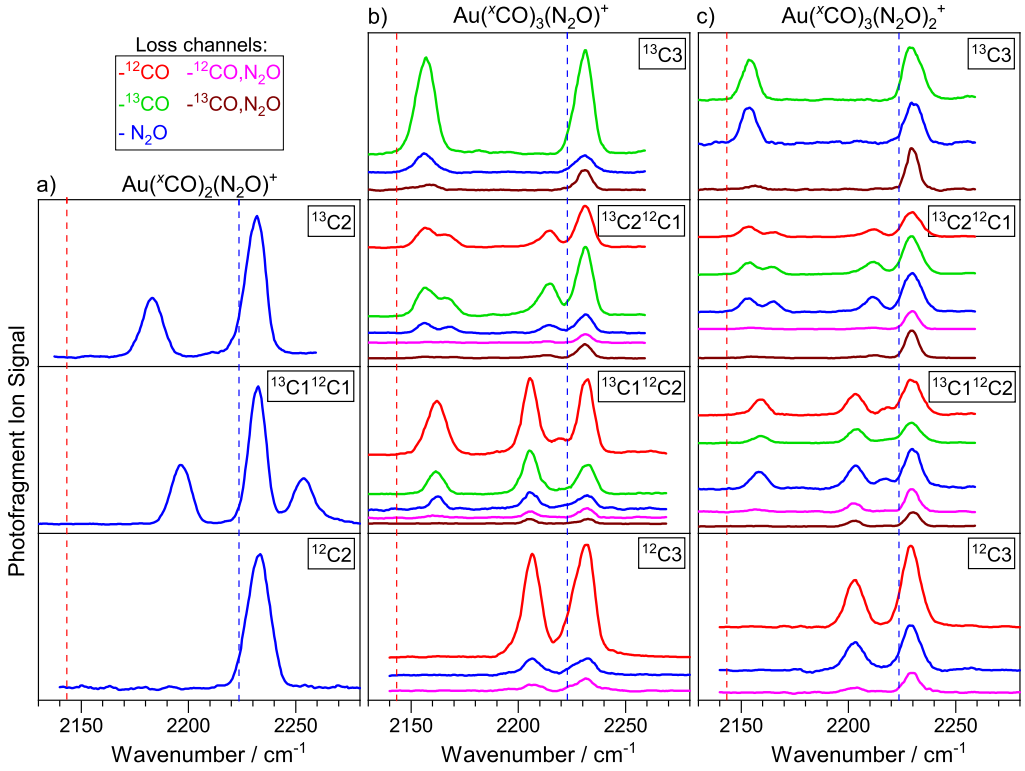

Figure 8.4.1: IR-PD spectra of the a) $Au(^{12/13}CO)_2(N_2O)^+$, b) $Au(^{12/13}CO)_3(N_2O)^+$, and c) $Au(^{12/13}CO)_3(N_2O)_2^+$ clusters presented as the absolute difference in enhancement signal for all observed daughter channels, with all possible isotopic CO combinations, as indicated. The dashed red and blue lines denote the "free" ^{12}CO (2143.2 cm^{-1}) [166] and N_2O N=N (2223.5 cm^{-1}) [125] stretches, respectively.

8.4 IR-PD Spectra

The IR-PD spectra for the a) $Au(^{12/13}CO)_2(N_2O)^+$, b) $Au(^{12/13}CO)_3(N_2O)^+$, and c) $Au(^{12/13}CO)_3(N_2O)_2^+$ clusters are shown in Figure 8.4.1, recorded for all possible isotopic CO combinations. The data using ^{12}CO has been published by Green *et al.* previously [62, 236]. Labels on the right top corner of each spectrum indicate the number of CO molecules with a specific C isotope used, *e.g.* $^{13}C2$ under a) corresponds to the $Au(^{13}CO)_2(N_2O)^+$ species.

Concerning the recorded spectra using only ^{12}CO ligands (bottom row in Figure 8.4.1), the origin of the bands slightly blue-shifted from the "free" N_2O N=N stretch were assigned by Green *et al.* [62, 236] employing DFT as due to the N_2O

molecule(s), whereas the bands around 2205 cm^{-1} – due to the CO molecules. The spectrum for the $Au(^{12}CO)_2(N_2O)^+$ species, however, only presents one band that is to the blue of the "free" N_2O N=N stretch. It was argued in [62, 236] that either the CO vibrational band coincides in its position with the N_2O N=N stretch, or the molecule does not fragment when the light is absorbed at the CO moiety.

Isotopic substitution of one or more ligands is an effective way to deconvolute the aforementioned band and has been employed here. The frequency of the C≡O bond vibration, ν, is expected to red-shift by *ca.* 50 cm^{-1} upon substitution of ^{12}C to ^{13}C according to its dependency on the reduced mass of the molecule, μ:

$$\nu \propto \sqrt{\frac{1}{\mu}}. \tag{8.4.1}$$

As is apparent from Figure 8.4.1, the isotopically expected red shift of the $^{13}C{\equiv}O$ band is reflected in the experimental data and the positions of the N_2O band do not change, just as expected. Thus, the sole band observed in the spectrum of the $Au(^{12}CO)_2(N_2O)^+$ species can be assigned to be an overlap between individual $^{12}C{\equiv}O$ and N=N N_2O vibrations. In b) and c), even upon one ^{12}CO molecule substitution to ^{13}CO, a band emerges at 2160 cm^{-1}. In a), the situation is more interesting, as for the $^{13}C1^{12}C1$ species, a red- as well as a blue-shifted band appears. One has to bear in mind that these vibrations could be normal modes, and not local to a specific CO molecule. Thus, the observed vibrational bands might somewhat be an interplay of the stretches of all CO molecules. The DFT calculations will be discussed in Section 8.5 in order to try to understand the band origins and evolution of the spectra in terms of the vibrations in these molecules.

The efficiency of fragmentation of the parent ions is reflected in the area of the IR-PD band. By monitoring the loss of each ligand(s), the fragmentation pathways are visualised. The efficiency with which each ligand(s) is lost will depend on their binding energy to the metal centre as well as the position in the cluster where the energy is injected.

It was determined by Green *et al.* [62, 236] that the binding energy of CO molecule in all cases is higher than that of N_2O, however, mimicking their results, in this experiment, the efficiency of CO loss is much higher than the N_2O loss. A simple idea was utilised: provided both -CO and -N_2O channels are energetically accessible, the ratio of CO to N_2O ligand loss resembles the respective ratio of each ligand in the parent species. In other words, the loss of CO is more extensive than N_2O when the number of CO ligands in a complex is higher than the number of N_2O ligands. However, the driving factor behind it is not clear. Agreeing with this idea, the $Au(^{12/13}CO)_2(N_2O)^+$ species undergo a sole -N_2O loss since each of the CO molecules are found in the inner solvation shell (a core of two CO molecules was determined [31, 277]) and are too tightly bound.

In Figure 8.4.1, for the $Au(^{12/13}CO)_3(N_2O)^+$ and $Au(^{12/13}CO)_3(N_2O)_2^+$ species, the spectra corresponding to the -CO and -N_2O loss channels are similar but for the -(CO, N_2O) channel is qualitatively different. Namely, the areas under the CO versus N_2O stretches are different, pointing to more efficient IVR if energy is injected at the N_2O moiety. Even more striking is the fact that, as mentioned beforehand, the efficiency of CO ligand loss is much larger than the loss of N_2O ligand. It essentially means that the energy gets stuck in the core, *i.e.* the IVR is less efficient, if the energy is injected at the CO moiety. The results are, again, representative of the ones by Green *et al.* [62, 236]. This phenomenon was explained in terms of coupling efficiencies, and this idea will be considered in Section 8.5.

8.5 Vibrational Modes of the Molecules

Throughout this section, the computational structures that will be presented were assigned in our previous study [62, 236] for species containing ^{12}CO, and for those structures the isotopical labelling calculations were completed.

Computed vibrational analysis, including mode vectors, are given for all possible isotopic CO combinations of the $Au(^{12/13}CO)_2(N_2O)^+$ species in Figure 8.5.1. A

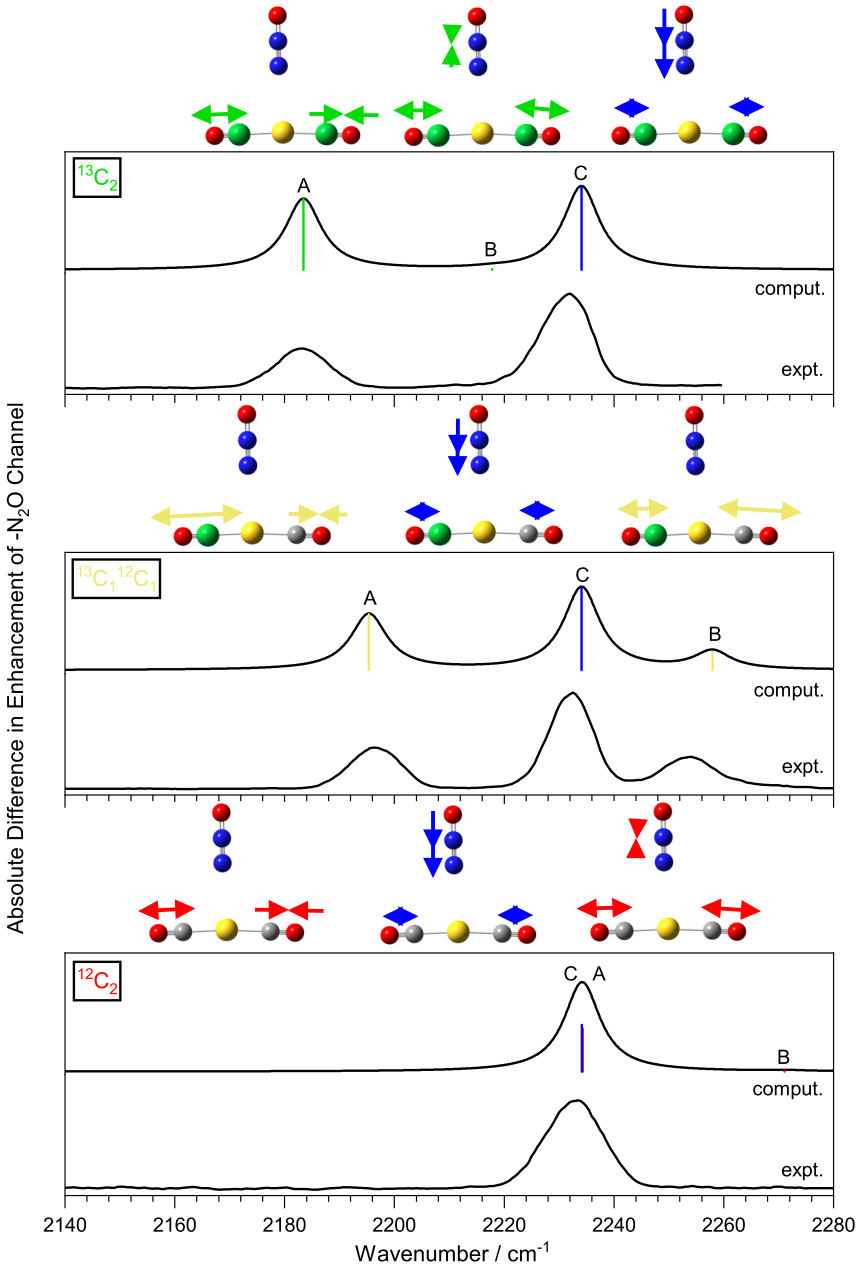

Figure 8.5.1: The comparison of experimental (recorded in the -N_2O channel) and computational spectra of the Au($^{12/13}$CO)$_2$(N_2O)$^+$ species, with all possible isotopic CO combinations. The vibrations are shown in vectors and the length of the vector is indicative of the amplitude of the vibration.

good match between the experimental and computed spectra for all indicated isotopes of carbon is apparent.

The band 'A' denotes the normal mode arising from the out-of-phase vibrations of the CO molecules, the band 'B' from the in-phase vibrations of the CO molecules with a little amount of coupling to the N_2O N=N stretch, and the 'C' band is arising from the N_2O N=N vibration with a small coupling to the in-phase vibration of the CO molecules. The aforementioned blue-shifted band (here, noted as 'B') in the $^{13}C1^{12}C1$ spectrum is actually "silent" in either $^{13}C2$ or $^{12}C2$ spectra due to an insignificant change in the molecule's dipole moment upon vibration, and only when there is a mismatch between the amplitudes it is visible.

The mode analysis in terms of vectors for all possible isotopic combinations of the $Au(^{12/13}CO)_3(N_2O)^+$ species is given in Figure 8.5.2. Generally, the experimental spectra are well-reproduced by the computationally assigned structures.

The band 'A' denotes the normal mode due to two CO molecules vibrating out-of-phase coupled with a smaller amplitude movement of the third CO molecule. Upon having one and two ^{13}CO substituted ligands, this band splits into 'A1' and 'A2' that arise from the out-of-phase and in-phase vibrations of the same isotope CO ligands, respectively. 'A1' is coupled with a miniature vibrational displacement of the third CO adsorbate but in 'A2' it has a similar amplitude as the other CO molecules and vibrates out-of-phase to them. The 'B' mode is due to all CO ligands stretching in-phase coupled with a small symmetric movement of the N_2O molecule whereas mode 'C' arises from the N=N stretch of the N_2O molecule coupled with a small in-phase movement of all CO ligands.

As mentioned previously, the spectra in the -(CO, N_2O) loss channel are qualitatively different from the other channels. The fragmentation of the clusters is much more efficient when the energy is injected into the N_2O moiety than the CO. This can be understood in terms of coupling efficiencies of these ligands. Comparison of the 'A' and 'C' modes reveals that in 'A', which is the CO stretch,

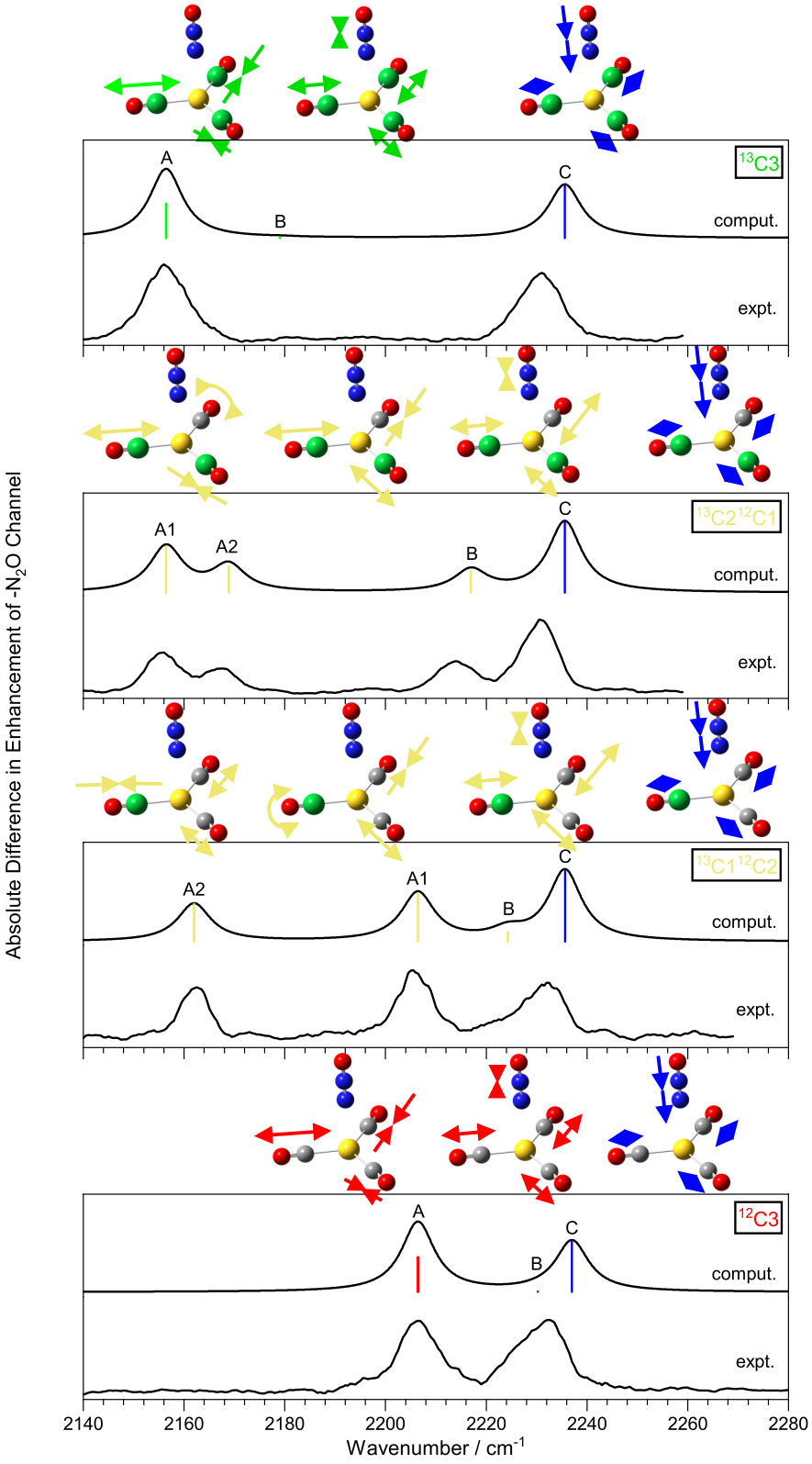

Figure 8.5.2: The comparison of experimental (recorded in the -N_2O channel) and computational spectra of the Au($^{12/13}$CO)$_3$(N_2O)$^+$ species, with all possible isotopic CO combinations. The vibrations are shown in vectors and the length of the vector is indicative of the amplitude of the vibration.

N_2O is not coupled to the other CO ligands, whereas in 'C', which is the N_2O stretch, the CO ligands are.

A similar mode analysis for the $Au(^{12/13}CO)_3(N_2O)_2^+$ species is shown in Figure 8.5.3. Again, the match between the experimental and computational spectra is clear. The band assignments are similar to Figure 8.5.2, but includes vibrations due to an additional N_2O ligand. One of the differences is that the 'A2' and 'B' bands are coupled with an asymmetric movement of both N_2O ligands towards each other. The 'C' mode arises from the in-phase asymmetric vibration of the N_2O ligands with weak coupling to the other CO ligands.

In reality, however, the CO molecules are not perfectly orthogonal to the N_2O ligands and the N_2O ligands are not strictly linear due to the zero-point molecular vibrations as well as low frequency modes. Thus, there is likely some vibrational coupling between them, and it is evident in the spectra in Figure 8.4.1. There is no apparent coupling of the CO vibrations to the N_2O ligands in Figure 8.5.3 as well, and the same rationale can be applied.

The question still remains, though, why the loss of (CO, N_2O) moiety is much smaller when the energy is injected at the CO resonance, *cf.* N_2O (Figure 8.4.1). Perhaps the answer also lies in the counting of the ligands. As mentioned previously, the efficiency of CO loss is greater than the N_2O due to the ratio of ligands in the cluster being CO:$N_2O > 1$. And so, because the CO loss is more extensive, there are fewer CO moieties to inject the energy at, and consequently lose the (CO, N_2O) species. This rationale could also apply to the $Au(^{12/13}CO)_3(N_2O)^+$ species.

8.6 Summary and Conclusions

To summarise, IR spectra of the $Au(^{12/13}CO)_n(N_2O)_m^+$ ($n = 2$–3, $m = 1$–2) species for all CO isotope combinations were recorded in the C≡O and N_2O N=N stretch regions, and were shown to be well-reproduced by DFT simulations. The isotopic shift in the frequency of the CO band for the $Au(^{12/13}CO)_2(N_2O)^+$ species proved that the spectrum of $Au(^{12}CO)_2(N_2O)^+$ contains CO and N_2O bands that overlap

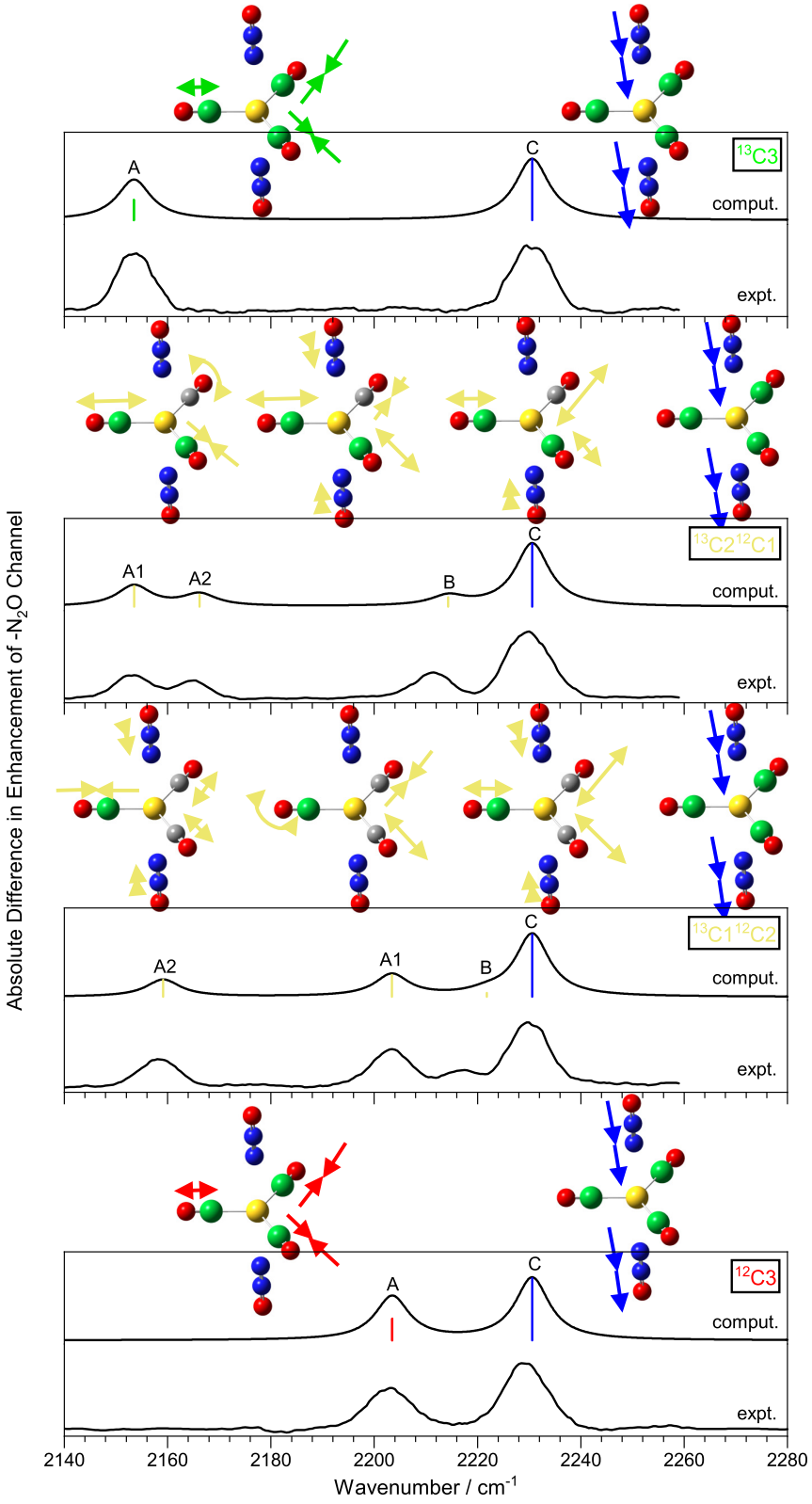

Figure 8.5.3: The comparison of experimental (recorded in the -N_2O channel) and computational spectra of the Au($^{12/13}$CO)$_3$(N_2O)$_2^+$ species, with all possible isotopic CO combinations. The vibrations are shown in vectors and the length of the vector is indicative of the amplitude of the vibration.

with each other. Spectra recorded in the loss of different moieties proved sensitive to the band where energy is injected, and was explained in terms of ligand counting as well as the geometry of the species.

The calculations in the Green *et al.* [62, 236] publication indicated a similar spectral outcome to the $Au(^{12/13}CO)_2(N_2O)^+$ species explored in this chapter, demonstrating a sole band which is, most likely, composed of the CO and N_2O vibrational bands. Specifically, the isotopic experiments and complementary calculations could be extended to include the $Au(^{12/13}CO)(N_2O)_2^+$, $Au(^{12/13}CO)(N_2O)_3^+$, and $Au(^{12/13}CO)_2(N_2O)_2^+$ systems to confirm whether the observed vibrational bands are overlaps of individual vibrations. This study would benefit from modelling energy flow, perhaps with time-dependent DFT, in order to better understand the observed energy bottlenecks and the reason ligand counting guides more efficient loss of a stronger bound CO ligand.

In each case, upon mass selection of a specific peak, there was small amount of $\pm$ 1 mass units species coming through the mass gate, evident in the recorded mass-selected ToF spectra. No attempt was made to subtract the spectrum coming from different species in the same loss channel as the amount of non-selected species was too low to obscure the main spectral features, however, it could be done to improve the recorded spectra.

Chapter 9

Conclusions

This thesis has described several studies of metal-containing clusters and complexes with atmospherically relevant adsorbates, using IR-PD and complementary DFT calculations. Each chapter has described a different system. In each case, the mass spectra give information on reactivity; structural binding motifs and the degree of activation of adsorbed moieties are extracted and analysed from the IR spectra obtained.

Distinct reactivity of small (n = 3−5) versus large (n = 6−8) Pt_n^+ clusters towards N_2O is observed in Chapter 3. Small clusters combine with N_2O forming molecular adsorption products whereas larger ones react to produce Pt_nO^+. Similar reactivity is also seen upon IR excitation in the N_2O N=O and N=N stretches (N_2O and N_2 desorption for small and larger clusters, respectively). These findings are rationalised by calculated potential energy surface profiles.

Chapter 4 presents a similar study to Chapter 3 but of Au_n^+ ($n \leqslant 7$) and Co_n^+ ($n \leqslant 5$) clusters. In terms of reactivity, the Au_n^+ species are found to be relatively inert whereas Co_n^+ react similarly to the Pt_n^+ clusters. For Co_n^+, small ($n \leqslant 2$) adsorb N_2O molecularly whereas larger ($n > 3$) clusters react to form oxides. The 1000-1200 cm^{-1} region where one of the O-bound N_2O signature bands are located is presented in this chapter but it is concluded that these isomers are not present in the molecular beam.

The adsorption of O_2 as well as CO on Au_n^- (n = 2−8, even n) has been investigated in Chapter 5, where size-selective cooperative binding effects are

observed (for $n = 2$, 6, and 8). The most interesting finding involves the change of O_2 binding mode from end-on to side-on upon CO coadsorption to the Au_6^- cluster. The preference of a particular O_2 binding motif is explained in terms of regioselectivity with respect to the partial charge distribution on the Au_n^- core.

The experiments in Chapters 3-5 were carried out in the Fritz Haber Institute in Berlin, where the setup is optimised to produce larger metal clusters with individual adsorbates. Chapters 6-8 present the studies performed in the Oxford laboratory, where, by contrast, complexes of multiple ligands adsorbed on a single metal ion are produced.

Studying NO binding at Group 9 ions (Co_n^+ and Rh_n^+ ($n \geqslant 8$)) reveals the signature of NO dimer motifs for the $n \geqslant 5$ complexes as well as significant differences in the IR-PD spectra between the Co^+ and Rh^+ complexes. The closing of the coordination shell at $Co(NO)_4^+$ and $Rh(NO)_6^+$ is determined, which in addition to the Rh complexes containing multiple isomers, help to explain these spectral differences. The infrared action spectra of pure $(NO)_n^+$−containing complexes show stark differences to the spectra recorded by Stace and coworkers [226, 227]. The future directions include performing exhaustive DFT calculations that may help in explaining these differences, perhaps in the context of different experimental conditions leading to different internal energy distributions of the isomers produced. The $Ir(NO)_n^+$ complexes are being studied at the moment in the Mackenzie laboratory and will provide an opportunity to compare the results of the whole triad. Work on the $Pt(NO)_n^+$ complexes has also started, which will allow for further comparison between Groups 9 and 10. Another possibility would be to study anionic counterparts (Co_n^-, Rh_n^-, and Ir_n^-), which may result in much more significant molecular activation.

Mixed ligand effects in the $Rh(CO)_n(N_2O)_m^+$ ($n = 1$−5, $m = 1$−4) complexes are explored in Chapter 7, and compared to the $Au(CO)_n(N_2O)_m^+$ studied previously [62, 236]. In some cases, kinetically trapped O-bound N_2O isomers are observed in the spectra that are stuck behind a rotational barrier to the thermodynamically

preferred N-bound geometries on the potential energy surface profile. Irrespective of the nature of the ligand (CO or N_2O), the coordination shell of four is observed, with CO displacing N_2O upon binding to the Rh^+ centre. This did not allow the study of the energy flow effects seen in the gold system [62, 236]. Metals that have lower coordination numbers, such as the coinage group, would make interesting systems to study the energy flow effects in the future.

A continuation of the $Au(CO)_n(N_2O)_m^+$ study [62, 236] realised by isotopic ^{13}CO experiments is described in Chapter 8. An overlap of the individual $^{12}C{\equiv}O$ and N_2O N=N vibrational bands is determined for the $Au^{12}(CO)_2(N_2O)^+$ complex, and most likely this explanation can be extended to the $Au(^{12/13}CO)(N_2O)_2^+$, $Au(^{12/13}CO)(N_2O)_3^+$, and $Au(^{12/13}CO)_2(N_2O)_2^+$ systems, where a sole band is observed in the IR-PD spectra as well. Similarly to $Au^{12}(CO)_n(N_2O)_m^+$ [62, 236], unexpected fragmentation pathways (stronger bound CO ligand fragments more easily than weaker bound N_2O) and different dissociation yields for the loss of (CO, N_2O) moiety with IR photon absorption at the CO or N_2O vibrational band are observed. These findings should be studied further computationally, *e.g.* by energy flow modelling, in order to better understand such unexpected outcomes.

Appendices

Appendix A

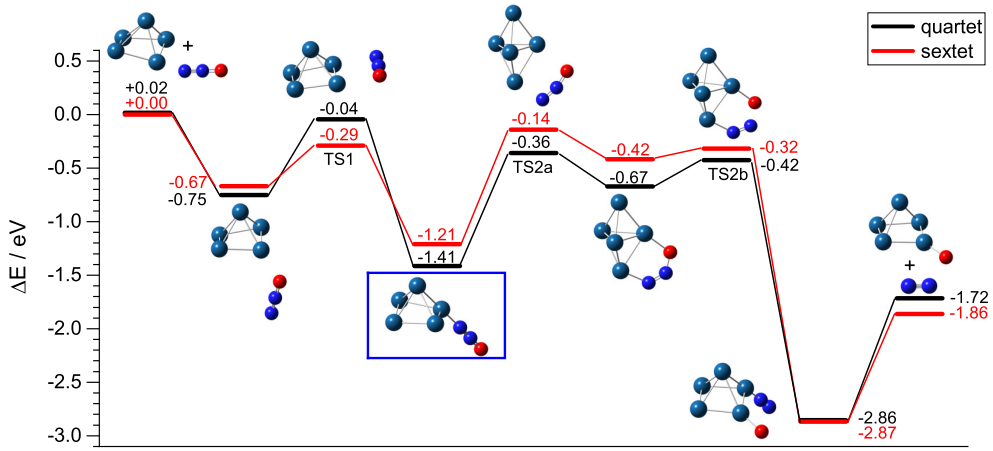

Figure 9.0.1: IRC pathway for the $Pt_5^+ + N_2O$ reaction; as Figure 3.4.1 in Chapter 3 but with calculated sextet structures shown. Adapted from Ref. [60] (https://doi.org/10.1039/D0CP02800B) with permission from the PCCP Owner Societies.

Bibliography

[1] J. Jortner. Cluster size effects. *Zeitschrift für Physik D Atoms, Molecules and Clusters*, 24(3):247–275, 1992.

[2] A. W. Castleman and K. H. Bowen. Clusters: Structure, energetics, and dynamics of intermediate states of matter. *The Journal of Physical Chemistry*, 100(31):12911–12944, 1996.

[3] S. M. Lang and T. M. Bernhardt. Gas phase metal cluster model systems for heterogeneous catalysis. *Physical Chemistry Chemical Physics*, 14(26):9255–9269, 2012.

[4] Z. Luo and S. N. Khanna. *Metal clusters and their reactivity*. Springer, Singapore, 2020.

[5] V. Bonačić-Koutecký, R. Mitrić, C. Bürgel, and B. Schäfer-Bung. Cluster properties in the regime in which each atom counts. *Computational Materials Science*, 35(3):151–157, 2006.

[6] D. M. Popolan, M. Nossler, R. Mitric, T. M. Bernhardt, and V. Bonacic-Koutecky. Tuning cluster reactivity by charge state and composition: Experimental and theoretical investigation of CO binding energies to $Ag_nAu_m^{+/-}$ $(n+m = 3)$. *The Journal of Physical Chemistry A*, 115(6):951–959, 2011.

[7] Y. Iizuka, T. Tode, T. Takao, K. I. Yatsu, T. Takeuchi, S. Tsubota, and M. Haruta. A kinetic and adsorption study of CO oxidation over unsupported fine gold powder and over gold supported on titanium dioxide. *Journal of Catalysis*, 187(1):50–58, 1999.

[8] M. Okumura, Y. Kitagawa, M. Haruta, and K. Yamaguchi. DFT studies of interaction between O_2 and Au clusters. the role of anionic surface Au atoms on Au clusters for catalyzed oxygenation. *Chemical Physics Letters*, 346(1):163–168, 2001.

[9] D. J. Harding, C. Kerpal, G. Meijer, and A. Fielicke. Activated methane on small cationic platinum clusters. *Angewandte Chemie International Edition*, 51(3):817–819, 2012.

[10] K. M. DeWitt, L. Valadez, H. L. Abbott, K. W. Kolasinski, and I. Harrison. Using effusive molecular beams and microcanonical unimolecular rate theory to characterize ch_4 dissociation on pt (111). *The Journal of Physical Chemistry B*, 110(13):6705–6713, 2006.

[11] D. K. Boehme and H. Schwarz. Gas-phase catalysis by atomic and cluster metal ions: The ultimate single-site catalysts. *Angewandte Chemie International Edition*, 44(16):2336–2354, 2005.

[12] Y. Watanabe. Atomically precise cluster catalysis towards quantum controlled catalysts. *Science and Technology of Advanced Materials*, 15(6):063501, 2014.

[13] H. J. Freund, G. Meijer, M. Scheffler, R. Schlögl, and M. Wolf. CO oxidation as a prototypical reaction for heterogeneous processes. *Angewandte Chemie International Edition*, 50(43):10064–10094, 2011.

[14] H. S. Taylor. A theory of the catalytic surface. *Proceedings of the Royal Society of London. Series A, Containing Papers of a Mathematical and Physical Character*, 108(745):105–111, 1925.

[15] H. Guo, W. Ji, J. C. Polanyi, and J. Yang. Molecular dynamics of localized reaction, experiment and theory: Methyl bromide on Si(111)-7×7. *ACS Nano*, 2(4):699–706, 2008.

[16] W. T. Wallace and R. L. Whetten. Coadsorption of CO and O_2 on selected gold clusters: evidence for efficient room-temperature CO_2 generation. *Journal of the American Chemical Society*, 124(25):7499–7505, 2002.

[17] O. P. Balaj, I. Balteanu, T. T. J. Roßteuscher, M. K. Beyer, and V. E. Bondybey. Catalytic oxidation of CO with N_2O on gas-phase platinum clusters. *Angewandte Chemie International Edition*, 43(47):6519–6522, 2004.

[18] K. R. Asmis and A. Fielicke. Size-selected clusters as model systems for catalysis. *Topics in Catalysis*, 61(1):1–2, 2018.

[19] T. G. Dietz, M. A. Duncan, D. E. Powers, and R. E. Smalley. Laser production of supersonic metal cluster beams. *The Journal of Chemical Physics*, 74(11):6511–6512, 1981.

[20] H. W. Kroto, J. R. Heath, S. C. O'Brien, R. F. Curl, and R. E. Smalley. C60: Buckminsterfullerene. *Nature*, 318(6042):162–163, 1985.

[21] V. E. Bondybey and J. H. English. Laser induced fluorescence of metal clusters produced by laser vaporization: Gas phase spectrum of Pb_2. *The Journal of Chemical Physics*, 74(12):6978–6979, 1981.

[22] O. F. Hagena. Nucleation and growth of clusters in expanding nozzle flows. *Surface Science*, 106(1-3):101–116, 1981.

[23] M. A. Duncan. Invited review article: laser vaporization cluster sources. *Review of Scientific Instruments*, 83(4):041101, 2012.

[24] E. C. Honea, M. L. Homer, J. L. Persson, and R. L. Whetten. Generation and photoionization of cold na_n clusters; n to 200. *Chemical Physics Letters*, 171(3):147–154, 1990.

[25] A. Fielicke, A. Kirilyuk, C. Ratsch, J. Behler, M. Scheffler, G. von Helden, and G. Meijer. Structure determination of isolated metal clusters via far-infrared spectroscopy. *Physical Review Letters*, 93(2):023401, 2004.

[26] S. Maruyama, L. R. Anderson, and R. E. Smalley. Direct injection supersonic cluster beam source for FT-ICR studies of clusters. *Review of Scientific Instruments*, 61(12):3686–3693, 1990.

[27] U. Heiz, F. Vanolli, L. Trento, and W. D. Schneider. Chemical reactivity of size-selected supported clusters: An experimental setup. *Review of Scientific Instruments*, 68(5):1986–1994, 1997.

[28] J. E. Reddic and M. A. Duncan. Photodissociation spectroscopy of the Mg^+-Ne complex. *The Journal of Chemical Physics*, 110(20):9948–9955, 1999.

[29] A. M. Ricks, J. M. Bakker, G. E. Douberly, and M. A. Duncan. Infrared spectroscopy and structures of cobalt carbonyl cations, $Co(CO)_n^+$ (n = 1-9). *The Journal of Physical Chemistry A*, 113(16):4701–4708, 2009.

[30] A. M. Ricks, Z. D. Reed, and M. A. Duncan. Seven-coordinate homoleptic metal carbonyls in the gas phase. *Journal of the American Chemical Society*, 131(26):9176–9177, 2009.

[31] A. M. Ricks, Z. E. Reed, and M. A. Duncan. Infrared spectroscopy of mass-selected metal carbonyl cations. *Journal of Molecular Spectroscopy*, 266(2):63–74, 2011.

[32] B. F. G. Johnson and J. S. McIndoe. Spectroscopic and mass spectrometric methods for the characterisation of metal clusters. *Coordination Chemistry Reviews*, 200(202):901–932, 2000.

[33] M. Maier-Borst, D. B. Cameron, M. Rokni, and J. H. Parks. Electron diffraction of trapped cluster ions. *Physical Review A*, 59(5):R3162, 1999.

[34] X. Xing, B. Yoon, U. Landman, and J. H. Parks. Structural evolution of Au nanoclusters: From planar to cage to tubular motifs. *Physical Review B*, 74(16):165423, 2006.

[35] S. Krückeberg, D. Schooss, M. Maier-Borst, and J. H. Parks. Diffraction of trapped $(CsI)_nCs^+$: the appearance of bulk structure. *Physical Review Letters*, 85(21):4494, 2000.

[36] D. J. Harding and A. Fielicke. Platinum group metal clusters: From gas-phase structures and reactivities towards model catalysts. *Chemistry–A European Journal*, 20(12):3258–3267, 2014.

[37] T. Suzuki, K. Kato, H. Tanaka, K. Isoyama, R. Kanya, and K. Yamanouchi. Determination of geometrical structure of CCl_3^+ by trapped-ion electron diffraction. *Chemical Physics Letters*, page 139753, 2022.

[38] E. A. Mason and E. W. McDaniel. *Transport properties of ions in gases*, volume 26. Wiley Online Library, 1988.

[39] P. R. Kemper and M. T. Bowers. Electronic-state chromatography: application to first-row transition-metal ions. *The Journal of Physical Chemistry*, 95(13):5134–5146, 1991.

[40] G. Von Helden, N. G. Gotts, and M. T. Bowers. Experimental evidence for the formation of fullerenes by collisional heating of carbon rings in the gas phase. *Nature*, 363(6424):60–63, 1993.

[41] P. Weis, T. Bierweiler, S. Gilb, and M. M. Kappes. Structures of small silver cluster cations (Ag_n^+, $n < 12$): ion mobility measurements versus density functional and MP2 calculations. *Chemical Physics Letters*, 355(3):355–364, 2002.

[42] F. Furche, R. Ahlrichs, P. Weis, C. Jacob, S. Gilb, T. Bierweiler, and M. M. Kappes. The structures of small gold cluster anions as determined by a combination of ion mobility measurements and density functional calculations. *The Journal of Chemical Physics*, 117(15):6982–6990, 2002.

[43] R. R. Hudgins, M. Imai, M. F. Jarrold, and P. Dugourd. High-resolution ion mobility measurements for silicon cluster anions and cations. *The Journal of Chemical Physics*, 111(17):7865–7870, 1999.

[44] M. F. Jarrold and J. E. Bower. Mobilities of metal cluster ions aluminum (Al_n^+ and Al_n^{2+}): effect of charge on cluster geometry. *The Journal of Physical Chemistry*, 97(9):1746–1748, 1993.

[45] A. A. Shvartsburg and M. F. Jarrold. Solid clusters above the bulk melting point. *Physical Review Letters*, 85(12):2530, 2000.

[46] A. A. Shvartsburg and M. F. Jarrold. Transition from covalent to metallic behavior in group-14 clusters. *Chemical Physics Letters*, 317(6):615–618, 2000.

[47] D. Schooss, P. Weis, O. Hampe, and M. M. Kappes. Determining the size-dependent structure of ligand-free gold-cluster ions. *Philosophical Transactions of the Royal Society A: Mathematical, Physical and Engineering Sciences*, 368(1915):1211–1243, 2010.

[48] E. J. Bieske and J. P. Maier. Spectroscopic studies of ionic complexes and clusters. *Chemical Reviews*, 93(8):2603–2621, 1993.

[49] M. A. Duncan. Frontiers in the spectroscopy of mass-selected molecular ions. *International Journal of Mass Spectrometry*, 200(1-3):545–569, 2000.

[50] K. R. Asmis. Structure characterization of metal oxide clusters by vibrational spectroscopy: possibilities and prospects. *Physical Chemistry Chemical Physics*, 14(26):9270–9281, 2012.

[51] M. R. Zakin, R. O. Brickman, D. M. Cox, K. C. Reichmann, D. J. Trevor, and A. Kaldor. Infrared spectroscopy of unsupported metal cluster complexes using multiple photon dissociation. *The Journal of Chemical Physics*, 85(2):1198–1199, 1986.

[52] R. Prazeres, J. M. Berset, R. Chaput, F. Glotin, D. A. Jaroszynski, and J. M. Ortega. CLIO, an infrared free electron laser facility. *Nuclear Instruments and Methods in Physics Research Section B: Beam Interactions with Materials and Atoms*, 89(1-4):54–59, 1994.

[53] D. Oepts, A. F. G. Van der Meer, and P. W. Van Amersfoort. The free-electron-laser user facility FELIX. *Infrared physics & technology*, 36(1):297–308, 1995.

[54] M. Z. Kamrath, E. Garand, P. A. Jordan, C. M. Leavitt, A. B. Wolk, M. J. Van Stipdonk, S. J. Miller, and M. A. Johnson. Vibrational characterization of simple peptides using cryogenic infrared photodissociation of H_2-tagged, mass-selected ions. *Journal of the American Chemical Society*, 133(16):6440–6448, 2011.

[55] M. Z. Kamrath, R. A. Relph, T. L. Guasco, C. M. Leavitt, and M. A. Johnson. Vibrational predissociation spectroscopy of the H_2-tagged mono-and dicarboxylate anions of dodecanedioic acid. *International Journal of Mass Spectrometry*, 300(2-3):91–98, 2011.

[56] M. Okumura, L. I. Yeh, J. D. Myers, and Y. T. Lee. Infrared spectra of the cluster ions $H_7O_3^+ \cdot H_2$ and $H_9O_4^+ \cdot H_2$. *The Journal of Chemical Physics*, 85(4):2328–2329, 1986.

[57] K. Mizuse and A. Fujii. Tuning of the internal energy and isomer distribution in small protonated water clusters $H^+(H_2O)_{4-8}$: An application of the inert gas messenger technique. *The Journal of Physical Chemistry A*, 116(20):4868–4877, 2012.

[58] P. Gruene, D. M. Rayner, B. Redlich, A. F. G. van der Meer, J. T. Lyon, G. Meijer, and A. Fielicke. Structures of neutral Au_7, Au_{19}, and Au_{20} clusters in the gas phase. *Science*, 321(5889):674–676, 2008.

[59] A. E. Green, S. Schaller, G. Meizyte, B. J. Rhodes, S. P. Kealy, A. S. Gentleman, W. Schöllkopf, A. Fielicke, and S. R. Mackenzie. Infrared study of OCS binding and size-selective reactivity with gold clusters, Au_n^+ (n = 1–10). *The Journal of Physical Chemistry A*, 124(26):5389–5401, 2020.

[60] G. Meizyte, A. E. Green, A. S. Gentleman, S. Schaller, W. Schöllkopf, A. Fielicke, and S. R. Mackenzie. Free electron laser infrared action spectroscopy of nitrous oxide binding to platinum clusters, $Pt_n(N_2O)^+$. *Phys. Chem. Chem. Phys.*, 22:18606–18613, 2020.

[61] E. M. Cunningham, A. E. Green, G. Meizyte, A. S. Gentleman, P. W. Beardsmore, S. Schaller, K. M. Pollow, K. Saroukh, M. Förstel, O. Dopfer, W. Schöllkopf, A. Fielicke, and S. R. Mackenzie. Infrared action spectroscopy of nitrous oxide on cationic gold and cobalt clusters. *Phys. Chem. Chem. Phys.*, 23(1):329–338, 2021.

[62] A. E. Green, R. H. Brown, G. Meizyte, and S. R. Mackenzie. Spectroscopy and infrared photofragmentation dynamics of mixed ligand ion–molecule complexes: $Au(CO)_x(N_2O)_y^+$. *The Journal of Physical Chemistry A*, 125(33):7266–7277, 2021.

[63] P. M. Morse. Diatomic molecules according to the wave mechanics. ii. vibrational levels. *Physical Review*, 34(1):57, 1929.

[64] W. C. Wiley and I. H. McLaren. Time-of-flight mass spectrometer with improved resolution. *Review of Scientific Instruments*, 26(12):1150–1157, 1955.

[65] B. A. Mamyrin, V. I. Karataev, D. V. Shmikk, and V. A. Zagulin. The mass-reflectron, a new nonmagnetic time-of-flight mass spectrometer with high resolution. *Zh. Eksp. Teor. Fiz*, 64(1):82–89, 1973.

[66] I. S. Parry, A. C. Hermes, A. Kartouzian, and S. R. Mackenzie. Imaging the photodissociation dynamics of neutral metal clusters: copper dimer, Cu_2, and copper oxide, CuO. *Physical Chemistry Chemical Physics*, 16(2):458–466, 2014.

[67] W. Schöllkopf, S. Gewinner, W. Erlebach, G. Heyne, H. Junkes, A. Liedke, G. Meijer, A. Paarmann, G. von Helden, H. Bluem, et al. The new IR FEL facility at the Fritz-Haber-Institut in Berlin. In *36th International Free Electron Laser Conference*, pages 629–634, 2015.

[68] W. Schöllkopf, S. Gewinner, H. Junkes, A. Paarmann, G. von Helden, H. P. Bluem, and A. M. Todd. The new IR and THz FEL facility at the Fritz Haber Institute in Berlin. In *Advances in X-ray Free-Electron Lasers Instrumentation III*, volume 9512, page 95121L. International Society for Optics and Photonics, 2015.

[69] C. Walther, S. Becker, G. Dietrich, H. J. Kluge, M. Lindinger, K. Lützenkirchen, L. Schweikhard, and J. Ziegler. Photo fragmentation of metal clusters stored in a Penning trap. *Zeitschrift für Physik D Atoms, Molecules and Clusters*, 38(1):51–58, 1996.

[70] M. Born and R. Oppenheimer. Zur quantentheorie der molekeln. *Annalen der Physik*, 389(20):457–484, 1927.

[71] P. Hohenberg and W. Kohn. Inhomogeneous electron gas. *Physical review*, 136(3B):B864–B871, 1964.

[72] W. Kohn and L. J. Sham. Self-consistent equations including exchange and correlation effects. *Phys. Rev.*, 140:A1133–A1138, Nov 1965.

[73] D. R. Hartree. The wave mechanics of an atom with a non-coulomb central field. part ii. some results and discussion. *Mathematical Proceedings of the Cambridge Philosophical Society*, 24(1):111–132, 1928.

[74] L. Goerigk and S. Grimme. A thorough benchmark of density functional methods for general main group thermochemistry, kinetics, and noncovalent interactions. *Physical Chemistry Chemical Physics*, 13(14):6670–6688, 2011.

[75] A. V. Arbuznikov. Hybrid exchange correlation functionals and potentials: Concept elaboration. *Journal of Structural Chemistry*, 48(1):S1–S31, 2007.

[76] F. Weigend and R. Ahlrichs. Balanced basis sets of split valence, triple zeta valence and quadruple zeta valence quality for H to Rn: Design and assessment of accuracy. *Physical Chemistry Chemical Physics*, 7(18):3297–3305, 2005.

[77] F. Weigend. Accurate Coulomb-fitting basis sets for H to Rn. *Physical Chemistry Chemical Physics*, 8(9):1057–1065, 2006.

[78] J. Pérez-Ramırez, F. Kapteijn, K. Schöffel, and J. A. Moulijn. Formation and control of N_2O in nitric acid production: where do we stand today? *Applied Catalysis B: Environmental*, 44(2):117–151, 2003.

[79] D. Fahey, P. A. Newman, J. A. Pyle, B. Safari, M. P. Chipperfield, D. Karoly, D. E. Kinnison, M. Ko, M. Santee, and S. J. Doherty. Scientific assessment of ozone depletion: 2018, global ozone research and monitoring project-report no. 58, 2018.

[80] A. R. Ravishankara, J. S. Daniel, and R. W. Portmann. Nitrous oxide (N_2O): the dominant ozone-depleting substance emitted in the 21st century. *Science*, 326(5949):123–125, 2009.

[81] A. Ajavon, J. Bornman, B. Maranion, N. Paul, M. Pizano, P. Newman, J. Pyle, A. Ravishankara, M. Shao, and A. Woodcock. Synthesis of the 2014 reports of the scientific, environmental effects, and technology and economic assessment panels of the montreal protocol, 2015.

[82] V. Rosca, M. Duca, M. T. de Groot, and M. T. M. Koper. Nitrogen cycle electrocatalysis. *Chemical Reviews*, 109(6):2209–2244, 2009.

[83] G. Chinchen, P. Davies, and R. J. Sampson. The historical development of catalytic oxidation processes. In *Catalysis*, volume 8, pages 1–67. Springer, 1987.

[84] R. C. Stempel and S. W. Martens. Fuel economy trends and catalytic devices. *SAE Transactions*, pages 2358–2372, 1974.

[85] A. Cho. Connecting the dots to custom catalysts. *Science*, 299(5613):1684–1685, 2003.

[86] A. Ulvestad, A. Singer, J. N. Clark, H. M. Cho, J. W. Kim, R. Harder, J. Maser, Y. S. Meng, and O. G. Shpyrko. Topological defect dynamics in operando battery nanoparticles. *Science*, 348(6241):1344–1347, 2015.

[87] M. B. Knickelbein. Reactions of transition metal clusters with small molecules. *Annual review of physical chemistry*, 50(1):79–115, 1999.

[88] D. J. Trevor, R. L. Whetten, D. M. Cox, and A. Kaldor. Gas phase platinum cluster reactions with benzene and several hexanes: evidence of extensive dehydrogenation and size-dependent chemisorption. *Journal of the American Chemical Society*, 107(2):518–519, 1985.

[89] D. J. Trevor, D. M. Cox, and A. Kaldor. Methane activation on unsupported platinum clusters. *Journal of the American Chemical Society*, 112(10):3742–3749, 1990.

[90] T. Hanmura, M. Ichihashi, and T. Kondow. Dehydrogenation of simple hydrocarbons on platinum cluster ions. *The Journal of Physical Chemistry A*, 106(47):11465–11469, 2002.

[91] G. S. Jackson, F. M. White, C. L. Hammill, R. J. Clark, and A. G. Marshall. Gas-phase dehydrogenation of saturated and aromatic cyclic hydrocarbons by Pt_n^+ (n = 1-4). *Journal of the American Chemical Society*, 119(32):7567–7572, 1997.

[92] C. Adlhart and E. Uggerud. Mechanisms for the dehydrogenation of alkanes on platinum: Insights gained from the reactivity of gaseous cluster cations, Pt_n^+ n = 1–21. *Chemistry–A European Journal*, 13(24):6883–6890, 2007.

[93] C. Adlhart and E. Uggerud. Reactions of platinum clusters $Pt_n^{\pm}$, n = 1–21, with CH_4: to react or not to react. *Chemical Communications*, pages 2581–2582, 2006.

[94] U. Achatz, C. Berg, S. Joos, B. S. Fox, M. K. Beyer, G. Niedner-Schatteburg, and V. E. Bondybey. Methane activation by platinum cluster ions in the gas phase: effects of cluster charge on the Pt_4 tetramer. *Chemical Physics Letters*, 320(1-2):53–58, 2000.

[95] M. Andersson and A. Rosén. Catalytic oxidation of hydrogen on free platinum clusters. *The Journal of Chemical Physics*, 117(15):7051–7054, 2002.

[96] H. Yamamoto, K. Miyajima, T. Yasuike, and F. Mafuné. Reactions of neutral platinum clusters with N_2O and CO. *The Journal of Physical Chemistry A*, 117(47):12175–12183, 2013.

[97] K. Koszinowski, D. Schröder, and H. Schwarz. Reactivity of small cationic platinum clusters. *The Journal of Physical Chemistry A*, 107(25):4999–5006, 2003.

[98] I. Balteanu, O. P. Balaj, M. K. Beyer, and V. E. Bondybey. Reactions of platinum clusters $^{195}Pt_n^{\pm}$, n = 1–24, with N_2O studied with isotopically enriched platinum. *Physical Chemistry Chemical Physics*, 6(11):2910–2913, 2004.

[99] P. A. Hintz and K. M. Ervin. Chemisorption and oxidation reactions of nickel group cluster anions with N_2, O_2, CO_2, and N_2O. *The Journal of Chemical Physics*, 103(18):7897–7906, 1995.

[100] L. L. Lv, Y. C. Wang, Q. Wang, and H. W. Liu. Why is Pt_4^+ the least efficient cationic cluster in activating the C-H bond in methane? two-state reaction computational investigation. *The Journal of Physical Chemistry C*, 114(41):17610–17620, 2010.

[101] P. Ferrari, K. Hansen, P. Lievens, and E. Janssens. Stability of small cationic platinum clusters. *Physical Chemistry Chemical Physics*, 20(46):29085–29090, 2018.

[102] A. E. Green, J. Justen, W. Schöllkopf, A. S. Gentleman, A. Fielicke, and S. R. Mackenzie. IR signature of size-selective CO_2 activation on small platinum cluster anions, Pt_n^- (n = 4–7). *Angewandte Chemie*, 130(45):15038–15042, 2018.

[103] Y. Shi and K. M. Ervin. Catalytic oxidation of carbon monoxide by platinum cluster anions. *The Journal of Chemical Physics*, 108(5):1757–1760, 1998.

[104] E. M. Cunningham, A. S. Gentleman, P. W. Beardsmore, A. Iskra, and S. R. Mackenzie. Infrared signature of structural isomers of gas–phase $M^+(N_2O)_n$ (M = Cu, Ag, Au) ion–molecule complexes. *The Journal of Physical Chemistry A*, 121(40):7565–7571, 2017.

[105] E. M. Cunningham, A. S. Gentleman, P. W. Beardsmore, and S. R. Mackenzie. Structural isomers and low-lying electronic states of gas-phase $M^+(N_2O)_n$ (M = Co, Rh, Ir) ion–molecule complexes. *Phys. Chem. Chem. Phys.*, 21:13959–13967, 2019.

[106] E. M. Cunningham, A. S. Gentleman, P. W. Beardsmore, and S. R. Mackenzie. Infrared spectroscopy of closed *s*-shell gas-phase $M^+(N_2O)$ n (M = Li, Al) ion-molecule complexes. *Molecular Physics*, 117(21):2990–3000, 2019.

[107] E. M. Cunningham. Elucidating the structures of cationic metal-nitrous oxide complexes using infrared action spectroscopy. DPhil Thesis, University of Oxford, 2019.

[108] S. M. Hamilton, W. S. Hopkins, D. J. Harding, T. R. Walsh, M. Haertelt, C. Kerpal, P. Gruene, G. Meijer, A. Fielicke, and S. R. Mackenzie. Infrared-induced reactivity of N_2O on small gas-phase rhodium clusters. *The Journal of Physical Chemistry A*, 115(12):2489–2497, 2011.

[109] S. M. Hamilton, W. S. Hopkins, D. J. Harding, T. R. Walsh, P. Gruene, M. Haertelt, A. Fielicke, G. Meijer, and S. R. Mackenzie. Infrared induced reactivity on the surface of isolated size-selected clusters: dissociation of N_2O on rhodium clusters. *Journal of the American Chemical Society*, 132(5):1448–1449, 2010.

[110] A. C. Hermes, S. M. Hamilton, W. S. Hopkins, D. J. Harding, C. Kerpal, G. Meijer, A. Fielicke, and S. R. Mackenzie. Effects of coadsorbed oxygen on the infrared driven decomposition of N_2O on isolated Rh_5^+ clusters. *The Journal of Physical Chemistry Letters*, 2(24):3053–3057, 2011.

[111] I. S. Parry, A. Kartouzian, S. M. Hamilton, O. P. Balaj, M. K. Beyer, and S. R. Mackenzie. Chemical reactivity on gas-phase metal clusters driven by blackbody infrared radiation. *Angewandte Chemie International Edition*, 54(4):1357–1360, 2015.

[112] I. S. Parry, A. Kartouzian, S. M. Hamilton, O. P. Balaj, M. K. Beyer, and S. R. Mackenzie. Collisional activation of N_2O decomposition and CO oxidation reactions on isolated rhodium clusters. *The Journal of Physical Chemistry A*, 117(36):8855–8863, 2013.

[113] G. von Helden, D. van Heijnsbergen, and G. Meijer. Resonant ionization using IR light: A new tool to study the spectroscopy and dynamics of gas-phase molecules and clusters. *The Journal of Physical Chemistry A*, 107(11):1671–1688, 2003.

[114] B. Simard, S. Dénommée, D. M. Rayner, D. van Heijnsbergen, G. Meijer, and G. von Helden. IR multiphoton depletion spectroscopy of metal cluster–ligand complexes. *Chemical Physics Letters*, 357(3-4):195–203, 2002.

[115] A. Fielicke, G. von Helden, G. Meijer, D. B. Pedersen, B. Simard, and D. M. Rayner. Size and charge effects on the binding of CO to small isolated rhodium clusters. *The Journal of Physical Chemistry B*, 108(38):14591–14598, 2004.

[116] V. N. Staroverov, G. E. Scuseria, J. Tao, and J. P. Perdew. Comparative assessment of a new nonempirical density functional: Molecules and hydrogen-bonded complexes. *The Journal of Chemical Physics*, 119(23):12129–12137, 2003.

[117] J. Tao, J. P. Perdew, V. N. Staroverov, and G. E. Scuseria. Climbing the density functional ladder: Nonempirical meta–generalized gradient approximation designed for molecules and solids. *Physical Review Letters*, 91(14):146401, 2003.

[118] M. J. Frisch, G. W. Trucks, H. B. Schlegel, G. E. Scuseria, M. A. Robb, J. R. Cheeseman, G. Scalmani, V. Barone, G. A. Petersson, H. Nakatsuji, X. Li, M. Caricato, A. V. Marenich, J. Bloino, B. G. Janesko, R. Gomperts, B. Mennucci, H. P. Hratchian, J. V. Ortiz, A. F. Izmaylov, J. L. Sonnenberg, D. Williams-Young, F. Ding, F. Lipparini, F. Egidi, J. Goings, B. Peng, A. Petrone, T. Henderson, D. Ranasinghe, V. G. Zakrzewski, J. Gao, N. Rega, G. Zheng, W. Liang, M. Hada, M. Ehara, K. Toyota, R. Fukuda, J. Hasegawa, M. Ishida, T. Nakajima, Y. Honda, O. Kitao, H. Nakai, T. Vreven, K. Throssell, J. A. Montgomery, Jr., J. E. Peralta, F. Ogliaro, M. J. Bearpark, J. J. Heyd, E. N. Brothers, K. N. Kudin, V. N. Staroverov, T. A. Keith, R. Kobayashi, J. Normand, K. Raghavachari, A. P. Rendell, J. C. Burant, S. S. Iyengar, J. Tomasi, M. Cossi, J. M. Millam, M. Klene, C. Adamo, R. Cammi, J. W. Ochterski, R. L. Martin, K. Morokuma, O. Farkas, J. B. Foresman, and D. J. Fox. Gaussian~16 Revision A.03, 2016. Gaussian Inc. Wallingford CT.

[119] K. P. Jensen. Metal- ligand bonds of second-and third-row *d*-block metals characterized by density functional theory. *The Journal of Physical Chemistry A*, 113(37):10133–10141, 2009.

[120] A. C. Hermes, S. M. Hamilton, G. A. Cooper, C. Kerpal, D. J. Harding, G. Meijer, A. Fielicke, and S. R. Mackenzie. Infrared driven CO oxidation reactions on isolated platinum cluster oxides, $Pt_nO_m^+$. *Faraday discussions*, 157:213–225, 2012.

[121] A. Fielicke, P. Gruene, M. Haertelt, D. J. Harding, and G. Meijer. Infrared spectroscopy and binding geometries of oxygen atoms bound to cationic tantalum clusters. *The Journal of Physical Chemistry A*, 114(36):9755–9761, 2010.

[122] D. J. Harding, C. Kerpal, D. M. Rayner, and A. Fielicke. Communication: The structures of small cationic gas-phase platinum clusters. *The Journal of Chemical Physics*, 136(21):211103, 2012.

[123] S. Grimme, S. Ehrlich, and L. Goerigk. Effect of the damping function in dispersion corrected density functional theory. *Journal of computational chemistry*, 32(7):1456–1465, 2011.

[124] D. Andrae, U. Haeussermann, M. Dolg, H. Stoll, and H. Preuss. Energy-adjusted ab initio pseudopotentials for the second and third row transition elements. *Theoretica chimica acta*, 77(2):123–141, 1990.

[125] G. Herzberg. *Molecular Spectra and Molecular Structure: II Infrared and Raman Spectra of Polyatomic Molecules*, volume 2. Krieger, Malabar, Florida, 1991.

[126] K. Fukui. The path of chemical reactions-the IRC approach. *Accounts of Chemical Research*, 14(12):363–368, 1981.

[127] H. P. Hratchian and H. B. Schlegel. Finding minima, transition states, and following reaction pathways on ab initio potential energy surfaces. In *Theory and applications of computational chemistry*, pages 195–249. Elsevier, 2005.

[128] C. Kerpal, D. J. Harding, A. C. Hermes, G. Meijer, S. R. Mackenzie, and A. Fielicke. Structures of platinum oxide clusters in the gas phase. *The Journal of Physical Chemistry A*, 117(6):1233–1239, 2013.

[129] G. Dietrich, K. Lützenkirchen, S. Becker, H. U. Hasse, H. J. Kluge, M. Lindinger, L. Schweikhard, J. Ziegler, and S. Kuznetsov. Au-induced decomposition of N_2O. *Berichte der Bunsengesellschaft für physikalische Chemie*, 98(12):1608–1612, 1994.

[130] P. Ferrari, G. L. Hou, O. V. Lushchikova, F. Calvo, J. M. Bakker, and E. Janssens. The structures of cationic gold clusters probed by far-infrared spectroscopy. *Phys. Chem. Chem. Phys.*, 22:11572–11577, 2020.

[131] S. Gilb, P. Weis, F. Furche, R. Ahlrichs, and M. M. Kappes. Structures of small gold cluster cations (Au_n^+, $n < 14$): Ion mobility measurements versus density functional calculations. *The Journal of Chemical Physics*, 116(10):4094–4101, 2002.

[132] H. Häkkinen, B. Yoon, U. Landman, X. Li, H. J. Zhai, and L. S. Wang. On the electronic and atomic structures of small Au_n^- (n = 4- 14) clusters: a photoelectron spectroscopy and density-functional study. *The Journal of Physical Chemistry A*, 107(32):6168–6175, 2003.

[133] L. M. Ghiringhelli, P. Gruene, J. T. Lyon, D. M. Rayner, G. Meijer, A. Fielicke, and M. Scheffler. Not so loosely bound rare gas atoms: finite-temperature vibrational fingerprints of neutral gold-cluster complexes. *New Journal of Physics*, 15(8):083003, aug 2013.

[134] B. R. Goldsmith, J. Florian, J. X. Liu, P. Gruene, J. T. Lyon, D. M. Rayner, A. Fielicke, M. Scheffler, and L. M. Ghiringhelli. Two-to-three dimensional transition in neutral gold clusters: The crucial role of van der waals interactions and temperature. *Phys. Rev. Materials*, 3:016002, Jan 2019.

[135] P. Gruene, B. Butschke, J. T. Lyon, D. M. Rayner, and A. Fielicke. Far-IR spectra of small neutral gold clusters in the gas phase. *Zeitschrift für Physikalische Chemie*, 228(4-5):337–350, 2014.

[136] H. Häkkinen, M. Moseler, and U. Landman. Bonding in Cu, Ag, and Au clusters: Relativistic effects, trends, and surprises. *Phys. Rev. Lett.*, 89:033401, Jun 2002.

[137] H. Grönbeck and P. Broqvist. Comparison of the bonding in au_8 and cu_8: A density functional theory study. *Phys. Rev. B*, 71:073408, Feb 2005.

[138] V. Bonačić-Koutecký, J. Pittner, C. Fuchs, P. Fantucci, M. F. Guest, and J. Koutecký. Ab initio predictions of structural and optical response properties of Na_n^+ clusters: Interpretation of depletion spectra at low temperature. *The Journal of Chemical Physics*, 104(4):1427–1440, 1996.

[139] K. S. Pitzer. Relativistic effects on chemical properties. *Accounts of Chemical Research*, 12(8):271–276, 1979.

[140] P. Pyykkö. Relativistic quantum chemistry. In P. O. Löwdin, editor, *Advances in quantum chemistry*, volume 11 of *Advances in Quantum Chemistry*, pages 353–409. Academic Press, 1978.

[141] M. L. Anderson, A. Lacz, T. Drewello, P. J. Derrick, D. P. Woodruff, and S. R. Mackenzie. The chemistry of nitrogen oxides on small size-selected cobalt clusters, Co_n^+. *The Journal of Chemical Physics*, 130(6):064305, 2009.

[142] S. Hirabayashi, M. Ichihashi, and T. Kondow. Reactions of copper cluster cations with nitrous oxide: Oxidation and sequential N_2O adsorption. *Chemical Physics Letters*, 533:15–19, 2012.

[143] R. Gehrke, P. Gruene, A. Fielicke, G. Meijer, and K. Reuter. Nature of ar bonding to small co n+ clusters and its effect on the structure determination by far-infrared absorption spectroscopy. *The Journal of Chemical Physics*, 130(3):034306, 2009.

[144] M. Jia, J. Van der Tol, Y. Li, V. Chernyy, J. M. Bakker, L. N. Pham, M. T. Nguyen, and E. Janssens. Structures and magnetic properties of small and con-1cr+ (n= 3–5) clusters. *Journal of Physics: Condensed Matter*, 30(47):474002, 2018.

[145] M. J. Frisch, G. W. Trucks, H. B. Schlegel, G. E. Scuseria, M. A. Robb, J. R. Cheeseman, G. Scalmani, V. Barone, B. Mennucci, G. A. Petersson, H. Nakatsuji, M. Caricato, X. Li, H. P. Hratchian, A. F. Izmaylov, J. Bloino, G. Zheng, J. L. Sonnenberg, M. Hada, M. Ehara, K. Toyota, R. Fukuda, J. Hasegawa, M. Ishida, T. Nakajima, Y. Honda, O. Kitao, H. Nakai, T. Vreven, J. A. Montgomery, J. E. Peralta, F. Ogliaro, M. Bearpark, J. J. Heyd, E. Brothers, K. N. Kudin, V. N. Staroverov, R. Kobayashi, J. Normand, K. Raghavachari, A. Rendell, J. C. Burant, S. S. Iyengar, J. Tomasi, M. Cossi, N. Rega, J. M. Millam, M. Klene, J. E. Knox, J. B. Cross, V. Bakken, C. Adamo, J. Jaramillo, R. Gomperts, R. E. Stratmann, O. Yazyev, A. J. Austin, R. Cammi, C. Pomelli, J. W. Ochterski, R. L. Martin, K. Morokuma, V. G. Zakrzewski, G. A. Voth, P. Salvador, J. J. Dannenberg, S. Dapprich, A. D. Daniels, O. Farkas, J. B. Foresman, J. V. Ortiz, J. Cioslowski, and D. J. Fox. Gaussian 09, revision d.01. *Gaussian 09, Revision D.01, Gaussian, Inc., Wallingford CT*, 2009.

[146] A. P. Woodham, G. Meijer, and A. Fielicke. Activation of molecular oxygen by anionic gold clusters. *Angewandte Chemie International Edition*, 51(18):4444–4447, 2012.

[147] A. Fielicke, G. von Helden, G. Meijer, B. Simard, and D. M. Rayner. Gold cluster carbonyls: vibrational spectroscopy of the anions and the effects of cluster size, charge, and coverage on the CO stretching frequency. *The Journal of Physical Chemistry B*, 109(50):23935–23940, 2005.

[148] M. Haruta, N. Yamada, T. Kobayashi, and S. Iijima. Gold catalysts prepared by coprecipitation for low-temperature oxidation of hydrogen and of carbon monoxide. *Journal of Catalysis*, 115(2):301–309, 1989.

[149] R. Meyer, C. Lemire, S. K. Shaikhutdinov, and H. J. Freund. Surface chemistry of catalysis by gold. *Gold Bulletin*, 37(1):72–124, 2004.

[150] R. R. Buchholz, H. M. Worden, M. Park, G. Francis, M. N. Deeter, D. P. Edwards, L. K. Emmons, B. Gaubert, J. Gille, S. Martínez-Alonso, W. Tang, R. Kumar, J. R. Drummond, C. Clerbaux, M. George, P. F. Coheur, D. Hurtmans, K. W. Bowman, M. Luo, V. H. Payne, J. R. Worden, M. Chin, R. C. Levy, J. Warner, Z. Wei, and S. S. Kulawik. Air pollution

trends measured from Terra: CO and AOD over industrial, fire-prone, and background regions. *Remote Sensing of Environment*, 256:112275, 2021.

[151] J. E. Kloeppel. A sensitive technique for measuring hydroxyl radicals, atmospheric cleansing molecules. *Environmental Health Perspectives*, 101(2):123–125, 1993.

[152] G. Reumuth, Z. Alharbi, K. S. Houschyar, B. S. Kim, F. Siemers, P. C. Fuchs, and G. Grieb. Carbon monoxide intoxication: What we know. *Burns*, 45(3):526–530, 2019.

[153] M. P. Johansson, A. Lechtken, D. Schooss, M. M. Kappes, and F. Furche. 2d-3D transition of gold cluster anions resolved. *Physical Review A*, 77(5):053202, 2008.

[154] B. E. Salisbury, W. T. Wallace, and R. L. Whetten. Low-temperature activation of molecular oxygen by gold clusters: a stoichiometric process correlated to electron affinity. *Chemical Physics*, 262(1):131–141, 2000.

[155] R. Pal, L. M. Wang, Y. Pei, L. S. Wang, and X. C. Zeng. Unraveling the mechanisms of O_2 activation by size-selected gold clusters: Transition from superoxo to peroxo chemisorption. *Journal of the American Chemical Society*, 134(22):9438–9445, 2012.

[156] B. Yoon, H. Häkkinen, and U. Landman. Interaction of O_2 with gold clusters: molecular and dissociative adsorption. *The Journal of Physical Chemistry A*, 107(20):4066–4071, 2003.

[157] G. Blyholder. Molecular orbital view of chemisorbed carbon monoxide. *The Journal of Physical Chemistry*, 68(10):2772–2777, 1964.

[158] A. S. Goldman and K. Krogh-Jespersen. Why do cationic carbon monoxide complexes have high C O stretching force constants and short C O bonds? electrostatic effects, not σ-bonding. *Journal of the American Chemical Society*, 118(48):12159–12166, 1996.

[159] J. France and P. Hollins. Interactions of CO molecules adsorbed on gold. *Journal of Electron Spectroscopy and Related Phenomena*, 64-65:251–258, 1993.

[160] X. Wu, L. Senapati, S. K. Nayak, A. Selloni, and M. Hajaligol. A density functional study of carbon monoxide adsorption on small cationic, neutral, and anionic gold clusters. *The Journal of Chemical Physics*, 117(8):4010–4015, 2002.

[161] D. W. Yuan and Z. Zeng. Saturated adsorption of CO and coadsorption of CO and O_2 on Au_N (N = 2–7) clusters. *The Journal of Chemical Physics*, 120(14):6574–6584, 2004.

[162] H. Häkkinen and U. Landman. Gas-phase catalytic oxidation of CO by Au_2^-. *Journal of the American Chemical Society*, 123(39):9704–9705, 2001.

[163] H. Liu, X. Xing, X. Wang, H. Qu, G. J. Wang, and M. F. Zhou. Co-adsorption of O_2 and CO on Au_2: Infrared photodissociation spectroscopy and theoretical study of $[Au_2O_2(CO)_n]$ (n = 2-6). *Chemistry – A European Journal*, 22(6):2085–2091, 2016.

[164] L. D. Socaciu, J. Hagen, T. M. Bernhardt, L. Wöste, U. Heiz, H. Häkkinen, and U. Landman. Catalytic CO oxidation by free Au_2^-: experiment and theory. *Journal of the American Chemical Society*, 125(34):10437–10445, 2003.

[165] R. A. Kendall, T. H. Dunning, and R. J. Harrison. Electron affinities of the first row atoms revisited. systematic basis sets and wave functions. *The Journal of Chemical Physics*, 96(9):6796–6806, 1992.

[166] G. Herzberg. *Molecular Spectra and Molecular Structure: I Spectra of Diatomic Molecules*, volume 1. Krieger, Malabar, Florida, 1989.

[167] R. S. Mulliken. Electronic population analysis on LCAO–MO molecular wave functions. i. *The Journal of Chemical Physics*, 23(10):1833–1840, 1955.

[168] E. R. Davidson and S. Chakravorty. A test of the Hirshfeld definition of atomic charges and moments. *Theoretica chimica acta*, 83(5):319–330, 1992.

[169] M. D. Segall, C. J. Pickard, R. Shah, and M. C. Payne. Population analysis in plane wave electronic structure calculations. *Molecular Physics*, 89(2):571–577, 1996.

[170] F. L. Hirshfeld. Bonded-atom fragments for describing molecular charge densities. *Theoretica chimica acta*, 44(2):129–138, 1977.

[171] P. M. Mannucci, S. Harari, I. Martinelli, and M. Franchini. Effects on health of air pollution: a narrative review. *Internal and emergency medicine*, 10(6):657–662, 2015.

[172] R. J. Blaszczak. Nitrogen oxides (NO_x): Why and how they are controlled; EPA-456/F-99-006R, 1999.

[173] M. Lenner. Nitrogen dioxide in exhaust emissions from motor vehicles. *Atmospheric Environment (1967)*, 21(1):37–43, 1987.

[174] S. Gligorovski, R. Strekowski, S. Barbati, and D. Vione. Addition and correction to environmental implications of hydroxyl radicals (·OH). *Chemical Reviews*, 118(4):2296–2296, 2018.

[175] D. E. Koshland Jr. The molecule of the year. *Science*, 258(5090):1861–1861, 1992.

[176] G. B. Richter-Addo, P. Legzdins, and J. Burstyn. Introduction: nitric oxide chemistry. *Chemical Reviews*, 102(4):857–860, 2002.

[177] J. Kašpar, P. Fornasiero, and N. Hickey. Automotive catalytic converters: current status and some perspectives. *Catalysis today*, 77(4):419–449, 2003.

[178] K. Hiraoka, M. Nasu, D. Oomori, and A. Minamitsu. Bond energy oscillation in the cluster ion $NO^+(NO)_n$. *The Journal of Chemical Physics*, 105(20):9068–9071, 1996.

[179] S. R. Desai, C. S. Feigerle, and J. C. Miller. Laser ionization mass spectrometry of homogeneous and binary molecular clusters of nitric oxide. *The Journal of Chemical Physics*, 101(6):4526–4535, 1994.

[180] L. Poth, Z. Shi, Q. Zhong, and A. W. Castleman. Metastable dissociation study of nitric oxide clusters. *The Journal of Physical Chemistry A*, 101(6):1099–1103, 1997.

[181] M. E. Jacox and W. E. Thompson. The vibrational spectra of molecular ions isolated in solid neon. iv. NO^+, NO^-, $ONNO^+$, and $ONNO^-$. *The Journal of Chemical Physics*, 93(11):7609–7621, 1990.

[182] A. Strobel, N. Knoblauch, J. Agreiter, A. M. Smith, G. Niedner-Schatteburg, and V. E. Bondybey. Identification, structure, and vibrational assignment of the NO dimer cation. *The Journal of Physical Chemistry*, 99(3):872–874, 1995.

[183] C. L. Lugez, W. E. Thompson, M. E. Jacox, A. Snis, and I. Panas. Infrared spectra of $(NO)_2^+$, $(NO)_2^-$, and $(NO)_3^-$ trapped in solid neon. *The Journal of Chemical Physics*, 110(21):10345–10358, 1999.

[184] L. Andrews and M. F. Zhou. Infrared spectra of $(NO)_2^-$ and $(NO)_2^+$ isomers trapped in solid neon. *The Journal of Chemical Physics*, 111(13):6036–6041, 1999.

[185] F. Legay and N. Legay-Sommaire. NO diffusion and dimer formation in a nitrogen matrix studied by FTIR spectroscopy. *Chemical Physics Letters*, 211(6):516–522, 1993.

[186] R. Kometer, F. Legay, N. Legay-Sommaire, and N. Schwentner. Vibrational spectroscopy of NO and $(NO)_2$ isolated in solid neon. *The Journal of Chemical Physics*, 100(12):8737–8745, 1994.

[187] J. F. Canty, E. G. Stone, S. B. H. Bach, and D. W. Ball. Matrix isolation and theoretical studies of ONNO: Assignment of a new combination band and density functional calculations. *Chemical Physics*, 216(1-2):81–89, 1997.

[188] J. Hacaloglu, S. Suzer, and L. Andrews. Chemical ionization discharge of nitrogen oxide for matrix infrared spectroscopic study of isolated anions. *Journal of Physical Chemistry*, 94(5):1759–1764, 1990.

[189] L. Andrews, M. F. Zhou, S. P. Willson, G. P. Kushto, A. Snis, and I. Panas. Infrared spectra of cis and trans-$(NO)_2^-$ anions in solid argon. *The Journal of Chemical Physics*, 109(1):177–185, 1998.

[190] C. E. Dinerman and G. E. Ewing. Infrared spectrum, structure, and heat of formation of gaseous $(NO)_2$. *The Journal of Chemical Physics*, 53(2):626–631, 1970.

[191] G. E. Ewing. Intermolecular interactions: van der Waals molecules. *Angewandte Chemie International Edition in English*, 11(6):486–495, 1972.

[192] A. R. W. McKellar, J. K. G. Watson, and B. J. Howard. The NO dimer: ^{15}N isotopic infrared spectra, line-widths, and force field. *Molecular Physics*, 86(2):273–286, 1995.

[193] A. Dkhissi, P. Soulard, A. Perrin, and N. Lacome. The NO dimer. *Journal of Molecular Spectroscopy*, 183(1):12–17, 1997.

[194] J. K. G. Watson and A. R. W. Mckellar. The ν_5 band of the NO dimer. *Canadian journal of physics*, 75(3):181–189, 1997.

[195] E. P. F. Lee and T. G. Wright. The cis and trans structures of the NO dimer cation. *Chemical Physics Letters*, 301(5-6):467–473, 1999.

[196] A. L. L. East and J. K. G. Watson. On the photoelectron spectrum of the NO dimer, and the ground state of $(NO)_2^+$. *The Journal of Chemical Physics*, 110(13):6099–6102, 1999.

[197] Y. Xie, H. F. Schaefer III, X. Y. Fu, and R. Z. Liu. The infrared spectrum of the nitric oxide dimer cation: Problems for density functional theory and a muddled relationship to experiment. *The Journal of Chemical Physics*, 111(6):2532–2541, 1999.

[198] Y. Xie and H. F. Schaefer III. The puzzling infrared spectra of the nitric oxide dimer radical cation: a systematic application of Brueckner methods. *Molecular Physics*, 98(14):955–959, 2000.

[199] T. K. Ha. Ab initio CI study of the nitric oxide dimer (N_2O_2). *Theoretica chimica acta*, 58(2):125–130, 1981.

[200] T. J. Lee, A. P. Rendell, and P. R. Taylor. Comparison of the quadratic configuration interaction and coupled-cluster approaches to electron correlation including the effect of triple excitations. *Journal of Physical Chemistry*, 94(14):5463–5468, 1990.

[201] R. González-Luque, M. Merchán, and B. O. Roos. A theoretical determination of the dissociation energy of the nitric oxide dimer. *Theoretica chimica acta*, 88(6):425–435, 1994.

[202] B. S. Jursic and Z. Zdravkovski. Theoretical investigation of cis-and trans-nitric oxide dimers with ab initio and density functional Gaussian-type orbital approach. *International Journal of Quantum Chemistry*, 54(3):161–166, 1995.

[203] A. L. L. East. The 16 valence electronic states of nitric oxide dimer $(NO)_2$. *Journal of Chemical Physics*, 109(6):2185–2193, 1998.

[204] H. Zhang, G. L. Zheng, G. Lv, Y. Z. Geng, and Q. Ji. Covalent intermolecular interaction of the nitric oxide dimer $(NO)_2$. *Chinese Physics B*, 24(9):093101, 2015.

[205] B. Urban, A. Strobel, and V. E. Bondybey. The $(NO)_2$ dimer and its ions: Is the solution near? *The Journal of Chemical Physics*, 111(19):8939–8949, 1999.

[206] H. Hoshina, M. Slipchenko, K. Prozument, D. Verma, M. W. Schmidt, J. Ivanic, and A. F. Vilesov. Infrared spectroscopy and structure of $(NO)_n$ clusters. *The Journal of Physical Chemistry A*, 120(4):527–534, 2016.

[207] G. K. Ruschel, T. M. Nemetz, and D. W. Ball. Matrix isolation and density functional studies of novel transition metal complexes. NO^+ Fe, Co, Ni, Cu, and Zn in argon matrices. *Journal of molecular structure*, 384(2-3):101–114, 1996.

[208] V. Blagojevic, E. Flaim, M. J. Y. Jarvis, G. K. Koyanagi, and D. K. Bohme. Nitric oxide as an electron donor, an atom donor, an atom acceptor, and a ligand in reactions with atomic transition-metal and main-group cations in the gas phase. *The Journal of Physical Chemistry A*, 109(49):11224–11235, 2005.

[209] A. Shiotari, H. Koshida, and H. Okuyama. Adsorption and valence electronic states of nitric oxide on metal surfaces. *Surface Science Reports*, 76(1):100500, 2021.

[210] C. Blanchet, H. A. Duarte, and D. R. Salahub. Density functional study of mononitrosyls of first-row transition-metal atoms. *The Journal of Chemical Physics*, 106(21):8778–8787, 1997.

[211] J. L. C. Thomas, C. W. Bauschlicher, and M. B. Hall. Binding of nitric oxide to first-transition-row metal cations: an ab initio study. *The Journal of Physical Chemistry A*, 101(45):8530–8539, 1997.

[212] J. J. Klaassen and D. B. Jacobson. Dissociative versus molecular chemisorption of nitric oxide on small bare cationic cobalt clusters in the gas phase. *Journal of the American Chemical Society*, 110(3):974–976, 1988.

[213] M. E. Bridge and R. M. Lambert. Adsorption and reactivity of nitric oxide on Co (0001). *Surface Science*, 94(2-3):469–482, 1980.

[214] T. Hanmura, M. Ichihashi, Y. Watanabe, N. Isomura, and T. Kondow. Reactions of nitrogen monoxide on cobalt cluster ions: reaction enhancement by introduction of hydrogen. *The Journal of Physical Chemistry A*, 111(3):422–428, 2007.

[215] T. Hanmura, M. Ichihashi, R. Okawa, and T. Kondow. Size-dependent reactivity of cobalt cluster ions with nitrogen monoxide: Competition between chemisorption and decomposition of NO. *International Journal of Mass Spectrometry*, 280(1-3):184–189, 2009.

[216] M. S. Ford, M. L. Anderson, M. P. Barrow, D. P. Woodruff, T. Drewello, P. J. Derrick, and S. R. Mackenzie. Reactions of nitric oxide on Rh_6^+ clusters: abundant chemistry and evidence of structural isomers. *Physical Chemistry Chemical Physics*, 7(5):975–980, 2005.

[217] M. L. Anderson, M. S. Ford, P. J. Derrick, T. Drewello, D. P. Woodruff, and S. R. Mackenzie. Nitric oxide decomposition on small rhodium clusters, $Rh_n^{+/-}$. *The Journal of Physical Chemistry A*, 110(38):10992–11000, 2006.

[218] D. J. Harding, R. D. L. Davies, S. R. Mackenzie, and T. R. Walsh. Oxides of small rhodium clusters: Theoretical investigation of experimental reactivities. *The Journal of Chemical Physics*, 129(12):124304, 2008.

[219] K. Koyama, S. Kudoh, K. Miyajima, and F. Mafuné. Thermal desorption spectroscopy study of the adsorption and reduction of NO by cobalt cluster ions under thermal equilibrium conditions at 300 K. *The Journal of Physical Chemistry A*, 119(37):9573–9580, 2015.

[220] T. Nagata, K. Koyama, S. Kudoh, K. Miyajima, J. M. Bakker, and F. Mafune. Adsorption forms of NO on Rh_n^+ (n = 6–16) revealed by infrared multiple photon dissociation spectroscopy. *The Journal of Physical Chemistry C*, 121(49):27417–27426, 2017.

[221] T. Nagata, S. Kudoh, K. Miyajima, J. M. Bakker, and F. Mafune. Adsorption of multiple NO molecules on Rh_n^+ (n = 6, 7) investigated by infrared multiple photon dissociation spectroscopy. *The Journal of Physical Chemistry C*, 122(40):22884–22891, 2018.

[222] M. Yamaguchi, Y. Zhang, S. Kudoh, K. Koyama, O. V. Lushchikova, J. M. Bakker, and F. Mafuné. Oxophilicity as a descriptor for NO cleavage efficiency over group IX metal clusters. *The Journal of Physical Chemistry Letters*, 11(11):4408–4412, 2020.

[223] Y. Zhang, M. Yamaguchi, K. Kawada, S. Kudoh, O. V. Lushchikova, J. M. Bakker, and F. Mafuné. Adsorption forms of NO on iridium-doped rhodium clusters in the gas phase revealed by infrared multiple photon dissociation spectroscopy. *The Journal of Physical Chemistry A*, 126(1):36–43, 2022.

[224] L. Andrews and A. Citra. Infrared spectra and density functional theory calculations on transition metal nitrosyls. vibrational frequencies of unsaturated transition metal nitrosyls. *Chemical Reviews*, 102(4):885–912, 2002.

[225] J. M. Bakker and F. Mafuné. Zooming in on the initial steps of catalytic NO reduction using metal clusters. *Physical Chemistry Chemical Physics*, 24(13):7595–7610, 2022.

[226] A. Mouhandes and A. J. Stace. Infrared photofragmentation of "hot" and "cold" nitric oxide cluster ions. *The Journal of Chemical Physics*, 111(21):9517–9525, 1999.

[227] M. A. Odeneye and A. J. Stace. Infrared photodissociation of $(NO)_n^+ \cdot X$ cluster ions (n 5). *Physical Chemistry Chemical Physics*, 7(5):998–1004, 2005.

[228] C. A. Woodward, J. F. Winkel, A. B. Jones, and A. J. Stace. Infrared predissociation in cluster ions containing a guest chromophore. a gentle route to the dynamics and spectroscopy of heterogeneous systems. *Chemical Physics Letters*, 206(1-4):49–56, 1993.

[229] J. F. Winkel, A. B. Jones, C. A. Woodward, D. A. Kirkwood, and A. J. Stace. Infrared laser-induced photofragmentation of the positive and negative ions of size-selected $SF_6(NO)_n$ clusters. *The Journal of Chemical Physics*, 101(11):9436–9446, 1994.

[230] S. Atrill, A. Mouhandes, J. F. Winkel, A. Goren, and A. J. Stace. Energy partitioning following the IR photofragmentation of $SF_6 \cdot (NO)_n^+$ cluster ions. *Faraday Discussions*, 102:339–351, 1995.

[231] A. Mouhandes and A. J. Stace. Infrared photofragmentation spectra of $C_2H_4 \cdot (NO)_n^+$ cluster ions. *International journal of mass spectrometry and ion processes*, 159(1-3):185–196, 1996.

[232] L. Wang, G. Wang, H. Qu, C. Wang, and M. F. Zhou. Infrared photodissociation spectroscopy of iron nitrosyl cation complexes: $Fe(NO)_n^+$ (n = 1–5). *The Journal of Physical Chemistry A*, 118(10):1841–1849, 2014.

[233] L. Wang, G. Wang, H. Qu, Z. H. Li, and M. F. Zhou. Flexible bonding between copper and nitric oxide: infrared photodissociation spectroscopy of copper nitrosyl cation complexes:$[Cu(NO)_n]^+$ (n = 1–5). *Physical Chemistry Chemical Physics*, 16(22):10788–10798, 2014.

[234] Y. Li, L. Wang, H. Qu, G. Wang, and M. F. Zhou. Infrared photodissociation spectroscopy of mass-selected silver and gold nitrosyl cation complexes. *The Journal of Physical Chemistry A*, 119(15):3577–3586, 2015.

[235] A. Iskra, A. S. Gentleman, A. Kartouzian, M. J. Kent, A. P. Sharp, and S. R. Mackenzie. Infrared spectroscopy of gas-phase $M^+(CO_2)_n$ (M = Co, Rh, Ir) ion–molecule complexes. *The Journal of Physical Chemistry A*, 121(1):133–140, 2017.

[236] A. E. Green. The infrared spectroscopy of molecular activation and reactivity on small metal clusters. DPhil Thesis, University of Oxford, 2020.

[237] J. P. Perdew. Density-functional approximation for the correlation energy of the inhomogeneous electron gas. *Phys. Rev. B*, 33:8822–8824, Jun 1986.

[238] A. D. Becke. Density-functional thermochemistry. i. the effect of the exchange-only gradient correction. *The Journal of Chemical Physics*, 96(3):2155–2160, 1992.

[239] A. D. Brathwaite, H. L. Abbott-Lyon, and M. A. Duncan. Distinctive coordination of CO vs N_2 to rhodium cations: An infrared and computational study. *The Journal of Physical Chemistry A*, 120(39):7659–7670, 2016.

[240] J. A. McCleverty. Chemistry of nitric oxide relevant to biology. *Chemical Reviews*, 104(2):403–418, 2004.

[241] J. Chatt and L. A. Duncanson. 586. olefin co-ordination compounds. part iii. infra-red spectra and structure: attempted preparation of acetylene complexes. *Journal of the Chemical Society (Resumed)*, pages 2939–2947, 1953.

[242] R. Mason. Activation of small molecules by transition metal ions and their complexes. *Nature*, 217(5128):543–545, 1968.

[243] R. S. Mulliken. Electronic population analysis on LCAO–MO molecular wave functions. ii. overlap populations, bond orders, and covalent bond energies. *The Journal of Chemical Physics*, 23(10):1841–1846, 1955.

[244] C. Y. Ng, P. W. Tiedemann, B. H. Mahan, and Y. T. Lee. The binding energy between NO and NO^+. *The Journal of Chemical Physics*, 66(9):3985–3987, 1977.

[245] J. Ivanic, M. W. Schmidt, and B. Luke. High-level theoretical study of the NO dimer and tetramer: Has the tetramer been observed? *The Journal of Chemical Physics*, 137(21):214316, 2012.

[246] O. K. Rice and H. C. Ramsperger. Theories of unimolecular gas reactions at low pressures. *Journal of the American Chemical Society*, 49(7):1617–1629, 1927.

[247] O. K. Rice and H. C. Ramsperger. Theories of unimolecular gas reactions at low pressures. ii. *Journal of the American Chemical Society*, 50(3):617–620, 1928.

[248] L. S. Kassel. Studies in homogeneous gas reactions. i. *The Journal of Physical Chemistry*, 32(2):225–242, 1928.

[249] J. Kašpar, P. Fornasiero, and N. Hickey. Automotive catalytic converters: current status and some perspectives. *Catalysis Today*, 77(4):419–449, 2003. Fundamentals of Catalysis and Applications to Environmental Problems.

[250] R. Zeng, M. Feller, Y. Diskin-Posner, L. J. W. Shimon, Y. Ben-David, and D. Milstein. CO oxidation by N_2O homogeneously catalyzed by ruthenium hydride pincer complexes indicating a new mechanism. *Journal of the American Chemical Society*, 140(23):7061–7064, 2018.

[251] M. M. Kappes and R. H. Staley. Gas-phase oxidation catalysis by transition-metal cations. *Journal of the American Chemical Society*, 103(5):1286–1287, 1981.

[252] R. W. McCabe and C. Wong. Steady-state kinetics of the CO N_2O reaction over an alumina-supported rhodium catalyst. *Journal of Catalysis*, 121(2):422–431, 1990.

[253] Q. Su, Y. Li, S. Wang, and C. Gao. Detailed mechanism for reduction of N_2O over rhodium by CO in automotive exhaust. *Topics in Catalysis*, 56(1):345–351, 2013.

[254] T. W. Dann, K. H. Schulz, M. Mann, and M. Collings. Supported rhodium catalysts for nitrous oxide decomposition in the presence of NO, CO_2, SO_2 and CO. *Applied Catalysis B: Environmental*, 6(1):1–10, 1995.

[255] V. Blagojevic, G. Orlova, and D. K. Bohme. O-atom transport catalysis by atomic cations in the gas phase: reduction of N_2O by CO. *Journal of the American Chemical Society*, 127(10):3545–3555, 2005.

[256] F. Rondinelli, N. Russo, and M. Toscano. On the Pt^+ and Rh^+ catalytic activity in the nitrous oxide reduction by carbon monoxide. *Journal of Chemical Theory and Computation*, 4(11):1886–1890, 2008.

[257] I. Swart, F. M. F. De Groot, B. M. Weckhuysen, D. M. Rayner, G. Meijer, and A. Fielicke. The effect of charge on CO binding in rhodium carbonyls: from bridging to terminal CO. *Journal of the American Chemical Society*, 130(7):2126–2127, 2008.

[258] E. Barwa, M. Ončák, T. F. Pascher, A. Herburger, C. van der Linde, and M. K. Beyer. Infrared multiple photon dissociation spectroscopy of hydrated cobalt anions doped with carbon dioxide $CoCO_2(H_2O)_n$, n = 1–10, in the C O stretch region. *Chemistry – A European Journal*, 26(5):1074–1081, 2020.

[259] E. Barwa, T. F. Pascher, M. Ončák, C. van der Linde, and M. K. Beyer. Carbon dioxide activation at metal centers: Evolution of charge transfer from $Mg^{\cdot+}$ to CO_2 in $[MgCO_2(H_2O)_n]^{\cdot+}$, $n = 0$–8. *Angewandte Chemie International Edition*, 59(19):7467–7471, 2020.

[260] B. J. Knurr and J. M. Weber. Infrared spectra and structures of anionic complexes of cobalt with carbon dioxide ligands. *The Journal of Physical Chemistry A*, 118(23):4056–4062, 2014.

[261] O. Rodriguez and J. M. Lisy. Infrared spectroscopy of $Li^+(CH_4)_1Ar_n$, $n =$ 1-6, clusters. *The Journal of Physical Chemistry A*, 115(7):1228–1233, 2011.

[262] O. Rodriguez and J. M. Lisy. Revisiting $Li^+(H_2O)_{3-4}Ar_1$ clusters: Evidence of high-energy conformers from infrared spectra. *The Journal of Physical Chemistry Letters*, 2(12):1444–1448, 2011.

[263] A. D. Becke. Density-functional exchange-energy approximation with correct asymptotic behavior. *Physical Review A*, 38(6):3098, 1988.

[264] A. D. Becke. Density-functional thermochemistry. III. the role of exact exchange. *The Journal of Chemical Physics*, 98(7):5648–5652, 1993.

[265] C. A. Tolman. The 16 and 18 electron rule in organometallic chemistry and homogeneous catalysis. *Chem. Soc. Rev.*, 1:337–353, 1972.

[266] X. Jin, G. Wang, and M. F. Zhou. Matrix isolation infrared spectroscopic and theoretical study of nickel, palladium, and platinum nitrous oxide complexes. *The Journal of Physical Chemistry A*, 110(26):8017–8022, 2006.

[267] G. Wang, X. Jin, M. Chen, and M. F. Zhou. Matrix isolation infrared spectroscopic and theoretical study of the copper (i) and silver (i)–nitrous oxide complexes. *Chemical Physics Letters*, 420(1):130–134, 2006.

[268] T. Beyer and D. F. Swinehart. Algorithm 448: number of multiply-restricted partitions. *Communications of the ACM*, 16(6):379, 1973.

[269] J. R. Barker, T. L. Nguyen, J. F. Stanton, C. Aieta, M. Ceotto, F. Gabas, T. J. D. Kumar, L. L. Lohr C. G. L. Li, A. Maranzana, N. F. Ortiz, J. M. Preses, J. M. Simmie, J. A. Sonk, and P. J. Stimac. MultiWell-2020 software suite, 2020. University of Michigan, Ann Arbor, Michigan, USA.

[270] J. R. Heath, Y. Liu, S. C. O'brien, Q. L. Zhang, R. F. Curl, F. K. Tittel, and R. E. Smalley. Semiconductor cluster beams: one and two color ionization studies of Si_x and Ge_x. *The Journal of Chemical Physics*, 83(11):5520–5526, 1985.

[271] M. H. Stockett and S. Brøndsted Nielsen. Communication: Does a single CH_3CN molecule attached to $Ru(bipy)^+_{32}$ affect its absorption spectrum? *The Journal of Chemical Physics*, 142(17):171102, 2015.

[272] L. E. Orgel. 843. stereochemistry of metals of the b sub-groups. part i. ions with filled *d*-electron shells. *Journal of the Chemical Society (Resumed)*, pages 4186–4190, 1958.

[273] V. Zamudio-Bayer, R. Lindblad, C. Bülow, G. Leistner, A. Terasaki, B. v. Issendorff, and J. T. Lau. Electronic ground state of Ni_2^+. *The Journal of Chemical Physics*, 145(19):194302, 2016.

[274] D. M. Popolan and T. M. Bernhardt. Communication: CO oxidation by silver and gold cluster cations: identification of different active oxygen species. *The Journal of Chemical Physics*, 134(9):091102, 2011.

[275] V. V. Lavrov, V. Blagojevic, G. K. Koyanagi, G. Orlova, and D. K. Bohme. Gas-phase oxidation and nitration of first-, second-, and third-row atomic cations in reactions with nitrous oxide: Periodicities in reactivity. *The Journal of Physical Chemistry A*, 108(26):5610–5624, 2004.

[276] F. X. Li, K. Gorham, and P. B. Armentrout. Oxidation of atomic gold ions: Thermochemistry for the activation of O_2 and N_2O by Au^+ ($^1S_0$ and ^3D). *The Journal of Physical Chemistry A*, 114(42):11043–11052, 2010.

[277] J. Velasquez, B. Njegic, M. S. Gordon, and M. A. Duncan. IR photodissociation spectroscopy and theory of $Au^+(CO)_n$ complexes: nonclassical carbonyls in the gas phase. *J. Phys. Chem. A*, 112(9):1907–1913, 2008.

[278] M. E. Jacox and W. E. Thompson. Vibrational spectra of molecular ions isolated in solid neon. 6. carbon oxide ion (CO_4^-). *The Journal of Physical Chemistry*, 95(7):2781–2787, 1991.

[279] M. F. Zhou and L. Andrews. Infrared spectra of the CO_2^- and $C_2O_4^-$ anions isolated in solid argon. *The Journal of Chemical Physics*, 110(5):2414–2422, 1999.

[280] Q. Zhang, W. L. Li, C. Q. Xu, M. Chen, M. F. Zhou, J. Li, D. M. Andrada, and G. Frenking. Formation and characterization of the boron dicarbonyl complex $[B(CO)_2]^-$. *Angewandte Chemie International Edition*, 54(38):11078–11083, 2015.

[281] G. Deng, S. Pan, G. Wang, L. Zhao, M. F. Zhou, and G. Frenking. Beryllium atom mediated dinitrogen activation via coupling with carbon monoxide. *Angewandte Chemie*, 132(41):18358–18364, 2020.

[282] M. Chen, R. Yang, R. Ma, and M. F. Zhou. Infrared spectra of the sulfenic ester CH_3SOCH_3 and its photodissociation products in solid argon. *The Journal of Physical Chemistry A*, 112(31):7157–7161, 2008.

[283] M. F. Zhou, R. Ma, D. Yuan, and M. Chen. Reaction of chloromethyl radical with dioxygen: Formation of the chloromethylperoxy radical and its photodissociation in solid argon. *The Journal of Physical Chemistry A*, 113(12):2826–2830, 2009.

[284] J. Jašík and J. Roithová. Infrared spectroscopy of $CHCl_2^+$ molecular dications. *International Journal of Mass Spectrometry*, 377:109–115, 2015.

[285] X. Wu, L. Zhao, J. Jin, S. Pan, W. Li, X. Jin, G. Wang, M. F. Zhou, and G. Frenking. Observation of alkaline earth complexes $M(CO)_8$ (M = Ca, Sr, or Ba) that mimic transition metals. *Science*, 361(6405):912–916, 2018.

[286] A. S. Gentleman, A. E. Green, D. R. Price, E. M. Cunningham, A. Iskra, and S. R. Mackenzie. Infrared spectroscopy of $Au^+(CH_4)_n$ complexes and vibrationally-enhanced C–H activation reactions. *Topics in Catalysis*, 61(1):81–91, 2018.

[287] Y. Li, G. Wang, C. Wang, and M. F. Zhou. Coordination and solvation of the Au^+ cation: Infrared photodissociation spectroscopy of mass-selected $Au(H_2O)_n^+$ (n = 1–8) complexes. *The Journal of Physical Chemistry A*, 116(44):10793–10801, 2012.